# Multiscale Modelling of sI Methane Hydrate : Stability Limits and Mechanical Properties under Pressure

Doctor of Philosophy

Department of Chemical Engineering

McGill University

Montréal, Québec

April, 2023

A thesis submitted to McGill University in partial fulfillment of the requirements of the degree of Doctor of Philosophy

# Abstract

This thesis presents a multi-scale characterization of the mechanical properties, equation of state, pressure stability limits, fracture mechanisms and structural organization of methane gas hydrates using integrated atomistic simulations, geometric modelling, and continuum elasticity. All atomistic simulation work has been done using ab initio simulations under 0 Kelvin. This thesis focuses on sI methane hydrates which is a hydrogen-bonded polyhedral guest-host material and includes methane as the guest molecule. The results presented in this thesis provide valuable insights into piezo effects on the gas hydrate's stability. The pressure stability limits were determined to be 7.5 GPa and -1.1 GPa for the compressive and tensile loads, respectively. Once approaching the stability limits, two failure modes may be triggered. Within the stability limits, the values of the second-order elastic constants (SOEC) under pressure were determined, as well as the mechanical properties. Furthermore, a novel methodology to calculate third-order elastic constants (TOEC) was applied and validated, which can provide a non-linear tendency predictions on the piezo effects. Besides the unique and useful property data generated, this work elucidates how the gas hydrate system collapses in terms of the changes in electronic density, bond length, bond angles, cage shape and lattice volume size. Also, the important geometry-imposed cage connectivity of hydrates has been revealed. The occupancy effects on the stability limits were investigated, as well as the failure mechanisms that different occupancies would trigger. The work presented in this thesis fills a gap in the knowledge of science on the piezo effects on the mechanical properties of gas hydrates and their pressure stability limits through various perspectives. These results are crucial in developing gas hydrates technologies that involve the medium- and long-term storage of gases in the hydrate phase.

# Résumé

Cette thèse présente une caractérisation multi-échelle des propriétés mécaniques, de l'équation d'état, des limites de stabilité sous pression, des mécanismes de fracture et de l'organisation structurelle des hydrates de gaz de méthane en utilisant des simulations atomistiques intégrées, une modélisation géométrique et l'élasticité de continuum. Tous les travaux de simulation atomistique ont été réalisés à l'aide de simulations ab initio à 0 Kelvin. Cette thèse se concentre sur les hydrates de méthane sI qui sont des matériaux hôte-invité polyédriques liés par des liaisons hydrogène et comprennent le méthane comme molécule invitée. Les résultats présentés dans cette thèse fournissent des informations précieuses sur les effets piézoélectriques sur la stabilité de l'hydrate de gaz. Les limites de stabilité sous pression ont été déterminées à 7,5 GPa et -1,1 GPa pour les charges de compression et de traction, respectivement. Lorsque les limites de stabilité sont approchées, deux modes de défaillance peuvent être déclenchés. Dans les limites de stabilité, les valeurs des constantes élastiques de second ordre (SOEC) sous pression ont été déterminées, ainsi que les propriétés mécaniques. De plus, une méthodologie novatrice pour calculer les constantes élastiques de troisième ordre (TOEC) a été appliquée et validée, ce qui peut fournir des prévisions de tendance non linéaire sur les effets piézoélectriques. Outre les données de propriété uniques et utiles générées, ce travail élucide comment le système d'hydrate de gaz s'effondre en termes de changements de densité électronique, de longueur de liaison, d'angles de liaison, de forme de cage et de taille de volume de maille. De plus, la connectivité de cage imposée par la géométrie des hydrates a été révélée. Les effets d'occupation sur les limites de stabilité ont été étudiés, ainsi que les mécanismes de défaillance que différentes occupations pourraient déclencher. Le travail présenté dans cette thèse comble une lacune dans la connaissance scientifique sur les effets piézoélectriques sur les propriétés mécaniques des hydrates de gaz et

leurs limites de stabilité sous pression sous différents points de vue. Ces résultats sont cruciaux pour développer des technologies d'hydrates de gaz qui impliquent le stockage à moyen et long terme de gaz dans la phase d'hydrate.

# Acknowledgements

This thesis was only possible because of the abundant love, support, inspiration, and discipline lavished on me by a huge number of people whom I would like to acknowledge and offer my sincerest thanks.

First, I would like to thank my two supervisors, Dr. Alejandro Rey and Dr. Phillip Servio, for guiding me through my academic journey, being available and present at all times, and always being a constant source of inspiration. I am grateful to have supervisors who dedicate so much time and effort to my personal and professional growth. I appreciate them not only for encouraging me to pursue my dream, but also for being my strongest support as I made a career transition.

I would also like to thank all my colleagues who have made my graduate life so colourful and memorable. In the very beginning, when I was struggling with software and simulations, Sam spent a lot of time helping me overcome all these obstacles. When I needed assistance with my writing, Shaden and Andre always provided me with sound advice. Whenever I had a math problem, Ziheng would help me out. When I was stressed, Sahar and Victoria talk to me and help me relax. Every day, David would remind me that the coffee was ready. Eric and Ali would always bring something intriguing to discuss during lunch.

Lastly and most importantly, I would like to my parents the deepest acknowledgement. I couldn't appreciate the world's beauty without them. My parents encouraged me to make every decision in life at every fork in the road. They believed in and supported every choice I made. They gave me the most confidence in my ability to create my own life. Without their encouragement, I would not have been brave enough to pursue a direct-PhD path. It is my pleasure to be your daughter. Thank you.

# Table of Contents

# List of Figures

# List of Tables

# Contributions of the Author

The following document is a manuscript-based thesis which consists of four published manuscripts. All work presented herein (e.g. simulations, data collection and analysis and article write-ups) has been performed by the author of this thesis (Xiaodan Zhu), with the review assistance of André Guerra and Shaden Daghash and under the supervision of Dr. Alejandro Rey and Dr. Phillip Servio, who provided guidance.

- Zhu, X., Rey, A. D. & Servio, P. Multiscale Piezoelasticity of Methane Gas Hydrates: From Bonds to Cages to Lattices. Energy Fuels **36**, 10591–10600 (2022).
- Zhu, X., Rey, A. D. & Servio, P. Piezo-elasticity and stability limits of monocrystal methane gas hydrates: Atomistic-continuum characterization. The Canadian Journal of Chemical Engineering **101**, 639-650 (2023).
- Zhu, X., Guerra, A., Servio, P. & Rey, A. D. Atomistic-geometric simulations to investigate the mechanical stability of monocrystalline sI methane hydrates under pressure. *Scientific Reports* **13**, 1907, doi:10.1038/s41598-023-29194-8 (2023).
- Zhu, X., Guerra, A., Servio, P. & Rey, A. D. DFT-continuum characterization of third-order elasticity of sI methane hydrates under pressure. Materials Research Express, doi:10.1088/2053-1591/acbf0a (2023).

# Contribution to original knowledge

The following is a list of original knowledge contributions resulting from the work presented in this thesis:

- Fulfilled the knowledge gap of the gas hydrates' behaviours under pressure
    - Determined the exact pressure stability limits of sI methane hydrate at 0 K.
    - Introduced piezo sensitivity factors to determine hydrates' pressure stability.
    - Elucidated the brittle-to-ductile transition of sI methane hydrates over pressures.
- Performed multi-scale analysis on the hydrate lattice under pressure
    - Presented the electron cloud movements of hydrate lattice under pressure.
    - Demonstrated the bond angle and bond length distributions of hydrates under pressure.
    - Characterized the cage deformation mechanisms.
    - Performed law of mixtures prediction on the gas hydrates' mechanical properties.
- Conducted Third-Order Elastic Constant (TOEC) calculations on sI methane hydrates
    - Proposed non-linear models that have advantages when the system is subject to significant strains.
    - Verified the ability of TOECs to assess the piezo effects on the Second-Order Elastic Constant (SOEC).
    - Improved the estimation of sensitivity factor values and ductile-to-brittle transition threshold.
- Discovered the geometry-imposed cage features in terms of piezo effects and occupancy

- Investigated the inclusion-matrix material composite structures of sI gas hydrates.
- Established an equation to predict the sI methane hydrate’s mechanical stability limits in terms of occupancy at zero Kelvin.
- Investigated two failure mechanisms under pressure based on the hydrate's occupancy.

# Chapter 1

# 1 Introduction

## 1.1 Thesis Motivation

Gas hydrates (GH), also known as clathrate hydrates, have garnered the interest of the scientific community as well as the general public due to their numerous engineering applications. Water molecules construct the main skeleton of the hydrate lattice. To maintain the solid state (similar to ice), the gas hydrates usually get formed in the deep ocean and permafrost areas that have high pressures and low temperatures[1,2]. It is reported that 80% of natural hydrates contain methane gas, which is recognized as an energy-intensive material[3]. So far, around 6.4 trillion tons of methane have been detected trapped in the deposits of methane hydrate on the deep ocean floor[4]. It is estimated that the amount of energy contained in these natural hydrates is more than twice the amount found in all other available hydrocarbons combined, which indicates that natural hydrates will be among the most competitive clean energy sources. Besides the high energy content, gas hydrates have a unique guest-host structure, where the water molecules form the host cages, and the gas molecules are encapsulated by the host cages as guests. This unique structure can be used for many applications; for example, carbon dioxide and hydrogen gas storage.

It is well-recognized that gas hydrates have multiple applications, such as natural gas production, carbon capture and gas separation; however, gas hydrate exploration is still limited to the research stage. Although some countries, like Japan and China, attempted at large-scale extraction of methane hydrate, they announced the commercial-scale production remains years away[5,6]. During exploration/ extraction, the accidental release of methane into the atmosphere or the deep sea would endanger the lives of animals. The oil and gas industry spends millions of dollars to remove or prevent the formation of gas hydrates because such formation can cause pipeline blockages or even explosions. In addition, global warming and frequent crustal movements, as well as changes in temperature and pressure, have created an environment unsuitable for natural gas hydrates.

Considering the various applications of gas hydrates and the security issues in the oil and gas industry, the most important task for future research is to examine the stability of gas hydrates. However, as discussed later in Chapter 2.2, the reliable literature data remains limited, and the factors that affect the gas hydrate's stability in terms of atoms, bonds, cages, and lattices are poorly understood.

This thesis contributes to knowledge by filling the gap in understanding the behavior of gas hydrates under pressure. It explores pressure stability limits and transition mechanisms, proposes non-linear models involving higher-order elastic constants for mechanical properties calculations, and examines geometry-imposed cage features to predict mechanical stability limits. Additionally, the analysis characterizes cage deformation mechanisms and investigates failure mechanisms under pressure based on hydrate occupancy. The findings provide novel insights into the behavior of gas hydrates and improve the understanding of their mechanical properties. Specifically, the software of Vienna Ab initio Simulation Package (VASP)[7-10] was selected to run all density functional theory (DFT) simulations. VESTA[11], a three-dimensional visualization system for electronic and structural analysis, was used to visualize the structure of the deformed hydrate lattice under pressure. Also, MATLAB was used for all the post-simulation calculations and analysis. After discussing the motivation behind this thesis, the rest of the chapter will demonstrate the objectives and the structure of this work.

## 1.2 Thesis Objectives

The following are the specific objectives of this thesis related to piezo effects, pressure stability limits, and gas hydrate fracture mechanisms:

**Chapter 3: determine the pressure stability limits and the mechanical properties of sI methane hydrate by using Ab initio first principle**

1. To determine the bulk modulus and its first derivatives by applying the isothermal Equation of State fittings to the Energy-Volume curve (Chapter 3).
2. To generate the sensitivity factor of mechanical properties of sI methane hydrates along with pressure (Chapter 3).
3. To establish a table for mechanical properties of sI methane hydrates under pressure before reaching stability limits (Chapter 3).
4. To apply the Born stability criteria to determine the mechanical stability limits (Chapter 3).

**Chapter 4: perform multi-scale geometric structural analysis on sI methane hydrate under pressure: from atoms to cages to lattice**

5. To demonstrate the electron density distribution under pressure (Chapter 4).

6. To illustrate the bond parameter distribution under pressure in terms of bond angles and bond lengths (Chapter 4).
7. To investigate the role of each type of cage in terms of the rules of mixture (Chapter 4).

**Chapter 5: Conducting third-order elastic constants (TOECs) calculations to evaluate the piezo-effects on second-order elastic constants (SOECs)**

8. To determine all second-order and third-order elastic constants of sI methane hydrates at zero pressure and zero Kelvin (Chapter 5).
9. To calculate the values of second-order elastic constants under pressure using the third-order elastic constants values (Chapter 5).
10. To evaluate the mechanical properties of sI methane hydrate by using linear and non-linear fittings (Chapter 5).
11. To determine the ductile-to-brittle transition using Pugh ratio and Pettifor criteria (Chapter 5).

**Chapter 6: Determine the two-phased structure of sI gas hydrates and investigate the impacts of occupied cages on the pressure stability**

12. To conduct two-phase structural analysis on sI gas hydrates (Chapter 6).
13. To investigate the effects of cages on the structural integrity of gas hydrates in terms of volumetric size under pressure (Chapter 6).
14. To develop an equation to estimate the mechanical stability limits of sI methane hydrates in terms of occupancy and occupied cage types (Chapter 6).

15. To examine the steepest ascending and descending curves to strengthen or weaken the sI methane gas hydrates based on their occupancy and cage type (Chapter 6).
16. To assess the fracture mechanisms that take place when hydrate systems with varying occupancies reach their stability limits (Chapter 6).

## 1.3 Thesis Organization

This thesis begins with a general introduction to clathrate hydrates associated with the scope of this work (Chapter 2). It includes the structural features and mechanical properties of gas hydrates. Also, a comprehensive literature review is provided to present the current status and understanding of gas hydrate and it is followed by a background discussion on the computational methods and software employed in this work. The organization of the rest of the thesis (Chapters 3-8) is shown in Figure 1-1.

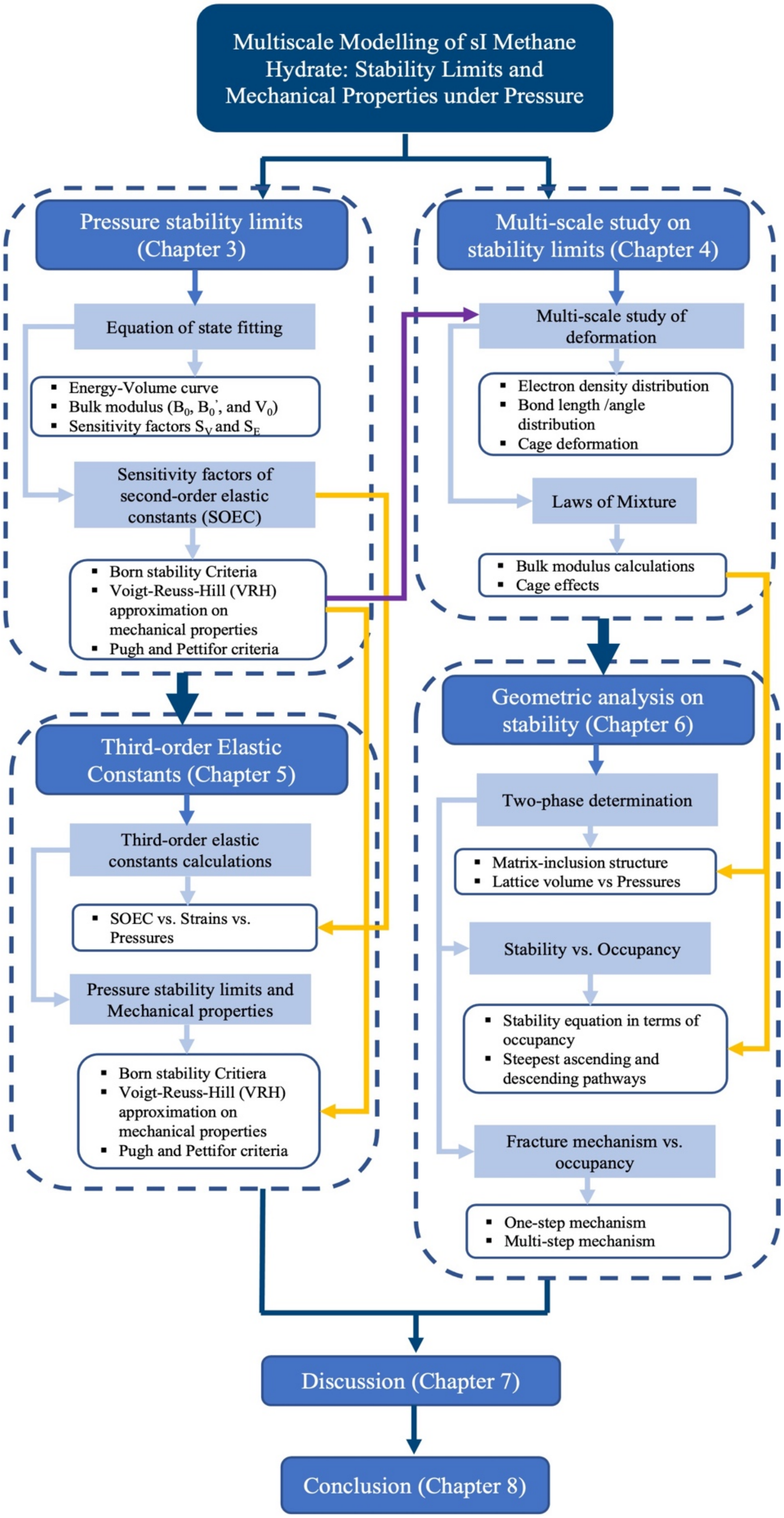

*Figure 1-1Thesis organization chart connecting the different thesis chapters*

In Chapter 3, the simulations are performed on the monocrystalline defect free sI methane hydrate with 100% cage occupancy. The ground-state volume and energy in terms of pressures are presented with the equations of state (EOS) fitting and the pressure sensitivity factor of the bulk modulus. Meanwhile, the relationship between second-order elastic constants (SOEC) and hydrostatic pressures is characterized. The Born stability criteria and Voigt-Reuss-Hill (VRH) approximation, based on the SOEC values, are applied to obtain the theoretical pressure limits and their associated polycrystalline mechanical properties.

In Chapter 4, we analyze the pressure effects on the sI methane hydrates from the structural aspect of the electron cloud, atoms interactions and cage deformation. To be specific, the electron density distributions under different pressures are characterized. The atoms' interactions, bond lengths and angles, are determined as a distribution with respect to pressures. The details of cage deformation are characterized. Also, the law of mixtures was applied to the gas hydrates for their elastic property predictions.

Chapter 5 focuses on the calculations of third-order elastic constants (TOEC) of monocrystalline sI methane hydrates and their applications. It demonstrates the use of TOEC to make a prediction on the piezo effects on the second-order elastic constants (SOEC). Also, the SOECs values obtained from TOECs prediction and the SOECs under pressure obtained from the simulation are compared, which shows a high consistency. In addition, the SOECs under pressure derived from TOEC predictions are done consistently well in calculations of mechanical properties, determination of stability limits, and ductile-to-brittle transition.

In Chapter 6,  a geometric analysis of the sI methane hydrate and the behavior of the cage under pressures especially with occupied guest molecules, were performed. Firstly, the two-phase matrix-inclusion structure is determined due to the polygonal connectivity through face sharing.

The stability thresholds in terms of phase modes were then determined, identifying two failure patterns. The correlation between the phase occupancy and compressive stability limits is established as well. An equation for the mechanical stability surface under variable methane occupancy is proposed by using a ternary non-ideal law of mixtures. Also, computing the steepest descent and ascent curves leads to the identification of optimal strengthening by specific gas occupancy and maximal failure routes mainly by a decrease of matrix phase occupancy.

# 1.4 Reference

1 Buffett, B. & Archer, D. Global inventory of methane clathrate: sensitivity to changes in the deep ocean. *Earth and Planetary Science Letters* **227**, 185-199, doi:https://doi.org/10.1016/j.epsl.2004.09.005 (2004).

2 Chong, Z. R., Yang, S. H. B., Babu, P., Linga, P. & Li, X.-S. Review of natural gas hydrates as an energy resource: Prospects and challenges. *Applied Energy* **162**, 1633-1652, doi:https://doi.org/10.1016/j.apenergy.2014.12.061 (2016).

3 Council of Canadian Academies. Expert Panel on Gas, H. (Council of Canadian Academies = Conseil des académies canadiennes, Ottawa, 2008).

4 Buffett, B. & Archer, D. Global inventory of methane clathrate: sensitivity to changes in the deep ocean. *Earth and Planetary Science Letters* **227**, 185-199, doi:10.1016/j.epsl.2004.09.005 (2004).

5 News, B. *China claims breakthrough in mining 'flammable ice'*, <https://www.bbc.com/news/world-asia-china-39971667> (2017).

6 Post, N. *China and Japan find way to extract 'combustible ice' from seafloor, harnessing a legendary frozen fossil fuel*, <https://nationalpost.com/news/world/china-japan-extracts-combustible-ice-from-seafloor-a-step-towards-harnessing-a-legendary-frozen-fossil-fuel> (2017).

7 Kresse, G. & Furthmüller, J. Efficiency of ab-initio total energy calculations for metals and semiconductors using a plane-wave basis set. *Computational Materials Science* **6**, 15-50, doi:https://doi.org/10.1016/0927-0256(96)00008-0 (1996).

8 Kresse, G. & Hafner, J. Ab initio molecular dynamics for liquid metals. *Physical Review B* **47**, 558-561, doi:10.1103/PhysRevB.47.558 (1993).

9 Kresse, G. & Furthmüller, J. Efficient iterative schemes for ab initio total-energy calculations using a plane-wave basis set. *Physical Review B* **54**, 11169-11186, doi:10.1103/PhysRevB.54.11169 (1996).

10 Kresse, G. & Joubert, D. From ultrasoft pseudopotentials to the projector augmented-wave method. *Physical Review B* **59**, 1758-1775, doi:10.1103/PhysRevB.59.1758 (1999).

11 Momma, K. & Izumi, F. VESTA 3 for three-dimensional visualization of crystal, volumetric and morphology data. *Journal of Applied Crystallography* **44**, 1272-1276, doi:https://doi.org/10.1107/S0021889811038970 (2011).

# Chapter 2

# 2 Background

## 2.1 Clathrate hydrates

Clathrate hydrates, also known as gas hydrates or simply hydrates, are crystalline solids that resemble ice and consist of water molecules encapsulating various gas molecules[1]. The lattice structure of clathrate hydrates is formed by the hydrogen bonds of water, and the entire structure is stabilized by the presence of trapped gas molecules[2]. In other words, clathrate hydrates are clathrate compounds in which the host molecule is the water, and the guest molecule is typically a gas or liquid. The most common guest molecules are methane and carbon dioxide. Most gas hydrates are formed at high pressures and low temperatures except for some low molecular weight gases. As the encapsulated guest molecules are never bonded to the lattice, the formation and decomposition of clathrate hydrates are first-order phase transitions, not chemical reactions[3-5]. In 2020, 250,000-700,000 cubic feet of methane have been detected that being trapped in the deposits of methane hydrate on the deep ocean floor[6]. It is estimated that the amount of energy contained in these natural hydrates is more than twice the amount found in all other available hydrocarbons combined, which indicates that natural hydrates will be the most competitive clean energy source.

The three most common types of gas hydrates are structure I (sI), structure II (sII), and structure H (sH) gas hydrates. The main differences among the three types of hydrates are the types of cages that contribute to their lattice structures and the number of each cage type involved. The details of sI gas hydrate structure are shown in Figure 2-1 and details of each type of gas hydrate structures will be discussed below.

Each structure has at least two kinds of cages involved. The general notation, $X^n$, describes the water cages where X is the number of sides of a cage face, and n is the number of cage faces having these X sides[7]. The pentagonal dodecahedral water cage (12-hedra), denoted $5^{12}$, which comprises of 12 pentagons, is present in all three structures, shown as Figure 2-1 (A). Apart from this, sI structure is composed of tetradecahedral cavities (14-hedra), denoted $5^{12}6^2$ (comprising of 12 pentagons and 2 hexagons), shown as Figure 2-1 (B). For sII structure, instead of the tetradecahedral cavities, larger hexacaidecahedral cavities (16-hedra), denoted $5^{12}6^4$ (comprising of 12 pentagons and 4 hexagons) are present[7]. Compared with sI and sII structures, sH has a hexagonal framework. Besides the $5^{12}$ cavities, it has another two types of large cavities ($4^35^66^3$ and $5^{12}6^8$), which can contain a large molecular fluorinated gas (octafluorocyclobutane, c-C4F8)[8].

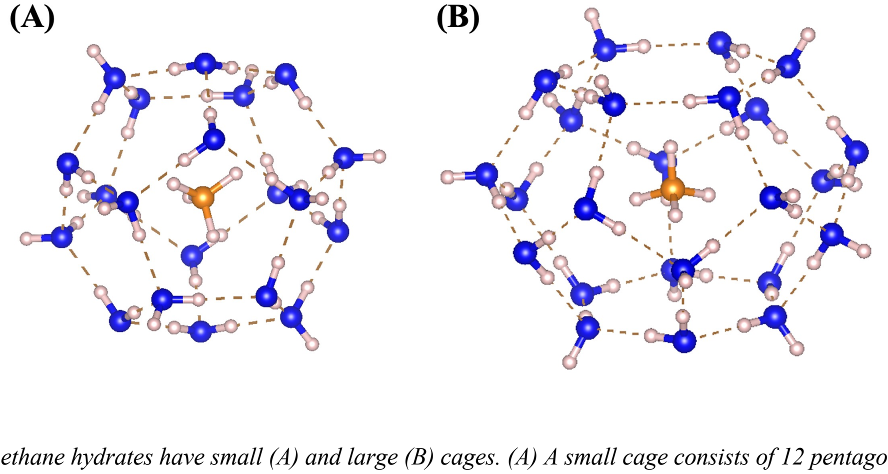

*Figure 2-1 sI methane hydrates have small (A) and large (B) cages. (A) A small cage consists of 12 pentagonal faces and a methane molecule at its center. Large cages (B) have 12 pentagonal faces and two hexagonal faces, with a guest methane molecule at the center. Water oxygen atoms are represented by blue circles. Hydrogen atoms are represented by pink-white* *circles. Carbon atoms are denoted by orange circles. All solid lines represent covalent bonds; their colors indicate which two atoms formed the covalent bond. OH hydrogen bonds are displayed by the brown dashed lines*[9]

The detailed geometric properties of these three hydrate structures, along with their respective cavities, are presented in Table 2-1. For full occupancy, the ideal molar guest-to-water ratio for an sI is 1: 5.75[2]. Usually, the stabilization of the entire hydrate system is supported by the van der Waals Forces between the gas molecules (guest) and the water molecules (host). So the hydrate's occupancy is around 80% in nature. However, under extreme conditions (temperatures between 100 and 220 K and pressures between 1 and 5000 bar), the hydrate's structure can even be nucleated without guest molecules[10-13]. Typically, each cavity accommodates only one guest molecule ranging in diameter from 0.40 to 0.90 nm[2]. sI hydrates are the most commonly encountered naturally occurring hydrate structure which encases small diameter molecules (0.40-0.55 nm) such as methane gas. sII and sH hydrates can accommodate larger guest molecules, typically propane for sII or combinations of methane gas and nexohexane or cycloheptane for sH, but they are less prevalent in nature[2].

*Table 2-1 Geometrical parameters of the main hydrate crystal structures*[2]

| | Structure I | | Structure II | | Structure H | | |
|---|---|---|---|---|---|---|---|
| cavity | small | large | Small | Large | Small | Medium | Large |
| Description | $5^{12}$ | $5^{12}6^{2}$ | $5^{12}$ | $5^{12}6^{4}$ | $5^{12}$ | $4^{3}5^{6}6^{3}$ | $5^{12}6^{8}$ |
| Cavities/ unit cell | 2 | 6 | 16 | 8 | 3 | 2 | 1 |
| Average cavity radius, nm | 0.395 | 0.433 | 0.391 | 0.473 | 0.391 | 0.406 | 0.571 |
| Coordination number | 20 | 24 | 20 | 28 | 20 | 20 | 36 |

| | | | |
|---|---|---|---|
| Water molecules per unit cell | 46 | 136 | 34 |
| Lattice type | Cubic | Face-centered cubic | Hexagonal |
| Unit cell parameters, nm | a=1.2 | a=1.7 | a=1.21, c=1.01 |
| Density, $kg/m^3$ | 912 | 940 | 1952 |

# 2.2 Gas Hydrates' Properties

## 2.2.1 Current Status

So far, many research groups are looking into the thermodynamic and mechanical properties of gas hydrates because of their high energy content and potential applications. However, the difficulties associated with recreating the actual environment of gas hydrates in the laboratory restrict the study and the investigation of their properties. This phenomenon further demonstrates the significance of gas hydrate modelling and simulations. In this section, we will examine the current understanding of gas hydrate, which provides a solid foundation for this thesis.

Since gas hydrates contain at least 85 mol% water molecules, this indicates that an analogy could be applied between gas hydrates and ice. The high water content in hydrates suggests that the mechanical properties of all three hydrate structures should be similar to those of ice. A comparison of properties among a unit cell size of sI, sII gas hydrates and Ih ice is shown in Table 2-2.

*Table 2-2 Comparison of properties of ice(Ih), sI, and sII hydrate crystal structures*[14]

| Property | Hexagonal Ice (Ih) | Structure I gas hydrate | Structure II gas hydrate |
|---|---|---|---|
| Water molecules number | 4 | 46 | 136 |
| Lattice parameters at 273K, nm | a=0.452<br>c=0.736 | 1.20 | 1.73 |
| Dielectric constant at 273K | 94 | ~58 | 58 |
| Water diffusion correlation time, $\mu s$ | 220 | 240 | 25 |
| Water diffusion activation energy, kJ/m | 58.1 | 50 | 50 |
| Isothermal Young's Modulus at 268K, $10^9$ Pa | 9.5 | 8.4 (est.) | 8.2 (est.) |
| Poisson's ratio | 0.33 | ~0.33 | ~0.33 |
| Bulk modulus (GPa) | 8.8 (272K) | 5.6 (272K) | 11.14 (0 K) |
| Shear modulus (GPa) | 3.9 (272K) | 2.4 (272K) | 4.36 (0 K) |
| Compressional velocity (Vp), m/s | 3870.1 | 3778.0 | 3821.8 |

| | | | |
|---|---|---|---|
| Shear velocity (Vs), m/s | 1949 | 1963.6 | 2001.1 |
| Velocity ratio (comp./shear) | 1.99 | 1.92 | 1.91 |
| Linear thermal expansion, at 200K, $K^{-1}$ | $56 \times 10^{-6}$ | $77 \times 10^{-6}$ | $52 \times 10^{-6}$ |
| Adiabatic bulk compression (273K), $10^{-11}$ Pa | 12 | 14 (est.) | 14 (est.) |
| Heat Capacity, $J \cdot kg^{-1} \cdot K^{-1}$ | 3800 | 3300 | 3600 |
| Thermal conductivity (263K), $W \cdot m^{-1} \cdot K^{-1}$ | 2.23 | $0.49 \pm 0.02$ | $0.51 \pm 0.02$ |
| Refractive index, 638 nm, -3℃ | 1.3082 | 1.3460 | 1.350 |
| Density, $kg \cdot m^{-3}$ | 916 | 912 | 940 |

Table 2-2 demonstrates the physical properties of ice and sI and sII gas hydrates. It shows that the physical properties of bulk gas hydrates are remarkably close to those of pure ice, with only a big difference shown in the thermal conductivity. The thermal conductivity of ice is 2.23 $W{\cdot}m^{-1}{\cdot}K^{-1}$ but for sI and sII hydrates, the values are around 0.50 $W{\cdot}m^{-1}{\cdot}K^{-1}$, which is four times smaller than that of ice. A lower thermal conductivity indicates that a temperature change on the gas hydrate’s surface would not lead to a temperature change in the internal system. As the heat cannot be dissipated within a short period of time, a temperature difference may be introduced as a function of axis symmetry. This uneven distribution of temperature would lead to crack nucleation on bounding surfaces.

It is important to note that the data present in Table 2-2 are limited to a very small range of temperatures, pressures and the type of guest molecules. However, these factors would significantly affect gas hydrates’ properties. Thus, to build a comprehensive picture of the mechanical properties of gas hydrates, understanding their behavior under pressure in terms of the factors mentioned above becomes very essential.

### 2.2.2 Knowledge Gap

As discussed above, the similarities between gas hydrates and the ice Ih have been partially explored. However, the current understanding of gas hydrates cannot support any long-term commercial scale exploration. Therefore, a comprehensive investigation is required, focusing on the impact of the environment on the hydrate's properties. Given the limitations of laboratory experiments in recreating environmental conditions, modelling simulations were chosen to conduct all required research investigations in this thesis to detail the effects of each factor.

In gas hydrates research, it is known that temperature and pressure have a significant impact on the gas hydrate’s properties and stability[15]. The effects of global warming on temperature appear to be considerably smaller than the pressure changes caused by earthquakes or plate movements. Thus, in this thesis, the focus is on the pressure effects (piezo-effects) on the gas hydrates mechanical properties and their stability limits.

Pressure stability limits for gas hydrates and associated fracture mechanisms have not been reported to date. However, because the pressure can fluctuate, this is crucial for methane extraction and $CO_2$ sequestration. Methane leaks may occur if the process exceeds the pressure stability limit, posing a threat to marine life. The pressure stability limit is a crucial value that must be investigated. In addition, the mechanism of fracture triggered when the pressure stability limit is exceeded is dependent on the intrinsic brittleness or ductility of the material. Understanding the fracture mechanisms and lattice collapse processes will aid in stopping the process of decomposition.

Additionally, the second-order elastic constants (SOECs) are the fundamental values to calculate the mechanical properties or stability evolution. As expected, the values of SOECs will change as the pressure changes. Thus, characterizing the piezo effects on the SOECs, and quantifying this relationship are most important in this thesis.

To summarize, this thesis would fill a gap in the knowledge of science on the pressure effects on gas hydrates' properties and stability. These findings would be useful for further studies or exploration of gas hydrates.

## 2.3 Modeling and simulation

To discover the gas hydrates' properties and their stability, first principles simulations with density functional theory (DFT) were utilized in the work presented in this thesis. To be specific, the Vienna Ab initio Simulation Package (VASP)[16] was utilized to conduct all simulations from the atomistic level. In this section, the principles of DFT and the details of VASP will be discussed.

## 2.3.1 Density Functional Theory (DFT)

The quantum mechanical wavefunction contains, in principle, all the information about a given system. In order to estimate the mechanical and thermodynamic properties of the material, it is necessary to obtain the wavefunction of its atomic system[17]. Schrödinger's equation describes the wave function or state function of a quantum-mechanical system, and the main goal of any DFT computation is to calculate the total energy of a specific set of atoms, which is done by solving the time-independent Schrödinger equation[18].

The time-independent Schrödinger equation describes the stationary states of the wave function, shown as Equation 2.1

$$H\psi = E\psi \qquad 2.1$$

In Eqn 2.1, H is the Hamiltonian operator and $\psi$ is a set of solutions, or eigenstates, of the Hamiltonian. Each of these solutions, $\psi_n$, has an associated eigenvalue, $E_n$, a real number that satisfies the eigenvalue equation.

To determine the energy changes as atoms move around, it is necessary to define the position of an atom. As the atomic nuclei are much heavier than individual electrons, the electrons respond much rapidly to changes in their surroundings than nuclei can. For a given set of electrons moving in the field of a set of nuclei, the lowest energy configuration of the electrons are found. The lowest energy state is known as the ground state of the electrons, and the separation of the nuclei and electrons into separate mathematical problems is the *Born-Oppenheimer approximation*[18].

The detailed definition of the Hamiltonian depends on the physical system being described by the Schrödinger equation. To consider multiple electrons interacting with multiple nuclei, a more complete description of the Schrödinger is shown by Equation 2.2:

$$\left[-\frac{h^2}{2m}\sum_{i=1}^{N}\nabla_i^2+\sum_{i=1}^{N}V(r_i)+\sum_{i=1}^{N}\sum_{j<i}U\left(r_i,r_j\right)\right]\psi=E\psi \tag{2.2}$$

Here, m is the electron mass. The three terms in brackets define, in order, the kinetic energy of each electron, the interaction energy between each electron and the collection of atomic nuclei, and the interaction energy between different electrons[18].

To find the wave function, 3N dimensions are required, where N is the number of electrons involved in unit cell. It indicates thousands of dimensions have to be determined simultaneously, which seems impossible. To solve this problem, Kohn and Sham proposed to find the right electron density can be expressed in a way that involves solving a set of equations in which each equation only involves a single electron[18].

The Kohn-Sham equations have the form presented by Equation 2.3

$$\left[-\frac{h^2}{2m}\nabla^2+V(r)+V_H(r)+V_{XC}(r)\right]\psi_i(r)=\varepsilon_i\psi_i(r) \tag{2.3}$$

The main difference between the Eqn. 2.2 and Eqn. 2.3 is that the Kohn-Sham equations are missing the summations that appear inside the full Schrödinger equation. This is because the solution of the Kohn-Sham equations are single-electron wave functions that depends only on three spatial variables, $\psi_i(r)$. Since the wave function for any particular set of coordinates cannot be directly observed, the quantity that can be measured is the probability that the N electrons are at a particular set of coordinates. Thus, the density of electrons at a particular position in space can be written in terms of the individual electron wave functions as shown by Equation 2.4

$$n(r) = 2\sum_{i} \psi_i^* (r)\psi_i(r) \tag{2.4}$$

The transition from wave functions to electron density rests on two fundamental mathematical theorems. The first theorem, proved by Hohenberg and Kohn, is : *the ground-state energy from Schrodinger's equation is a unique functional of the electron density*[18]. The second Hohenberg-Kohn theorem defines an important property of the functional: *the electron density that minimizes the energy of the overall functional is the true electron density corresponding to the full solution of the Schrodinger equation*[18].

For Eqn. 2.4, the term inside the summation is the probability that an electron in individual wave function $\psi_i(r)$ is located at position r. The factor of 2 appears because electrons have spin and the Pauli exclusion principle state that each individual electron wave function can be occupied by two separate electrons provided they have different spins[18].

## 2.3.2 Vienna Ab initio Simulation Package (VASP)

The Vienna Ab initio Simulation Package (VASP)[19-22] has been widely used for atomic scale materials modelling from first principles. VASP uses periodic boundary conditions and pseudopotential method with a plane wave basis set[16]. VASP obtains the converged physical properties such as the lattice volume and energy, and the electronic ground state of material through as self-converged calculation, as shown in Figure 2-2.

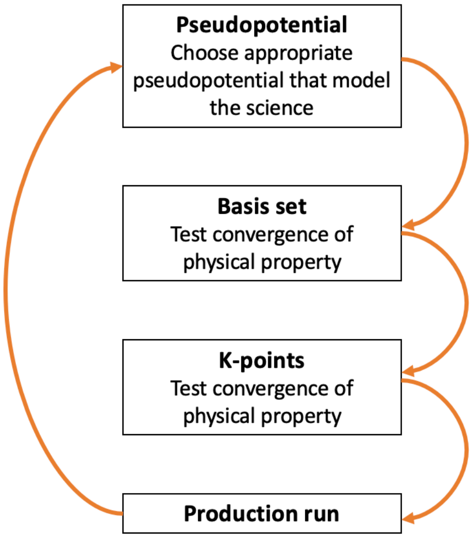

*Figure 2-2 Self-consistency cycle method within VASP[16]*

Four input files are required for VASP simulations, which are INCAR, PSOCAR, POTCAR, and KPOINTS files. INCAR file contains the user specified parameters that define the calculations, such as energy cut-off, ionic and geometric relaxation parameters. POSCAR specifies the periodic simulation cell and includes the geometry of the system. POTCAR is a pseudopotential file and has the atoms' information[23]. KPOINTS defines the k-point mesh, which affects the accuracy of the results[16]. Some of the key parameters of the four input files are shown in

Table 2-3.

*Table 2-3 Summary of key parameters of VASP input files*

| | |
|---|---|
| Exchange-correlation functional | revPBE+DFT-D2 dispersion correction |
| Cut-off energy | 520 eV |
| Global break conditions the electronic self-consistent loop | $1 \times 10^{-4}\ eV$ |
| Break conditions for the ionic relaxation | $5 \times 10^{-3}\ eV/\text{Å}$ |

| | |
|---|---|
| Calculation algorithm | Newton and conjugate gradient algorithms |
| Number of k-points | 4 |
| Grid generation mode | Gamma centred |

## 2.4 Post-simulation calculations

In this thesis, MATLAB was selected as the main software for the post-simulation calculations. The simulations results can provide structural information on the lattice under given conditions, such as lattice energy, lattice volume and atomic positions. This information are useful to understand lattice's response under specified condition. For example, the calculations of bond parameters, e.g., bond angles and bond lengths, the MATLAB code was written to identify the neighboring atoms for each oxygen atoms and calculate the associated bond length and angles. The distribution and fitting process were conducted by MATLAB as well. The details for methodologies applied in each project using MATLAB are demonstrated in each Chapter 3-6.

In addition, VESTA: a Three-Dimensional Visualization System for Electronic and Structural Analysis[24], is a software that was selected to visualize the relaxed structural lattice. The details of the model information and the selected planes for the visualization are shown in the Chapter 4 and 6.

## 2.5 Acknowledgement

Figure 2-1, reproduced with permission from Springer Nature, ‘Zhu, X., Guerra, A., Servio, P. & Rey, A. D. Atomistic-geometric simulations to investigate the mechanical stability of monocrystalline sI methane hydrates under pressure. *Scientific Reports* **13**, 1907, doi:10.1038/s41598-023-29194-8 (2023).

# 2.6 Reference

1 Englezos, P. Clathrate hydrates. *Industrial & engineering chemistry research* **32**, 1251-1274 (1993).

2 Sloan Jr, E. D., Koh, C. A. & Koh, C. A. Clathrate Hydrates of Natural Gases. doi:10.1201/9781420008494 (2007).

3 Gao, S., Chapman, W. G. & House, W. NMR and Viscosity Investigation of Clathrate Hydrate Formation and Dissociation. *Industrial & Engineering Chemistry Research* **44**, 7373-7379, doi:10.1021/ie050464b (2005).

4 Gao, S., House, W. & Chapman, W. G. NMR/MRI Study of Clathrate Hydrate Mechanisms. *The Journal of Physical Chemistry B* **109**, 19090-19093, doi:10.1021/jp052071w (2005).

5 Choudhary, N., Chakrabarty, S., Roy, S. & Kumar, R. A comparison of different water models for melting point calculation of methane hydrate using molecular dynamics simulations. *Chemical Physics* **516**, 6-14, doi:https://doi.org/10.1016/j.chemphys.2018.08.036 (2019).

6 Management, O. o. F. E. a. C. *Gas Hydrates*, <https://www.energy.gov/fecm/gas-hydrates> (2020).

7 Gabitto, J., Tsouris, C. & Oak Ridge National Lab, O. R. T. N. Physical Properties of Gas Hydrates: A Review. *Journal of Thermodynamics* **2010**, doi:10.1155/2010/271291 (2010).

8 Kim, E. & Seo, Y. A novel discovery of a gaseous sH clathrate hydrate former. *Chemical Engineering Journal* **359**, 775-778 (2019).

9 Zhu, X., Guerra, A., Servio, P. & Rey, A. D. Atomistic-geometric simulations to investigate the mechanical stability of monocrystalline sI methane hydrates under pressure. *Scientific Reports* **13**, doi:10.1038/s41598-023-29194-8 (2023).

10 Cruz, F. J. A. L., Alavi, S. & Mota, J. P. B. Low-Temperature Thermodynamic Study of the Metastable Empty Clathrate Hydrates Using Molecular Simulations. *ACS Earth and Space Chemistry* **3**, 789-799, doi:10.1021/acsearthspacechem.9b00009 (2019).

11 Falenty, A., Hansen, T. C. & Kuhs, W. F. Formation and properties of ice XVI obtained by emptying a type sII clathrate hydrate. *Nature* **516**, 231-233, doi:10.1038/nature14014 (2014).

12 Kosyakov, V. I. Structure formation under negative pressures. *Journal of Structural Chemistry* **50**, 60-65, doi:10.1007/s10947-009-0190-0 (2009).

13 Conde, M. M., Vega, C., Tribello, G. A. & Slater, B. The phase diagram of water at negative pressures: Virtual ices. *The Journal of Chemical Physics* **131**, 034510, doi:10.1063/1.3182727 (2009).

14 Sloan, E. D. Gas Hydrates: Review of Physical/Chemical Properties. *Energy & Fuels* **12**, 191-196, doi:10.1021/ef970164+ (1998).

15 Jia, J., Liang, Y., Tsuji, T., Murata, S. & Matsuoka, T. Elasticity and Stability of Clathrate Hydrate: Role of Guest Molecule Motions. *Scientific Reports* **7**, doi:10.1038/s41598-017-01369-0 (2017).

16 Liyanage, L. S. I. *Running a DFT calculation in VASP.*, <https://icme.hpc.msstate.edu/mediawiki/images/d/d2/LS14_VASP.pdf.> (2012).

17 Exeter, U. o. *Density function theory for begineers*, <http://newton.ex.ac.uk/research/qsystems/people/coomer/dft_intro.html> (2020).

18 Sholl, D. S. & Steckel, J. A. *Density functional theory: a practical introduction*. (John Wiley & Sons, 2022).

19 Georg Kresse, M. M., „J¨urgen Furthm¨uller. (2018).

20 Kresse, G. & Furthmüller, J. Efficiency of ab-initio total energy calculations for metals and semiconductors using a plane-wave basis set. *Computational Materials Science* **6**, 15-50, doi:https://doi.org/10.1016/0927-0256(96)00008-0 (1996).

21 Kresse, G. & Furthmüller, J. Efficient iterative schemes for ab initio total-energy calculations using a plane-wave basis set. *Physical Review B* **54**, 11169-11186, doi:10.1103/PhysRevB.54.11169 (1996).

22 Kresse, G. & Hafner, J. Ab initio molecular dynamics for liquid metals. *Physical Review B* **47**, 558-561, doi:10.1103/PhysRevB.47.558 (1993).
23 Kresse, G. & Joubert, D. From ultrasoft pseudopotentials to the projector augmented-wave method. *Physical Review B* **59**, 1758-1775, doi:10.1103/PhysRevB.59.1758 (1999).
24 Momma, K. & Izumi, F. VESTA 3 for three-dimensional visualization of crystal, volumetric and morphology data. *Journal of Applied Crystallography* **44**, 1272-1276, doi:https://doi.org/10.1107/S0021889811038970 (2011).

# Chapter 3

# 3 Piezo-elasticity and stability limits of monocrystal methane gas hydrates: Atomistic-continuum characterization

---

*Reproduced from Zhu, X., Rey, A. D. & Servio, P. Piezo-elasticity and stability limits of monocrystal methane gas hydrates: Atomistic-continuum characterization. The Canadian Journal of Chemical Engineering* ***101****, 639-650, doi:https://doi.org/10.1002/cjce.24433 (2023). Copyright [2023] Wiley Online Library*

## Preface

As discussed in Chapters 1 and 2, gas hydrates have a variety of applications for solving the problem of energy scarcity. However, the main barrier of further exploration and development is the lack of knowledge regarding the stability and pressure effects for gas hydrates. Chapter 3 starts with established atomistic modelling of gas hydrates to determine some fundamental properties, including lattice volume, lattice energy, bulk modulus, and its first derivative value, using the most fundamental equation of state fitting. After confirming the accuracy of the results, the simulations were conducted under various pressures. During this step, the pressure effects (piezo effects) on the mechanical properties of gas hydrates were investigated, and the mechanical/pressure stability limit of the hydrate system was determined. In order to calculate the mechanical properties under pressure, it is necessary to obtain the values of the second-order elastic constants (SOECs), which provide the most fundamental information about a system under strain, as well as the input values for the Voigt-Reuss-Hill (VRH) approximation. The values of the SOECs are provided in both numeric and sensitivity factor formats. The sensitivity factors can reveal the tendency of mechanical properties to change as a result of pressure. When the system approaches its limits of stability, the sensitivity factors of SOECs deviate from their ordinary direction and magnitude. Furthermore, the intrinsic brittle and ductile features and the transition point are essential to know because they will trigger different fracture mechanisms once the system reaches its pressure limits. In summary, Chapter 3 provides an wide characterization of the response of gas hydrates to pressure, including the pressure stability limits and how the mechanical properties change under pressure. All these findings provide a solid foundation for future research on the mechanical properties of gas hydrates under pressure, as described in Chapter 4.

## 3.1 Abstract

Gas hydrates are guest-host crystalline materials formed by water cages and guest gases such as methane and carbon dioxide under simultaneously relative high-pressure and low-temperature conditions. With this unique guest-host structural feature, gas hydrates can be used for gas storage and carbon dioxide ($CO_2$) sequestration creating challenges such as flow assurance and geology stability. Some of these challenges are related to material instabilities caused by changing external conditions. Thus, this paper aims to determine the theoretical pressure stability limits of monocrystal defect-free sI methane gas hydrates at 0 K using accurate density functional theory (DFT) to simulate the hydrate's thermodynamic and elastic responses under varying pressures. The pressure stability limits are determined by Born stability criteria and piezo sensitivity factors. The important brittle-to-ductile transitions of gas hydrates are established. Also, polycrystalline mechanical properties, including the Poisson ratio and Young modulus, are calculated from the second-order elastic constants obtained from the monocrystal sI methane hydrates, which provide the upper bounds. Taken together the piezo-sensitivity of a complete set of elastic properties of sI methane gas hydrates and material stability limits determined by atomistic calculations provide new data and fundamental understanding for technological applications.

## 3.2 Introduction

Gas hydrates (GH), also known as clathrate hydrates, or simply hydrates are crystalline solids that resemble ice, and consist of water molecules encapsulating various gas molecules.[1] The lattice structure of clathrate hydrates is formed by the hydrogen bonds of water and the entire structure is stabilized by the presence of trapped gas molecules.[2] In other words, gas hydrates are clathrate compounds in which the host molecule is water, and the guest molecule is typically a gas; more than one class of gas can be present with various occupancy rates.[3] Gas hydrates are usually found in deep ocean and permafrost areas, where low temperatures and high pressures prevail.[4] 80% of natural gas hydrates contains methane as their guest molecule, providing a significant potential energy source.[5] Additionally, due to the special guest-host structural features, gas hydrates can be used for gas storage, $CO_2$ sequestration, water desalination.[6-10] However, some negative impacts may take place during these applications. In energy-related industries, flow assurance and safety problems are inevitable.[11] Potential environmental impacts of methane gas hydrates due to structural and thermodynamic instabilities need to be taken into account in climate change challenges. Driven by these issues, much effort has been made to study the gas hydrates' stability and performance under relevant pressure and temperature ranges. Unfortunately, due to the high cost and technical challenges of performing actual experiments, the mechanical properties and stability of gas hydrates under high pressures and low temperatures are incomplete, poorly characterized, and a fundamental material physics understanding is still lacking.

To overcome these challenges, some research groups use computational materials engineering modelling methods, such as molecular dynamics (MD) to simulate, characterize and shed light on the performance of gas hydrates. Khurana, M., et al.[12] demonstrates a couple of clathrate nucleation pathways based on the molecular simulations. Kondori, J., et al.[13] illustrates the methane hydrate dissociation. They validates the increasing stability of hydrate with increasing pressures and occupancy. Also, they found that during the dissociation process, new hydrogen bonds were formed, [13] which is a robust indication of structural transition. Li, Y., et al.[14] investigated the nucleation and dissociation mechanisms of $CO_2$ hydrates in the dioctahedral smectite using molecular dynamics. They found that hydrate nucleation occurred in the inter-particle pores of dioctahedral smectite, whereas clathrate-like structures were formed in the intra-particle pores. Besides the pure mechanism studies, some research group put much effort on the methane properties and production process. Zhang, Y., et al.[15] found the three conditions that would trigger hydrate phase transition in deep-sea methane hydrate-bearing soil. The three conditions are low methane hydrate saturation, significant dissipated energy and methane hydrate decomposition. [15] Kondori, J., et al.[16] summarized the methane production from the gas hydrate reservoir. They used the molecular dynamics to simulate different hydrate dissociation mechanisms and provide the crystal structures of methane hydrate in salt solutions. [16]

The unit lattice of the gas hydrate is considered as the smallest unit, and thus the detailed guest host interactions, guest effects, and cage effects are not resolved in this paper. All the results , scalings, and observations are based on the whole lattice view. The Density Functional Theory (DFT) would be used for all the simulations. To overcome the DFT limitations, the careful selection of approximation, calculation algorithm and correlated systems are discussed in Section 3.4.2. Also, considering the DFT temperature limitations, all work from this paper is under 0 Kelvin. The effect of temperature is left for future work and is outside the scope of the work.

Recent studies have mainly focused on the material properties of gas hydrates in terms of pressures, temperatures, and chemical composition (types of guest molecules). Using Density Functional Theory (DFT), Jendi et al. [17] reported that the tensile and compressive ideal strengths of sI pure methane gas hydrates are -1.10 GPa and 90 GPa, respectively. Based on molecular dynamic (MD) simulations, Jia, J. et al.[18] reported the elastic behaviour and provided molecular insights into stability changes of sI pure methane and carbon dioxide gas hydrates from -5 MPa to -150 MPa and 20 MPa to 110 MPa. sI gas hydrate has a cubic structure,[19] and only has three independent elastic constants, $C_{11}$, $C_{12}$, and $C_{44}$.[20] For methane hydrates, $C_{11}$ and $C_{12}$ decrease with increase in temperature while they increase as pressure increases. [18] However, $C_{44}$ is insensitive to pressure and decreases with increasing temperature. [18] Meanwhile, the relationships between mechanical properties and pressure and temperature were recognized. [18] For methane hydrates, the bulk modulus and Poisson's ratio increase as pressure increases and decrease as temperature increases. However, the shear modulus and Young modulus have entirely different behaviours. These two moduli do not correlate strongly with pressures for the methane hydrates, but their values decrease as temperature increases.

The previous studies [17,18,21] determined the performance of sI gas hydrates under uniaxial stress, and the dynamic trends of various mechanical properties under different pressures and temperatures were estimated. However, hydrostatic pressure is a ubiquitous stress load that needs to also be studied in addition to uniaxial stress. In this work the pressure-dependence of all elastic constants and resulting elastic moduli is referred to as piezo-elasticity, in analogy and correspondence to piezo-viscosity in liquids.[22-24] Noteworthy, for water, the viscosity first decreases with increasing pressure but eventually increases with pressure as in other liquids and polymeric fluids[25] and hence the anomalous piezo-viscosity of water reveals unique molecular bonding effects. Hence, we expect that a systematic characterization of the piezo-elasticity of GH is important and necessary to close gaps in understanding and applications. We note that in this work we consider both positive (compression) and negative pressures (expansion). Accurate predictions of mechanical properties under varying pressure loads are required for engineering design and control in addition to characterizing correlations and parametric trends.

In order to meet the engineering and environmental challenges mentioned above, this work aims to provide a complete characterization of sI pure methane gas hydrates' performance under different hydrostatic pressures at 0 K using computational materials engineering methods. In order to provide a fundamental materials physics understanding of elasticity and stability, considerations of bonding, symmetry, and chemical composition need to be explicitly and accurately integrated, hence we  employ DFT-based atomistic modelling. Related studies that support the current work in terms of selection of accurate methods, efficient computational platforms, and useful calculation techniques are available.[17,21,26-29]

More specifically, in this paper we predict pressure stability limits and mechanical properties of monocrystal defect-free methane gas hydrates, using accurate density functional theory (DFT) to simulate the hydrate's performance under varying pressures relevant to the science and technology of gas hydrates. In addition, this paper uses periodic boundary conditions and full gas occupancy, which is not observed experimentally but is required for computational tractability. Furthermore, we use the quadratic elastic energy formulation, and the imposed loads and strains corresponds to linear elasticity. The averaging procedures to convert monocrystal properties into polycrystal ones are expected to provide upper and lower bounds of elastic properties.[30] All calculations are at 0K, and hence predictions are generally upper bounds when compared to values at higher temperatures.

The organization of this paper is as follows. In section 3.5.1, the ground-state volume and energy in terms of pressures were present with the equations of state (EOS) fitting and the pressure sensitivity factor of bulk modulus. In section 3.5.2, the relationship between second-order elastic constants and hydrostatic pressures are characterized. In section 3.5.3, the Born stability criteria were applied to evaluate the theoretic pressure limits based on the second-order elastic constants values. In section 3.5.4, the polycrystalline mechanical properties calculated through the Voigt-Reuss-Hill (VRH) approximation[30] and failure modes were given, based on the second-order elastic constants of a monocrystal. The supplementary information (SI) contains all the necessary data, equations, derivations and secondary calculations that support the paper. Without ambiguity and to avoid unnecessary repetitions we do not mention pressure when plotting and discussing results as a function of pressure, since it is the only independent variable/parameter in this work.

# 3.3 MODELS AND METHODOLOGY

## 3.3.1 Lattice structure

As mentioned above, in this work the focus is the sI pure methane gas hydrate with 100 % occupancy. In one sI hydrate unit lattice, 46 water molecules form two types of cages. The small cages ($5^{12}$) contain twelve pentagonal faces, and the large cages ($5^{12}6^{2}$) contain twelve pentagonal faces and two hexagonal faces.[31] Each cage can take only one guest molecule. For the water cages, the position of water oxygen atoms can be determined by X-ray diffraction, with the positions of water hydrogen atoms proposed by Takeuchi, F. et al.[32] Following the Bernal-Fowler ice rules,[33] the adopted structure has the lowest net dipole moments. In this work, the guest molecules in our gas hydrate are placed at the cage's centre to minimize the net dipole moment. The entire configuration is maintained during the simulations. Figure 3-1 shows the structures of the small and large water cages in sI methane hydrate. The methane molecule is located at the centre of the cage.

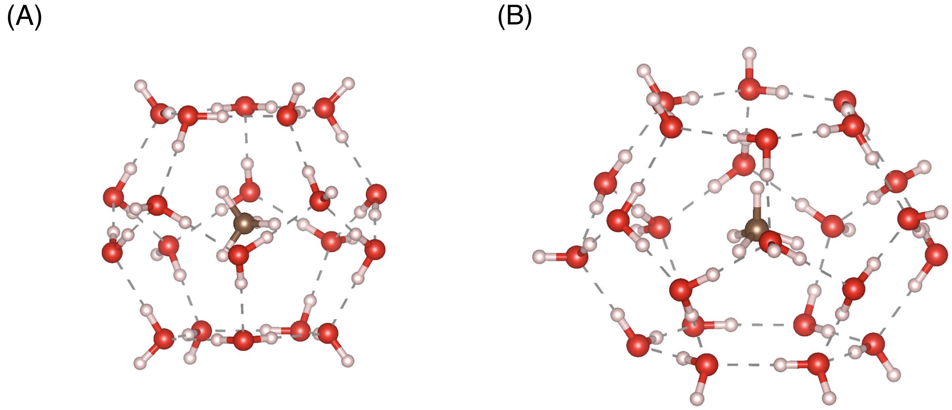

Figure 3-1 sI methane hydrate (A) small cage, which is the pentagonal dodecahedral water cage, denoted $5^{12}$ (B) large cage, which compromises 12 pentagons and 2 hexagons, denoted $5^{12}6^{2}$. Red circles represent oxygen atoms. White circles represent hydrogen atoms. Brown circles represent carbon atoms. Solid lines represent the covalent bonds between two atoms. The solid is presented with two colors (red and white), which indicate the atoms contributing to the covalent bond. The dashed lines represent the O-H hydrogen bonds.

## 3.3.2 Atomistic DFT Simulations

First principles simulations with Density Functional Theory (DFT) were utilized to investigate the performance of sI methane hydrate under different pressures. Simulations involved one unit lattice structure as discussed in the section 3.4.1. DFT simulations based on Kohn-Sham equations were performed at 0 K using a unit cell of sI methane hydrate with periodic boundary conditions. The first step was to converge the lattice to optimized geometries at different pressures allowing relaxations for the lattice volume, structural shape, and internal atomic positions. Then the energy-strain method was used to calculate the second-order elastic constants with the relaxation for internal atomic positions only.

All simulations were performed using the Vienna Ab initio Simulation Package (VASP), which conducted calculations using pseudopotentials and a plane-wave basis set. The basic methodology is the Density Functional Theory (DFT), and the hybrid functionals are applied simultaneously to compensate for any intrinsic deficits of DFT. The revPBE exchange-correlation functional and the DFT-D2 dispersion correction method were selected for this study based on the outstanding performance shown in previous studies on gas hydrates.[21,27,29] The cut-off energy was selected as 520 eV, which is 30% greater with respect to the standard values to guarantee the absolute energies are converged. $1\times10^{-4}$ eV and $5\times10^{-3}$ eV/Å were chosen as the global break conditions for the electronic self-consistent loop and the ionic relaxation respectively.

To not compromise the results' accuracy and minimize the calculation cost, the quasi-Newton and conjugate gradient algorithms were used. The quasi-Newton algorithm is time-efficient but only has a stable performance within the stable pressure range. The conjugate gradient algorithm has a stable performance under pressure; however, it requires more memory and more calculation time. The quasi-Newton algorithm was applied in the low-pressure range to maximize the time efficiency and minimize the memory cost. When pressures are approaching stability limits, the conjugate gradient algorithm was used. The lattice energy discrepancy for the same system between the two algorithms is approximately $10^{-4}$ eV, which is essentially negligible during the property calculations. This is because only the energy discrepancy between two different strained systems greater than $10^{-3}$ eV is considered for calculations. This $10^{-3}$ eV criterion can significantly reduce the calculation error from selecting the algorithm. All the key parameters used in the  simulations are summarized in Table 3-1.

During structural relaxation, the degree of freedom was controlled, and the details are shown in Supplementary Information 1 (SI1). To specify the Bloch vectors that will be used to sample the Brillouin zone in the calculation,[34] several parameters have been set. Firstly, the number of k-points are switched to the automatic generation scheme. A Gamma centered grid was applied. Four subdivisions along the reciprocal lattice vectors were selected for all directions. PAW potentials were used for generation of all the calculations in this paper.

Table 3-1 Summary of key parameters in DFT

| | |
|---|---|
| Exchange-correlation functional | revPBE+ DFT-D2 dispersion correction |
| Cut-off energy | 520 eV |
| Global break conditions the electronic self-consistent loop | $1\times10^{-4}$ eV |
| Break conditions for the ionic relaxation | $5\times10^{-3}$ eV/Å |
| Calculation algorithm | Newton and conjugate gradient algorithms |
| Number of k-points | 4 |
| Grid generation mode | Gamma centered |

### 3.3.3 Second order elastic constants (SOEC)

The second-order elastic constants (SOEC) were calculated from the energy analysis of the strained systems. While a stress-strain analysis could be applied, the energy-strain analysis is preferable and was chosen in previous studies.[21,35] Equation (1) presents the relationship between the lattice energy and the strains under constant pressures and temperatures. $E_0$ is the constant lattice energy of the unstrained system. The energy change of system due to the small strains can be determined by reducing Equation (3.1) to Equation (3.2), as shown below.

$$E = E_0 + \frac{V}{2}\sum_{i=1}^{6}\sum_{j=1}^{6} c_{ij}\delta^2 + O(\delta^4) \tag{3.1}$$

$$\Delta E = \frac{V}{2}\sum_{i=1}^{6}\sum_{j=1}^{6} c_{ij}\delta^2 + O(\delta^4) \tag{3.2}$$

where $E_0$ and V are the equilibrium energy and volume of the unstrained system, respectively. In the cubic lattice used here it is possible to choose the strains while preserving the unit cell volume. Given the cubic symmetry the number of second-order elastic constants tensor, $C_{ij}$, in the cubic structure can be reduced to three, $C_{11}$, $C_{12}$ and $C_{44}$.[20] Three linear independent combinations of strain vectors were selected to calculate these elastic constants, as shown in Supplementary Information 2 (SI2).

The second-order elastic constants can then be calculated for any pressure by using this methodology. The only difference is that the ground state energy is the energy of the unstrained system at different pressures. With the assumption of linear elasticity, the strain values were selected to vary from 0.005 to 0.03, with an increment of 0.005 to ensure the hydrate material response is in the elastic region. During the calculation of the system's total energy, the unstrained and strained systems were maintained in its initial volume and shape. Only the atomic positions were relaxed.

### 3.3.4 Engineering Sensitivity Analysis

The sensitivity analysis is designed to explore the response of the target properties as the input conditions, or the environmental conditions change. The sensitivity factor, also called parametric sensitivity, quantifies the effect of the variations of hydrostatic pressures on the property/quantity of interest, denoted as $S_Q$, where S stands for sensitivity factor and the subscript Q represents the lattice energy E, lattice volume V, elastic constants $C_{ij}$ (i,j=11,12,44), Young modulus E, shear modulus G, and Poisson ratio K. All the calculated sensitivity factor are normalized sensitivity (also called relative sensitivity), which is the product of two factors:

$$S_Q = \frac{\partial Q}{\partial P}\frac{|P|}{Q} \tag{3.3}$$

the first factor is the local sensitivity. The symbol Q is the property value at pressure P. The second factor in Equation (3.3) is the ratio P / Q. Thus, the sensitivity factor is dimensionless, and the sign of the sensitivity factor indicates whether the correlation between the quantity Q and the pressure is positive or negative. The magnitude of the sensitivity factor value indicates whether the property Q reacts significantly as the pressure changes. The closer the $S_Q$ values are to zero, the weaker the dependence to pressure. The four critical points of $S_Q$ of interest are:

Zero sensitivity: $$S_Q(P_o) = 0 \tag{3.4}$$

Diverging sensitivity: $$\lim_{P \to P_D} S_Q \to \pm\infty \tag{3.5}$$

Constant sensitivity: $$S_Q = \frac{\partial Q}{\partial P}\frac{P}{Q}\bigg|_{P_C} = C \tag{3.6}$$

Extremal sensitivity: $$\frac{\partial S_Q}{\partial P} = \frac{\partial}{\partial P}\left(\frac{\partial Q}{\partial P}\frac{P}{Q}\right)\bigg|_{P_E} = 0 \tag{3.7}$$

where C is a constant and the meaning of the four pressures $\{P_o, P_D, P_C, P_E\}$ are given in Equation (3.4-3.7) above. Zero sensitivity arises at P=0 or when $Q$ is not a function of pressure. Diverging sensitivity at $P_D$ signals loss of stability. Constant sensitivity at $P_C$ signals power law behavior such as $Q=\alpha P^n$, where α is a constant and n is the power order which equals C (See Equation (3.6)). Determining the critical pressure values $P_c$ corresponding to the critical sensitivities allows to identify the nature and number of regimes in any piezo-elastic and piezo-thermodynamic quantity. The presence of local maxima or minima signals transitions between softening and stiffening among other changes. Further technical details on evaluating $S_Q$ are given in Supplementary Information 3 (SI3).

# 3.4 RESULTS AND DISCUSSION

## 3.4.1 Ground-state energy and volume

In section 3.5.1, the ground-state energy E and lattice volume V are discussed. In section 3.5.1.1, the sensitivity factor of volume $S_V$ and sensitivity factor of energy $S_E$ are characterized. In section 3.5.1.2, the isothermal crystal equations of state (EOS) fitting were applied to determine bulk modulus and its first derivatives. Based on previous work,[21] Birch-Murnaghan and Vinet were selected for the energy-volume fitting and the sensitivity factor of bulk modulus was provided.

### 3.4.1.1 Piezo sensitivity factors of volume $S_V$ and energy $S_E$

Figure 3-2 shows the equilibrium volume V (left axis) of SI methane hydrates and the sensitivity $S_V$ (right axis). At 0 GPa, the equilibrium volume is 1662 Å$^3$. In previous work, the volume value obtained using the SIESTA platform under 0 GPa and 0K was 1684 Å$^3$ and the small 1.3% difference establishes the accuracy of the present method. [21]

The equilibrium volumes were determined by the Energy-Volume (E-V) curves with the precision of 1 meV for energy and 1 Å$^3$ for volume under constant pressures. The overall response is a monotonically decreasing volume with a divergence under expansion. Under expansion, the lattice volume increased significantly. The slope of the curve at -1.1 GPa nearly diverges, which represents the lattice loss of integrity if additional stress was applied. A dramatic increase in the lattice volume implies that the average atomic length becomes too long to maintain intermolecular bonds. On the compressive side, the volume decreases at a decreasing rate, indicating increase resistance under volume reduction. From a volumetric criterion the structural lattice remained stable under 6 GPa.

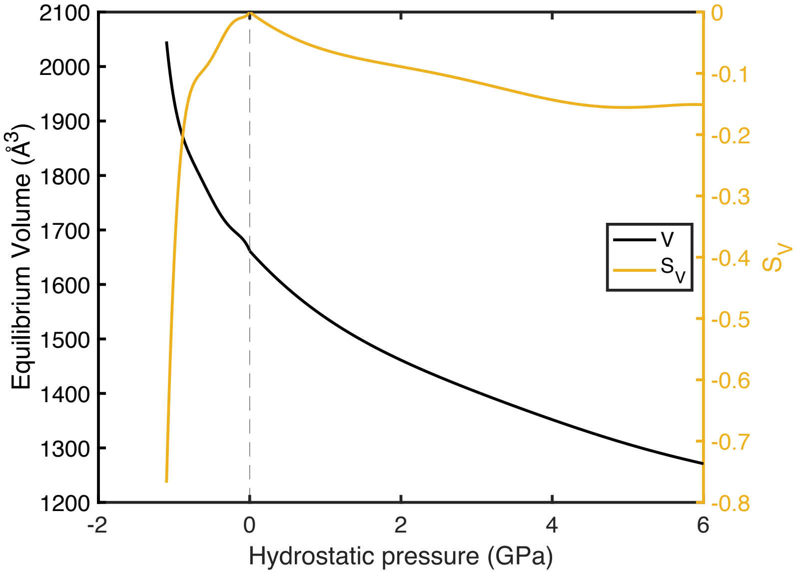

Figure 3-2 Equilibrium volume and $S_V$ vs. Hydrostatic pressures. Black solid curve represents the volume-pressure curves. Yellow solid curve represents the sensitivity factor of volume $S_V$. S stands for sensitivity factor and subscript V stands for Volume. The same nomenclature is applied for all the sensitivity factors in this paper. A grey vertical dashed line shows at zero shows the boundary between the tensile and compressive pressures.

The values of sensitivity vector $S_V$ in the entire range are negative as expected due to the negative relationship between volume and pressure. The magnitude of $S_V$ ranges from 0 to 0.8. The three critical pressures (GPa) values of $S_V$ are $\{P_0 = 0, P_D = -1.1, P_C = 4.5\}$ and hence we have three regions: (i) near instability region, high $\partial S_V / \partial P$ under expansion, (ii) intermediate region with small $\partial S_V / \partial P < 0$, and (iii) plateau region, $\partial S_V / \partial P = 0$. The response of $S_V$ shows that expansion eventually leads to instability while compression up to 6 GPa leads to a stable state with $S_V$ around -0.15. The piezo-choric sensitivity factor $S_V$ captures expected trends but provides specific values for the three mode transitions.

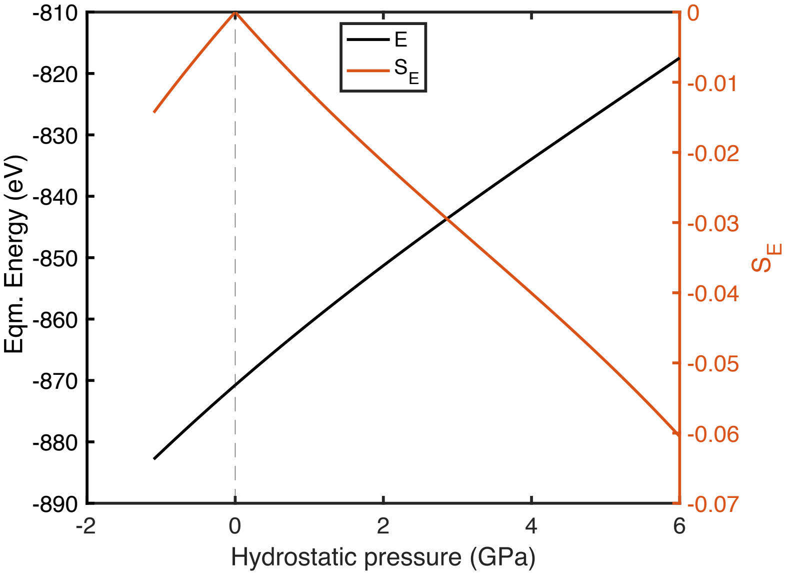

Figure 3-3 Equilibrium energy and sensitivity of equilibrium energy in terms of hydrostatic pressures. The black solid line represents the equilibrium energy values at different pressures. The orange line is the piezo sensitivity factor of equilibrium energy. The vertical grey dashed line shows the boundary between compressive and tensile stress.

Figure 3-3 shows the equilibrium energy E and its sensitivity factor $S_E$. The equilibrium energy E monotonically increases with pressure since strain increases. The only critical pressures (GPa) value of $S_E$ is $\{P_o=0\}$ and hence we have two regions: (i) expansion with a linear $\partial S_E / \partial P > 0$, (ii) compression with a linear $\partial S_E / \partial P < 0$. From -1.1 GPa to 6 GPa, the value of $S_E$ is always negative with a magnitude of $S_E$ of the order of $10^{-2}$. Using the DFT data and engineering sensitivity factor $S_E$ gives the following scaling, shown in Equation (3.8a-3.8b),

$$S_{E\pm} = 0.01P \tag{3.8a}$$

$$E(eV) = -870.76e^{0.01P} = -870.76 \pm (870.76 \times 0.01P_{\pm}) \tag{3.8b}$$

where ± refers to compression and expansion and P (GPa) is the signed pressure values. The sensitivity factor is linear and weakly dependent on pressure and the energy is essentially linear in pressure. The magnitude of $S_E$ ranges between 0 and 0.6.

### 3.4.1.2 Birch-Murnaghan and Vinet Equations of state fitting

Equations of state (EOS) are commonly used to find the bulk elasticity modulus B.[21] There are three widely used equations of state to evaluate the material's bulk modulus and its derivatives: Murnaghan, Birch-Murnaghan and Vinet equations,[36] which are defined in Supplementary Information 4 (SI4). The main difference among them is the assumption made on the pressure-derivatives of the bulk modulus. Murnaghan equation of state assumes the bulk modulus is linearly correlated with pressure, and its first derivative is a constant. This assumption limits the Murnaghan equation accuracy to low-pressure regions.[37] The Birch-Murnaghan equation is based on an expansion of the free energy in terms of the Eulerian strain.[36] It assumes that both bulk modulus and its first derivative are functions of the pressures. Vinet equation makes the same assumption as the Birch-Murnaghan, but it is based on an empirical potential.[36] Considering the extreme pressures applied in this project the Birch-Murnaghan and Vinet EOS were both used.

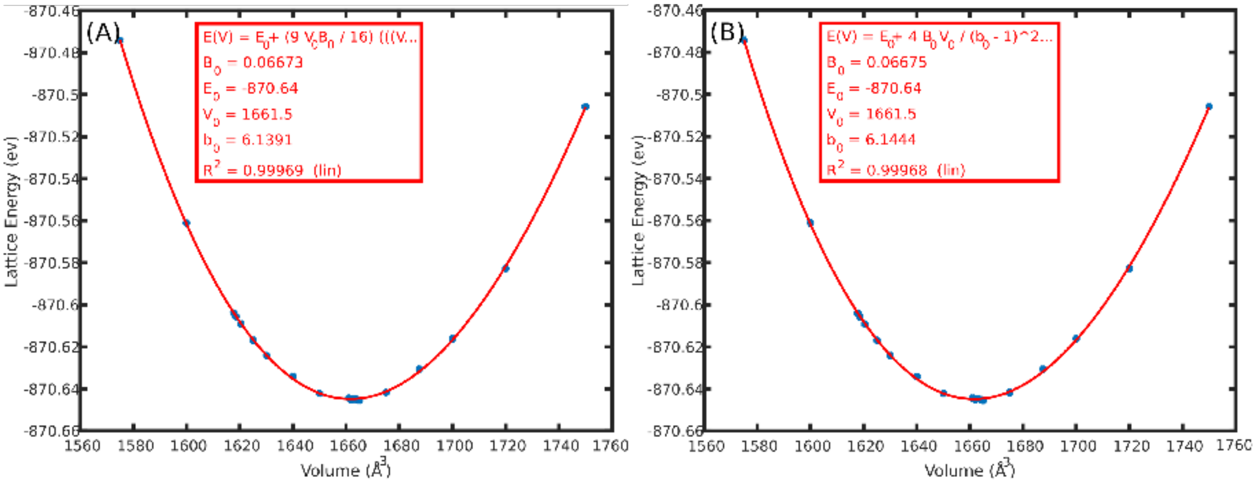

Figure 3-4 Equations of state fitting at 0 GPa under 0 K (A) Birch-Murnaghan (B) Vinet The blue dots are the raw data points, and the red curve is the fitting line based on the selected EOS. In the red box, the equations of selected EOS are shown. The following four fitting parameters $B_0$, $E_0$, $V_0$ and $b_0$ are bulk modulus, equilibrium energy, equilibrium volume and the first derivative of bulk modulus. $R^2$ is a coefficient of determination, which is 0.99969 and 0.99968 respectively. The unit of bulk modulus shown in the box is eV/Å$^3$.

Figure 3-4 shows the Birch-Murnaghan and Vinet EOS fittings. Both equations fit the DFT data very well and attain $R^2$ values of 0.999. The equilibrium volume and equilibrium energy are the same from the two equations. The bulk modulus B is 10.69 GPa from both EOS. Compared with the results from other simulation papers at 0 K and 0 GPa, 9.82 GPa,[21] 8.3 GPa,[38] and 9.98 GPa,[39] the results generated for this paper is very close to those reported. From the E-V fitting aspect, there is no preference of the Birch-Murnaghan equation or Vinet equation. Both show that sI methane hydrate follows the general material rules very well and its properties can be calculated from the established EOS. In this work the Birch-Murnaghan EOS was selected for calculation the bulk modulus B and sensitivity factor $S_B$ as a function of pressure:

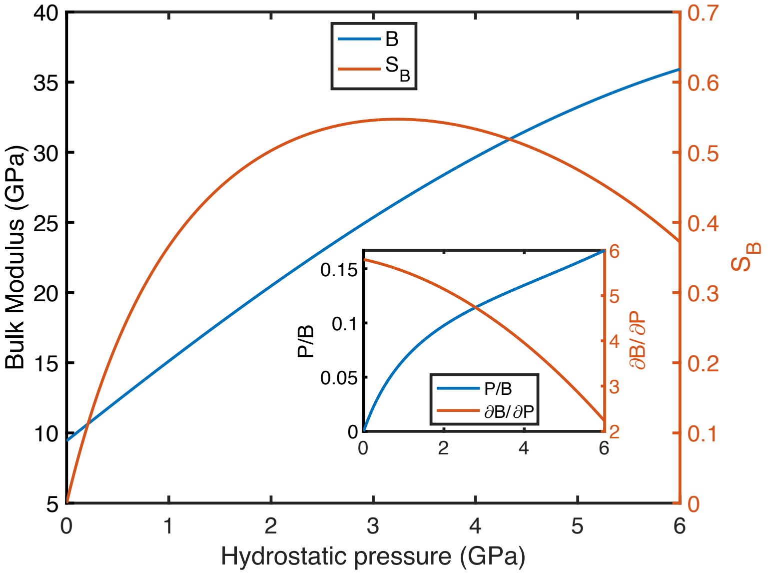

Figure 3-5 Bulk modulus and its sensitivity factor in terms of hydrostatic pressures. The blue and orange curves represent the bulk modulus values and its sensitivity factor calculated from Birch-Murnaghan, respectively.

Figure 3-5 shows the bulk modulus B and its piezo sensitivity factor $S_B$. The bulk modulus B shows an increasing trend throughout from 0 GPa to 6 GPa. The piezo sensitivity factor of bulk modulus $S_B$ is shown as the orange parabolic curve and shows a local maximum around $P_E$= 3.23

GPa. In this pressure range we do not see different modes as in $S_E$ (see Figure 3-3) and in $S_V$ (see Figure 3-2) but we found an extremal sensitivity point. The trends of the bulk modulus curve ($\partial B/\partial P$) and of the ratio of pressure and bulk modulus (P/B) are opposite, as shown in the inset of Figure 5. When the pressure is less than 3 GPa, the ratio between the pressure and bulk modulus dominates $S_B$. As the pressure increases, the pressure tendency of the bulk modulus B determines the performance of bulk modulus sensitivity factor $S_B$. Using standard definitions, we find the relations between bulk modulus B and volume sensitivity $S_V$, as shown in the Equation (3.9a-3.9b):

$$B = -\frac{P}{S_V} \tag{3.9a}$$

$$S_B = 1 - S_{S_V} = 1 - \frac{|P|}{S_V} \cdot \frac{\partial S_V}{\partial P} \tag{3.9b}$$

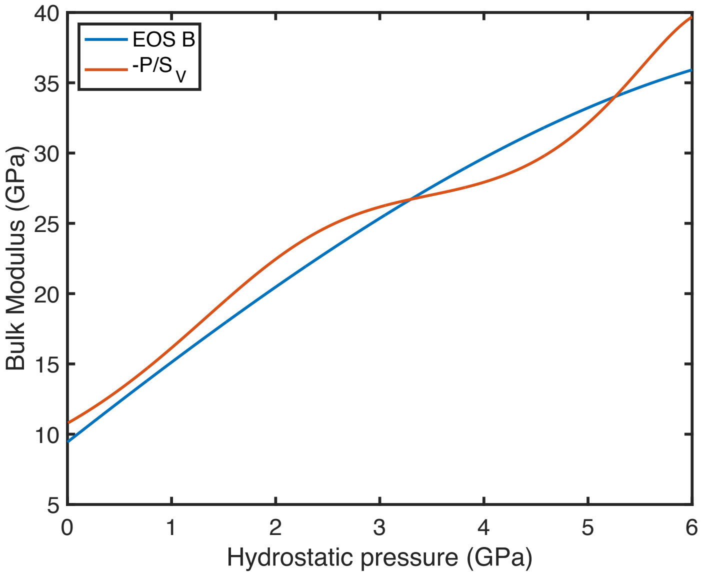

Figure 3-6 Bulk modulus calculated from EOS predictions (blue curve) and from thermodynamic derivations (orange curve)

Figure 3-6 shows the bulk modulus obtained from the EOS and from thermodynamics, establishing an important internal consistency between the two methods. Since the sensitivity of

B ($S_B$) is a function of the second order sensitivity of the volume ($S_{S_V}$), we can expect a local maximum in $S_B$ from the additional product factors $\left(P / S_V\right) \cdot \left(\partial S_V / \partial P\right)$ at $P_E$. Calculating $\partial S_B / \partial P = 0$ gives the following differential equation, Equation (3.10):

$$S_V \frac{\partial S_V}{\partial P} - P\left(\frac{\partial S_V}{\partial P}\right)^2 + S_V\, P \frac{\partial^2 S_V}{\partial P^2} = 0 \tag{3.10}$$

The simplest possible linear fit around the critical value $P_E$, such as $S_V = \alpha P_E$ satisfies the above equation and hence predicts a local maximum in $S_B$.

Taken together, the results indicate that the increase of B with pressure reaches a maximum at intermediate pressures ($P_E$) beyond which the resistance to compression becomes weaker ($\partial B / \partial P < 0$).

### 3.4.2 Piezo sensitivity factors of second-order elastic constants, $S_{C_{ij}}$

Second-order elastic constants are fundamental properties that are used to calculate the polycrystalline mechanical moduli (see Supplementary Information 5 (SI5)). In this section, the values of second-order elastic constants and their sensitivity factors are characterized. As mentioned above for sI methane hydrate, there are three independent second-order elastic constants: $C_{11}$, $C_{12}$ and $C_{44}$.

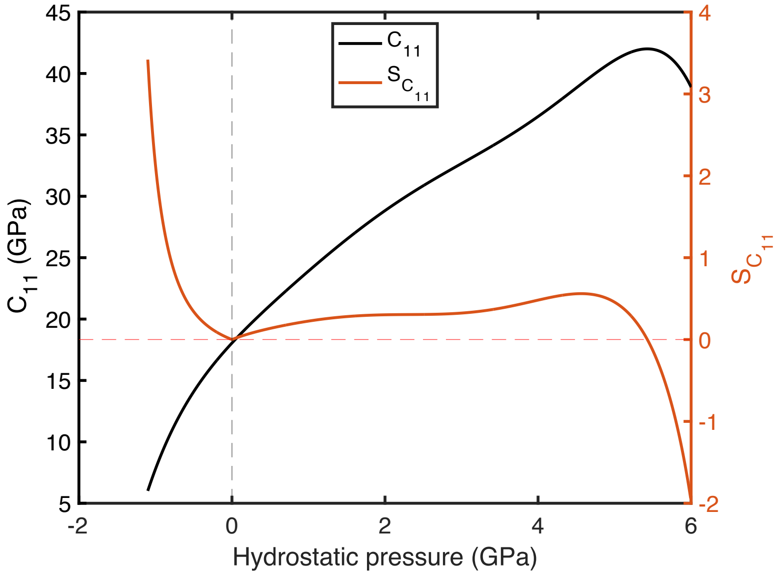

Figure 3-7 $C_{11}$ and $S_{C_{11}}$ in terms of hydrostatic pressures. The black curve represents $C_{11}$ values along with pressures. The orange curve is for the sensitivity factor of $C_{11}$ along with the pressures. The vertical grey dashed line at x=0 shows the boundary between tensile and compressive pressures. The horizontal orange line at y=0 presents if it is a positive or negative correlation between $S_{C_{11}}$ and pressures.

Figure 3-7 shows $C_{11}$ and sensitivity factor $S_{C11}$. $C_{11}$ presents an increasing trend with pressure until the compressive pressure reaches pressures of the order of 5 GPa. At approximately 5.2 GPa, $C_{11}$ reaches its maximum value and then decrease as the compressive pressures increase; this anomalous behaviour can be recognized as an indication of structural instability. The behaviour of $S_{C_{11}}$ shows three regimes defined by $P_o$=0 and $P_E$=5GPa and two critical divergences around $P_D$= -1 GPa and $P_D$ = 6 GPa. $S_{C_{11}}$ gives different responses for the compressive and tensile pressures. Similar to $S_V$, $S_{C_{11}}$curve diverges when the tensile pressure approaches approximately -1 GPa. The only discrepancy is that $S_{C_{11}}$ is always positive on the tensile side, however, $S_V$ is always negative. The positive $S_{C_{11}}$ indicate that the values of $S_{C_{11}}$ increase as the pressures increase. The magnitude of the values shows how reactive $C_{11}$ is to the applied pressures. On the compressive side, $S_{C_{11}}$ shows a mildly increasing trend, where the values are always below 1. At 5 GPa, $S_{C_{11}}$values start to decrease upon larger pressure loads. When the pressure reaches about

5.5 GPa, $S_{C_{11}}$ crosses the horizontal zero line, which means that the initial positive correlation between $S_{C_{11}}$ and hydrostatic pressures is replaced by a negative correlation. This inverse response or reaction can be recognized as an indication of instability.

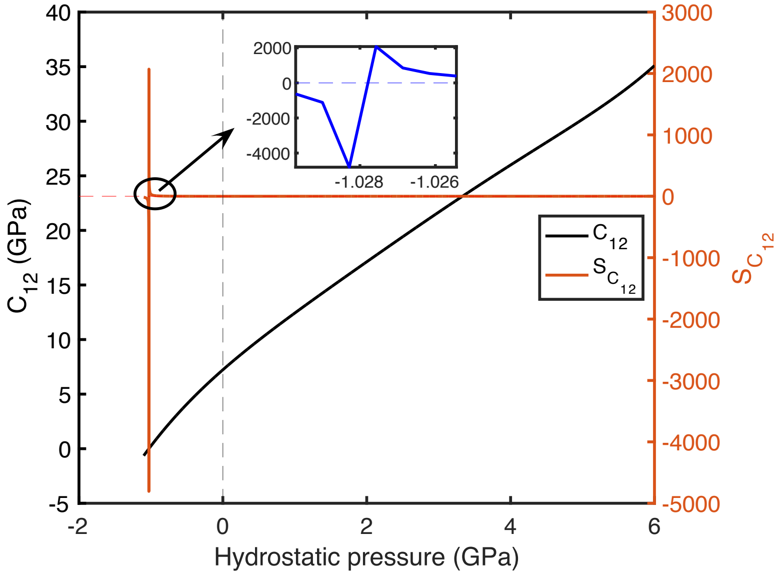

Figure 3-8 $C_{12}$ and $S_{C_{12}}$ in terms of hydrostatic pressures. The black curve represents $C_{12}$ values along with pressures. The orange curve is for the sensitivity factor of $C_{12}$ along with the pressures. The vertical grey dashed line at x=0 shows the boundary between tensile and compressive pressures. The horizontal orange line at y=0 presents if it is a positive or negative correlation between $S_{C_{12}}$ and pressures. A zoom-in figure is shown around -1 GPa to capture the sign change of $S_{C_{12}}$.

Figure 3-8 shows $C_{12}$ and $S_{C_{12}}$. $C_{12}$ shows a monotonic increasing trend up to a pressure of -1.1 GPa where $C_{12}$ becomes negative, which implies that the lattice structure became unstable. This is because $C_{12}$ shares the same numerical sign with Poisson ratio. Physically, Poisson ratio should be positive except for auxetics.[40] As gas hydrate is a high-dense material, it does not have the feature of auxetics and thus the $C_{12}$ value should be positive in the stable region. The behaviour of $S_{C_{12}}$ is relatively stable throughout the entire pressure range. Only near the region of -1 GPa, a sudden sign change of $C_{12}$ value takes place thus the $S_{C_{12}}$ value shows a significant value change.

The inset figure shows that near -1.028 GPa, $S_{C_{12}}$ sign changes and becomes negative, and it is the pressure value at which $C_{12}$ becomes negative as well. Thus, the $S_{C_{12}}$ is a robust indicator of the variation of $C_{12}$. Integrating $C_{11}$ and $C_{12}$ results using the standard relations, the bulk modulus and its sensitivity factor can be expressed as Equation (3.11a-3.11b):

$$B = -\frac{P}{S_V} = \frac{1}{3}(C_{11} + 2C_{12}) \tag{3.11a}$$

$$S_B = \left(\frac{1}{1+2R}\right)\left(S_{C_{11}} + 2RS_{C_{12}}\right); R = \frac{C_{12}}{C_{11}} \tag{3.11b}$$

We conclude that under a $P > 0$, the monotonic increase in B (see Figure 3-5) is a reflection of similar trends in $C_{11}$ (see Figure 3-7) and $C_{12}$ (see Figure 3-8) and that bulk sensitivity $S_B$ is a weighted nonlinear combination of the elementary sensitivities $\left(S_{C_{11}};S_{C_{12}}\right)$ and the elasticity ratio $R = C_{12}/C_{11}$ whose variability results in a local maximum for B, shown as Equation (3.11a-3.11b).

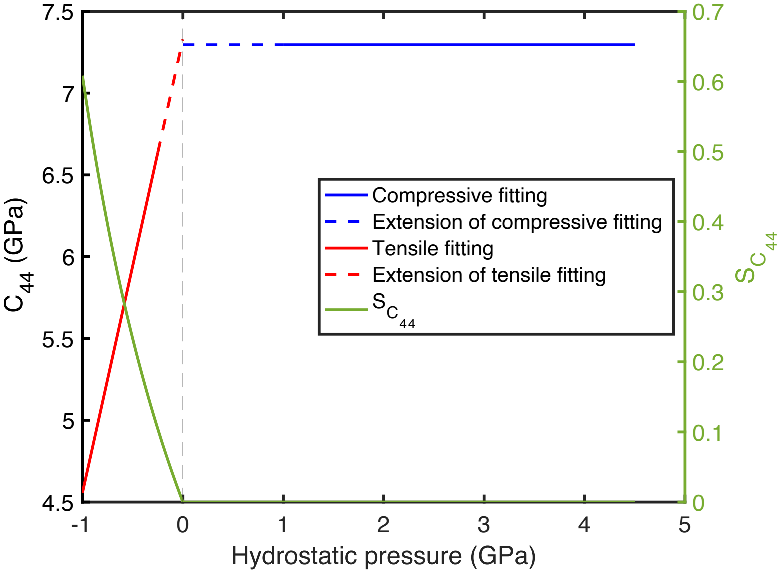

Figure 3-9 $C_{44}$ and $S_{C_{44}}$ in terms of hydrostatic pressures. The blue and red solid lines represent $C_{44}$ values along with tensile and compressive pressures respectively. The blue and red dashed lines are the extension from the corresponding solid fitting lines. The green solid curve is the $S_{C_{44}}$. The vertical grey dashed line at x=0 shows the boundary between tensile and compressive pressures.

Figure 3-9 shows the values of $C_{44}$ and its sensitivity factor in terms of pressures from -1.1 GPa to 4.5 GPa. Different from $C_{11}$ and $C_{12}$, the DFT predictions of $C_{44}$ do not show a robust monotonic response in the low-pressure region on both tensile and compressive sides (indicated by dashed lines) and only values from 1 GPa to 4.5 GPa and from -0.25 GPa to -1 GPa are considered. Based on previous work,[18,41] $C_{44}$ is insensitive to compressive pressures but negatively correlates with temperature. Shimizu, H., et al. [41] reported the $C_{44}$ for SI methane is a constant value of 3.6 GPa under 270K. Taken in consideration also the results from Jia, J., et al.,[18], the $C_{44}$ value under 0 K predicted here should be greater than 3.6 GPa[41]. After careful consideration of DFT raw data, the previous predictions and measurements, [18,41] the $C_{44}$ response is found to be linear under dilation and a constant of 7.2 GPa under compression.

### 3.4.3 Born stability criteria

The Born stability criteria[42] was used to characterize material stability through the second-order elastic constants. If one of these criteria is violated, it indicates material failure. The pressure range for $C_{11}$ and $C_{12}$ ranges from -1 GPa to 6 GPa. The criteria involving $C_{44}$ is restricted to -1 GPa to 4.5 GPa to ensure accuracy. Under material cubic symmetry, there are three stability criteria[43], shown as Equation (3.12-3.14):

$$C_{44} - P > 0 \tag{3.12}$$

$$C_{11} - P > |C_{12} + P| \tag{3.13}$$

$$C_{11} + 2C_{12} + P > 0 \tag{3.14}$$

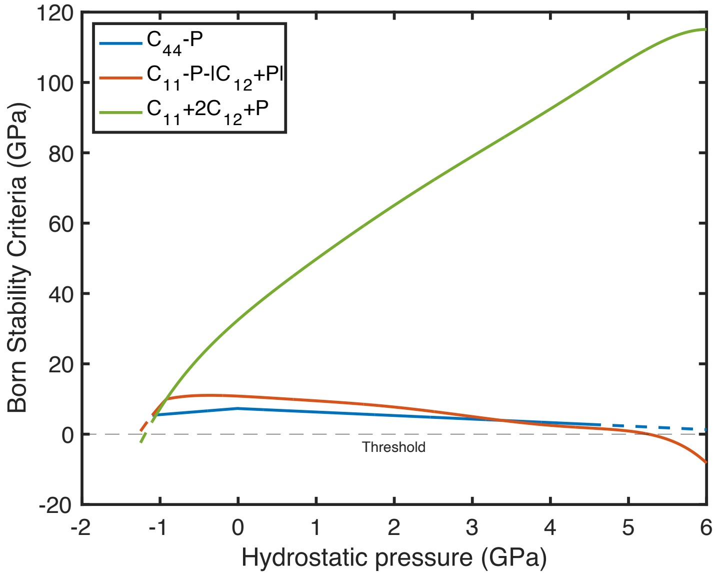

Figure 3-10 Born stability criteria according to Equation (3.12-3.14). The horizontal dotted line is the zero critical line. The figure shows that under dilation all criteria tend to fail and that under compression the dominant failure is from Equation (3.13).

Figure 3-10 presents the values of Born stability criteria. Criteria (3.12-3.13) follow similar weakly decreasing trend just above zero in contrast to the increasing trend of criterion 14 away from zero. The latter is a consequence that even under extension the sum is always positive due to the magnitudes of $C_{11}$ and $2C_{12}$. Since $C_{44}$ is relatively small the -P effect forces $C_{44}$-P to always be close to zero. Similarly, the comparable magnitudes of $C_{11}$ (see Figure 3-7) and $C_{12}$ (see Figure 3-8) results in $(C_{11} - P) - |C_{12} + P| \approx \varepsilon > 0$, where ε is a small number. Figure 3-10 shows that under extension Criterion 14 breaks down first and under compression Criterion 13 breaks down first. The green dashed line crossed the threshold at approximately -1.2 GPa which agrees with the volumetric behaviour under -1.2 GPa, where the volume diverges (see Figure 3-2). The dominant breakdown (criterion 3.13) under compression around 4.5 GPa is in good agreement with $S_{C11}$ (see Figure 3-7).

### 3.4.4 Mechanical properties and Failure Modes

The mechanical properties are calculated from the second order elastic constants using the Voigt-Reuss-Hill (VRH) approximation[44] shown in Supplementary Information 6 (SI6). All the properties were assessed and validated at zero pressure with available theoretical, modelling, and experimental data. The present predictions are consistent with previous reports, as shown in Supplementary Information 5 (SI5).

In this section, we investigate the ductile-to-brittle transition of sI methane hydrate under increasing pressure. The ductile and brittle material features will lead to different failure mechanism. We use these data in conjunction with elastic constants $C_{12}$ and $C_{44}$ to predict the failure modes of sI methane using the Pugh and Pettifor criteria.[45] The Pettifor criterion states that the ratio $(C_{12}-C_{44})/E$ must be greater than 0 if the material is ductile, which means $C_{12}$ has to be greater than $C_{44}$. The Pugh criterion states that if the G/B ratio is greater than 0.57, then the material is recognized as brittle. Figure 3-11 shows the results evaluated from the Pugh and Pettifor criteria. From the Pettifor criterion aspect, the ductile-to-brittle transition takes place at zero pressure. When the tensile pressure is applied, the hydrate becomes brittle. From the Pugh criterion, the transition is at 0.083 GPa. This means that the very low-compressive region (from 0 GPa to 0.083 GPa) is recognized as brittle as well.

To consider the effect of shape deformation on the ductile-to-brittle transition, another parameter, the Zener anisotropy ratio (A) is used to characterize shape changes under pressure. For the Pugh criterion, instead of a specific threshold at 0.57, it becomes a range from 0.42 to 0.6 to incorporate the shape deformation effect. In Figure 3-12, the Pugh criterion is shown as the grey and red dashed line located at G/B =0.42 and 0.6. These two numbers correspond to the A=9 and 1, respectively. A=1 and 9 represents the isotropic and highly anisotropic materials. Also, the difference ($C_{12}$-$C_{44}$) is normalized by B instead of E. This is because that based on the Equation (S13-S15), there is a linear relationship between ($C_{12}$-$C_{44}$)/B and G/B, which is shown in Figure 3-12. For sI gas hydrate system, when ($C_{12}$-$C_{44}$)/B=0, its G/B values is approximately 0.6 (red dashed line). This performance further indicates the isotropic nature of sI gas hydrate material.

In summary we can conclude that the piezo effects could affect the sI methane hydrate system's ductile/brittle feature. Under compressive conditions, the system shows a brittle behaviour and under tensile conditions, it has a ductile feature. If there is no pressure applied, based on the results shown in Figure 3-11, we concluded that it is brittle.

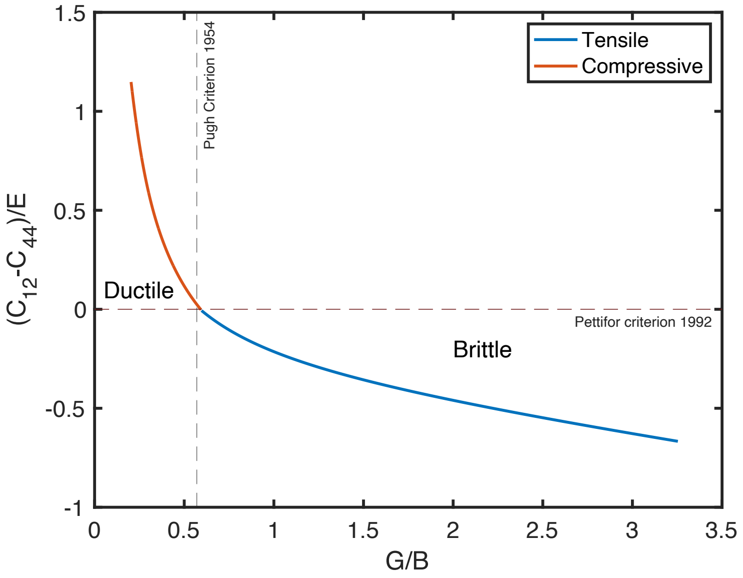

Figure 3-11 A renormalized correlation between ($C_{12}$-$C_{44}$) normalized by Young modulus E and G/B. The vertical grey dashed line corresponds to G/B=0.57 and the horizontal red dashed line corresponds to ($C_{12}$-$C_{44}$)/E =0. The blue curve represents the results obtained under tensile pressures and the orange curve represents the results obtained under compressive pressures.

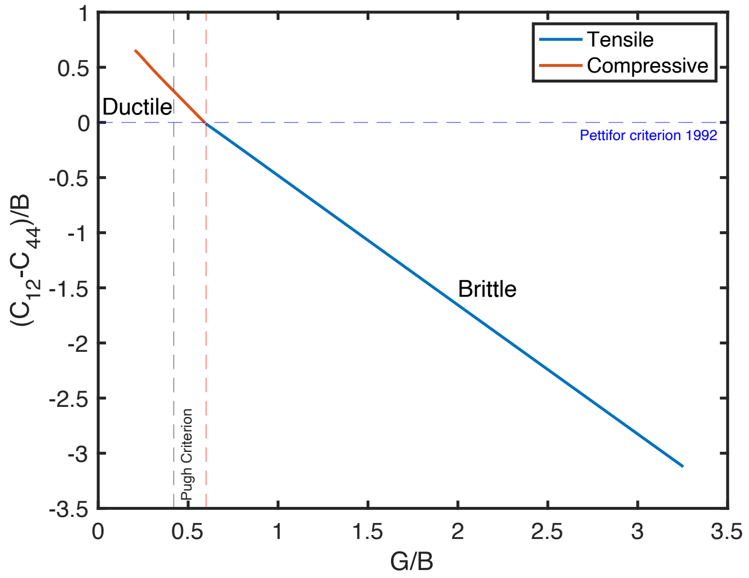

Figure 3-12 A renormalized correlation between ($C_{12}$ -$C_{44}$) normalized by bulk modulus B and G/B. The horizontal dashed line corresponds to ($C_{12}$ -$C_{44}$) /B =0. The vertical band corresponds to G/B in the range of 0.42 to 0.6 to account for the effect of elastic anisotropy on the value of G at $C_{12}$ -$C_{44}$= 0. The blue curve represents the results obtained under tensile pressures and the orange curve represents the results obtained under compressive pressures.

## 3.5 Conclusions

In conclusion, this paper characterizes the tensile and compressive pressure limits of sI methane hydrates at 0 K through a systematic atomistic computational methodology and a theoretical methodology. Pressure load extrema are found at -1 GPa and 5.5 GPa respectively. The generic Born stability criteria was implemented to evaluate the system's stability and the mechanical properties were determined within the stable pressure range. The Birch-Murnaghan and Vinet Equation of state are applied to determine the material bulk modulus. Additionally, piezo sensitivity factors were applied to capture the intrinsic responses and used to connect atomistic calculations with engineering sensitivity.

The results from this paper fill the knowledge gap of mechanical properties of sI methane hydrates under pressure. The theoretical pressure limits provide ideal bounds for crack nucleation under monocrystal conditions. In addition, the inability to maintain a cubic lattice structure on the tensile side at -1.1 GPa and the anomalous behaviour of second-order elastic constants at 6 GPa indicate the failure mechanisms are completely different under tensile and compressive stresses. In addition, the results obtained from piezo sensitivity factors, summarized in various critical points and scaling behaviours, can be used in future engineering applications

# 3.6 Reference

1 Englezos, P. Clathrate hydrates. **32**, 1251-1274, doi:10.1021/ie00019a001 (1993).

2 Sloan Jr., E., Koh, C., Koh, C. . Clathrate Hydrates of Natural Gases., 752 pages (2007).

3 Dillon, W. P. in *Encyclopedia of Physical Science and Technology (Third Edition)* (ed Robert A. Meyers) 473-486 (Academic Press, 2002).

4 Ruppel, C. D. Methane Hydrates and Contemporary Climate Change. *Nature Education Knowledge 3(10):29* (2011).

5 Council of Canadian Academies. Expert Panel on Gas, H. (Council of Canadian Academies = Conseil des académies canadiennes, Ottawa, 2008).

6 M.D. Max & R.E. Pellenbarg. U.S. Patent No. 5,873,262 patent 5873262 (1999).

7 M.D. Max & R.E. Pellenbarg. U.S. Patent No. 6,158,239 patent 6158239 (2000).

8 Max, M. D. U.S. Patent No. US2003/0024803 A1 patent USOO6733667B2 (2003).

9 M.D. Max. U.S. Patent No. US2005/0184010 A1. patent (2005).

10 Koh, C. A., Sloan, E. D., Sum, A. K. & Wu, D. T. Fundamentals and applications of gas hydrates. *Annu Rev Chem Biomol Eng* **2**, 237-257, doi:10.1146/annurev-chembioeng-061010-114152 (2011).

11 Sloan, D. in *Natural Gas Hydrates in Flow Assurance* (eds Dendy Sloan *et al.*) 1-11 (Gulf Professional Publishing, 2011).

12 Khurana, M., Yin, Z. & Linga, P. A Review of Clathrate Hydrate Nucleation. *ACS Sustainable Chemistry & Engineering* **5**, 11176-11203, doi:10.1021/acssuschemeng.7b03238 (2017).

13 Kondori, J., Zendehboudi, S. & James, L. New insights into methane hydrate dissociation: Utilization of molecular dynamics strategy. *Fuel* **249**, 264-276, doi:https://doi.org/10.1016/j.fuel.2019.02.125 (2019).

14 Li, Y. *et al.* Nucleation and dissociation of carbon dioxide hydrate in the inter- and intra-particle pores of dioctahedral smectite: Mechanistic insights from molecular dynamics simulations. *Applied Clay Science* **216**, 106344, doi:https://doi.org/10.1016/j.clay.2021.106344 (2022).

15 Zhang, Y. *et al.* Molecular Dynamics Simulation of the Effects of Methane Hydrate Phase Transition on Mechanical Properties of Deep-Sea Methane Hydrate-Bearing Soil. *Advances in Civil Engineering* **2021**, 1-10, doi:10.1155/2021/3716891 (2021).

16 Kondori, J., Zendehboudi, S. & Hossain, M. E. A review on simulation of methane production from gas hydrate reservoirs: Molecular dynamics prospective. *Journal of Petroleum Science and Engineering* **159**, 754-772, doi:https://doi.org/10.1016/j.petrol.2017.09.073 (2017).

17 Jendi, Z. M., Servio, P. & Rey, A. D. Ideal Strength of Methane Hydrate and Ice Ih from First-Principles. *Crystal Growth & Design* **15**, 5301-5309, doi:10.1021/acs.cgd.5b00829 (2015).

18 Jia, J., Liang, Y., Tsuji, T., Murata, S. & Matsuoka, T. Elasticity and Stability of Clathrate Hydrate: Role of Guest Molecule Motions. *Scientific Reports* **7**, 1290, doi:10.1038/s41598-017-01369-0 (2017).

19 McMullan, R. K. & Jeffrey, G. A. Polyhedral Clathrate Hydrates. IX. Structure of Ethylene Oxide Hydrate. *The Journal of Chemical Physics* **42**, 2725-2732, doi:10.1063/1.1703228 (1965).

20 Jamal, M., Jalali Asadabadi, S., Ahmad, I. & Rahnamaye Aliabad, H. A. Elastic constants of cubic crystals. *Computational Materials Science* **95**, 592-599, doi:https://doi.org/10.1016/j.commatsci.2014.08.027 (2014).

21 Jendi, Z. M., Rey, A. D. & Servio, P. Ab initio DFT study of structural and mechanical properties of methane and carbon dioxide hydrates. **41**, 572-579, doi:10.1080/08927022.2014.899698 (2015).

22 Chkadua, O. & Natroshvili, D. Localized boundary-domain integral equations approach for Dirichlet problem of the theory of piezo-elasticity for inhomogeneous solids. *Memoirs on Differential Equations and Mathematical Physics* **60**, 73-109 (2013).

23 Chkadua, O. & Natroshvili, D. Localized boundary-domain integral equations approach for Robin type problem of the theory of piezo-elasticity for inhomogeneous solids. *Memoirs on Differential Equations and Mathematical Physics* **65**, 57-91 (2015).

24 Talekar, N. & Kumar, P. Steady State EHL Line Contact Analysis with Surface Roughness and Linear Piezo-viscosity. *Procedia Materials Science* **5**, 898-907, doi:https://doi.org/10.1016/j.mspro.2014.07.377 (2014).

25 Singh, L. P., Issenmann, B. & Caupin, F. Pressure dependence of viscosity in supercooled water and a unified approach for thermodynamic and dynamic anomalies of water. *Proceedings of the National Academy of Sciences* **114**, 4312, doi:10.1073/pnas.1619501114 (2017).

26 Mathews, S. L., Servio, P. D. & Rey, A. D. Heat Capacity, Thermal Expansion Coefficient, and Grüneisen Parameter of CH4, CO2, and C2H6 Hydrates and Ice Ih via Density Functional Theory and Phonon Calculations. *Crystal Growth & Design* **20**, 5947-5955, doi:10.1021/acs.cgd.0c00630 (2020).

27 Daghash, S. M., Servio, P. & Rey, A. D. First-Principles Elastic and Anisotropic Characteristics of Structure-H Gas Hydrate under Pressure. *Crystals* **11**, doi:10.3390/cryst11050477 (2021).

28 Mirzaeifard, S., Servio, P. & Rey, A. D. Molecular Dynamics Characterization of Temperature and Pressure Effects on the Water-Methane Interface. *Colloid and Interface Science Communications* **24**, 75-81, doi:https://doi.org/10.1016/j.colcom.2018.04.004 (2018).

29 Vlasic, T. M., Servio, P. & Rey, A. D. Atomistic modeling of structure II gas hydrate mechanics: Compressibility and equations of state. *AIP Advances* **6**, 085317, doi:10.1063/1.4961728 (2016).

30 Hill, R. The Elastic Behaviour of a Crystalline Aggregate. *Proceedings of the Physical Society. Section A* **65**, 349-354, doi:10.1088/0370-1298/65/5/307 (1952).

31 Sloan, E. D. Fundamental principles and applications of natural gas hydrates. *Nature* **426**, 353-359, doi:10.1038/nature02135 (2003).

32 Takeuchi, F. *et al.* Water proton configurations in structures I, II, and H clathrate hydrate unit cells. *The Journal of Chemical Physics* **138**, 124504, doi:10.1063/1.4795499 (2013).

33 Ryzhkin, I. & Petrenko, V. Phase transition of an ice-proton system into a Bernal-Fowler state. *Phys. Rev. B* **62**, doi:10.1103/PhysRevB.62.11280 (2000).

34 Georg Kresse, M. M., „J¨urgen Furthm¨uller. (2018).

35 Zhao, J., Winey, J. M. & Gupta, Y. M. First-principles calculations of second- and third-order elastic constants for single crystals of arbitrary symmetry. *Physical Review B* **75**, 094105, doi:10.1103/PhysRevB.75.094105 (2007).

36 Cohen, R. E., Guelseren, O., Hemley, R. J. & Carnegie Institution of Washington, D. C. Accuracy of equation-of-state formulations. *American Mineralogist* **85**, doi:10.2138/am-2000-2-312 (2000).

37 Stacey, F. D., Brennan, B. J. & Irvine, R. D. Finite strain theories and comparisons with seismological data. *Geophysical surveys* **4**, 189-232, doi:10.1007/BF01449185 (1981).

38 Miranda, C. R. & Matsuoka, T. FIRST-PRINCIPLES STUDY ON MECHANICAL PROPERTIES OF CH4 HYDRATE. (2008).

39 Huo, H. *et al.* Mechanical and thermal properties of methane clathrate hydrates as an alternative energy resource. *Journal of Renewable and Sustainable Energy* **3**, 063110, doi:10.1063/1.3670410 (2011).

40 Cho, H., Seo, D. & Kim, D.-N. in *Handbook of Mechanics of Materials* (eds Siegfried Schmauder *et al.*) 733-757 (Springer Singapore, 2019).

41 Shimizu, H., Kumazaki, T., Kume, T. & Sasaki, S. Elasticity of single-crystal methane hydrate at high pressure. *Phys. Rev. B* **65**, doi:10.1103/PhysRevB.65.212102 (2002).

42 Born, M. Thermodynamics of Crystals and Melting. *The Journal of Chemical Physics* **7**, 591-603, doi:10.1063/1.1750497 (1939).

43 Sin$rquot$ko, G. V. & Smirnov, N. A. Ab initio calculations of elastic constants and thermodynamic properties of bcc, fcc, and hcp Al crystals under pressure. *Journal of Physics: Condensed Matter* **14**, 6989-7005, doi:10.1088/0953-8984/14/29/301 (2002).

44 Grimvall, G. r. (Elsevier, Amsterdam, Netherlands ;, 1999).

45 Senkov, O. N. & Miracle, D. B. Generalization of intrinsic ductile-to-brittle criteria by Pugh and Pettifor for materials with a cubic crystal structure. *Scientific reports* **11**, 4531, doi:10.1038/s41598-021-83953-z (2021).

46 M. B. Helgerud, W. F. W., S. H. Kirby, and A. Nur. Correction to ‘‘Elastic wave speeds and moduli in polycrystalline ice Ih, sI methane hydrate, and sII methane-ethane hydrate’’. *JOURNAL OF GEOPHYSICAL RESEARCH, VOL. 114, B04299*, doi:10.1029/2009JB006451 (2009).

# 3.7 Supplementary Information (SI)

## 3.7.1 Degrees of Relaxation (SI1)

This supplementary information SI1 summarizes the control on the degrees of relaxation during simulation used in Section 3.4.2 of the paper. To calculate the second-order elastic constants of a material there should be a control of the degrees of freedom during the relaxation. The description of different degrees of freedom and the steps of relaxation to obtain the second-order elastic constants are shown below.

First, the degrees of relaxation are controlled by the ISIF tag. The following table demonstrates the meaning of ISIF.

| ISIF | Relaxations | Change cell shape | Change cell volume |
|---|---|---|---|
| 2 | Yes | No | No |
| 3 | Yes | Yes | Yes |
| 4 | Yes | Yes | No |

Steps for relaxation:

1. Relax the unit lattice with ISIF=3 for a complete relaxation
2. Copy the CONTCAR to POSCAR, then rerun the job with ISIF=3 to minimize the Pulay errors
3. Copy the CONTCAR to POSCAR, then set ISIF=4 to generate the E-V curve
4. Determine the equilibrium volume from the E-V curve.

5. Use CONTCAR file at the equilibrium volume as a POSCAR template. Apply the strained system on the unit lattice with the POSCAR template and set ISIF=2.
6. With the energy of the strained system and the known strains, the three independent second-order elastic constants can be calculated.

### 3.7.2 Strained system (SI2)

The supplementary information SI2 summarizes the strained sets used to prepare the strained system in Section 3.4.3 of the paper.

The [100] and [010] strains were applied, which gives

$$\Delta\mathrm{E} = \mathrm{V}(\mathrm{C}_{11} + \mathrm{C}_{12})\delta^2 + \mathrm{O}(\delta^4) \tag{3.S1}$$

$$\varepsilon = \begin{bmatrix} \delta & 0 & 0 \\ 0 & \delta & 0 \\ 0 & 0 & 0 \end{bmatrix}$$

The tetragonal strains were applied, and the changes of the total energy from its unstrained system can give $(\mathrm{C}_{11} - \mathrm{C}_{12})$

$$\Delta\mathrm{E} = \mathrm{V}(\mathrm{C}_{11} - \mathrm{C}_{12})\delta^2 + \mathrm{O}(\delta^4) \tag{3.S2}$$

$$\varepsilon = \begin{bmatrix} \delta & 0 & 0 \\ 0 & -\delta & 0 \\ 0 & 0 & \dfrac{\delta^2}{1-\delta^2} \end{bmatrix}$$

The value of $\mathrm{C}_{44}$ was computed using the following strains.

$$\Delta\mathrm{E} = \frac{\mathrm{V}}{2}\mathrm{C}_{44}\delta^2 + \mathrm{O}(\delta^4) \tag{3.S3}$$

$$\varepsilon = \begin{bmatrix} 0 & \dfrac{\delta}{2} & 0 \\ \dfrac{\delta}{2} & 0 & 0 \\ 0 & 0 & \dfrac{\delta^2}{4-\delta^2} \end{bmatrix}$$

### 3.7.3 Polynomial fitting and Sensitivity factors ($S_Q$) Evaluation (SI3)

This supplementary information SI3 gives the key calculations needed to execute the sensitivity analysis used in Section 3.4.4 of the paper.

In this paper, it is assumed that the all the properties are only dependent on the pressures. This is because that the mechanical properties are usually only related to temperatures and pressures. In this paper, all the simulation performed under 0 K. Thus, the property Q is a function of pressures:

$$Q = Q(P) \tag{3.S4}$$

To describe the relationship between the elastic properties and pressures a polynomial fitting was applied. Due to intrinsic numerical accuracy limits and after extensive parametric studies it is found that the maximum order for polynomial fitting to be use is six orders. For this paper, six order polynomial fitting is enough since the $R^2$ is greater than 0.99. Then Equation (3.S4) can be expressed as Equation (3.S5):

$$Q(P) = aP^6 + bP^5 + cP^4 + dP^3 + eP^2 + fP + g \tag{3.S5}$$

where a-g are coefficients.

To capture the piezo-choric effect, a piecewise polynomial fitting. It was applied to V to capture both the tensile and compressive responses. Thus, to determine the relationship between the equilibrium volume and hydrostatic pressures, two polynomial equations from -1.1 GPa to 0 GPa (expansion) and another one is from 0 GPa to 6 Gpa (compression) were established. The values 0.25 GPa and 0.5 GPa were selected as the increments on the tensile and compressive sides respectively. On the compressive region, 0.1 GPa was used for the pressures from 0 GPa to 0.5

GPa to capture the changes in the low-pressure region. The adopted pressure increments followed extensive parametric studies and capture accurately the piezo-choric effect.

To capture the local sensitivity $\partial \mathrm{Q_j}/\partial \mathrm{P_j}$, the central difference is used for interior data points and a forward or backward difference is applied on the edges, shown as Equation (3.S6-3.S8):

$$\frac{\partial \mathrm{Q_j}}{\partial \mathrm{P_j}} = 0.5\ \times \frac{(\partial \mathrm{Q_{j+1}} - \partial \mathrm{Q_{j-1}})}{\Delta \mathrm{P}} \tag{3.S6}$$

$$\frac{\partial \mathrm{Q_1}}{\partial \mathrm{P_1}} = \frac{\partial \mathrm{Q_1} - \partial \mathrm{Q_1}}{\Delta \mathrm{P}} \tag{3.S7}$$

$$\frac{\partial \mathrm{Q_N}}{\partial \mathrm{P_N}} = \frac{\partial \mathrm{Q_N} - \partial \mathrm{Q_N}}{\Delta \mathrm{P}} \tag{3.S8}$$

The subscript j varies between 2 and N-1. $\Delta$P is the spacing between two pressure points. The target property $Q_j$ value can be calculated from Equation (3.S5) at pressure $P_j$. Since the second component of sensitivity factor is generated, the sensitivity factor value can be calculated for each point to generate a curve in terms of pressures.

## 3.7.4 EOS fitting (SI4)

This supplementary information SI4 presents all the equations of state discussed in the Section 3.5.1.2 of the paper.

Murnaghan:

$$\Delta \mathrm{E(V)} = \mathrm{B_0 V_0}\left[\frac{1}{\mathrm{B_0'(B_0'-1)}}\left(\frac{\mathrm{V}}{\mathrm{V_0}}\right)^{1-\mathrm{B_0'}} + \frac{\mathrm{V}}{\mathrm{B_0' V_0}} - \frac{1}{\mathrm{B_0'}-1}\right] \tag{3.S9}$$

Birch-Murnaghan:

$$\Delta \mathrm{E(V)} = \frac{9\mathrm{B_0 V_0}}{16}\left\{\left[\left(\frac{\mathrm{V_0}}{\mathrm{V}}\right)^{\frac{2}{3}} - 1\right]^3 \mathrm{B_0'} + \left[\left(\frac{\mathrm{V_0}}{\mathrm{V}}\right)^{\frac{2}{3}} - 1\right]^2 \left[6 - 4\left(\frac{\mathrm{V_0}}{\mathrm{V}}\right)^{\frac{2}{3}}\right]\right\} \tag{3.S10}$$

Vinet:

$$\Delta \mathrm{E(V)} = \frac{4\mathrm{B_0 V_0}}{(\mathrm{B_0'}-1)^2} - \frac{2\mathrm{B_0 V_0}}{(\mathrm{B_0'}-1)^2}\left\{5 + 3\mathrm{B_0'}\left[\left(\frac{\mathrm{V}}{\mathrm{V_0}}\right)^{\frac{1}{3}} - 1\right] - 3\left(\frac{\mathrm{V}}{\mathrm{V_0}}\right)^{\frac{1}{3}}\right\} \exp\left\{-\frac{3}{2}(\mathrm{B_0'}-1)\left[\left(\frac{\mathrm{V}}{\mathrm{V_0}}\right)^{\frac{1}{3}} - 1\right]\right\} \tag{3.S11}$$

$$\Delta \mathrm{E(V)} = \mathrm{E(V)} - \mathrm{E(V_0)} \tag{3.S12}$$

## 3.7.5 Mechanical properties calculations (VRH approximation) (SI5)

This supplementary information 5 presents all the definitions of elastic properties used in Section 3.5.2 and Section 3.5.4 of the paper.

Shear moduli:

$$\mathrm{G_{Reuss}} = \frac{5(\mathrm{C_{11}}-\mathrm{C_{12}})\mathrm{C_{44}}}{4\mathrm{C_{44}}+3(\mathrm{C_{11}}-\mathrm{C_{12}})} \quad (3.S13)$$

$$\mathrm{G_{Voigt}} = \frac{(\mathrm{C_{11}}-\mathrm{C_{12}}+3\mathrm{C_{44}})}{5} \quad (3.S14)$$

$$\mathrm{G} = \frac{\mathrm{G_{Reuss}}+\mathrm{G_{Voigt}}}{2} \quad (3.S15)$$

Bulk moduli:

$$\mathrm{B} = \mathrm{B_{Voigt}} = \mathrm{B_{Reuss}} = \frac{(\mathrm{C_{11}} + 2\mathrm{C_{12}})}{3} \quad (3.S16)$$

Poisson’s ratio:

$$\mathrm{v} = \frac{\frac{3}{2}\mathrm{B}-\mathrm{G}}{\mathrm{G}+3\mathrm{B}} \quad (3.S17)$$

Young’s modulus:

$$\mathrm{E} = 2\mathrm{G}(1 + \mathrm{v}) \quad (3.S18)$$

Longitudinal wave speed:

$$\mathrm{V_p} = \left(\frac{\mathrm{B}+\frac{4}{3}\mathrm{G}}{\rho}\right)^{\frac{1}{2}} \quad (3.S19)$$

Transverse wave speed:

$$\mathrm{V_s} = \left(\frac{\mathrm{G}}{\rho}\right)^{\frac{1}{2}} \quad (3.S20)$$

Zener anisotropy ratio:

$$A_z = \frac{2C_{44}}{C_{11} - C_{12}} \qquad (3.S21)$$

Since all the mechanical properties shown are calculated from the monocrystals, the values in Table 3-2 can provide a bound for each parameter.

Table 3-2 Mechanical properties of sI methane hydrate

| | This work[a] | Ref. [21] theo.[a] | Ref. [38] theo.[a] | Ref. [39] theo.[a] | Ref.[46] exp.[b] |
|---|---|---|---|---|---|
| $\rho$ (kg·m$^{-3}$) | 956.172 | 943 | 890 | 910 | 924.35. |
| B (GPa) | 10.754 | 9.82 | 8.3 | 9.98 | 8.39±0.01 |
| G (GPa) | 5.753 | 6.23 | 4.3 | 4.62 | 3.541±0.0008 |
| $\nu$ | 0.273 | 0.238 | 0.2776 | 0.299 | 0.3151±0.0002 |
| E (GPa) | 14.647 | 15.4 | 11.07 | 12.01 | - |
| $V_p$ (km·s$^{-1}$) | 4.390 | 4.386 | 3.981 | 4.205 | 3.766±0.002 |
| $V_s$(km·s$^{-1}$) | 2.453 | 2.571 | 1.964 | 2.25 | 1.957±0.0002 |

Note: [a] Results generated under 0 K and 0 GPa; [b] results for 0 °C and extrapolated to 0 GPa from 30.5-97.7 MPa with 3%, ± 6%, ± 4%, ± 3%, ± 1.5%, and ± 1.5% uncertainty in $\rho$, B, G, $\nu$, $V_p$, and $V_s$, respectively.

Table 3-2, presents the mechanical properties of sI methane hydrate at 0 K and under 0 GPa. Three groups of previous theoretical results and one group of experimental results were selected for comparison and validation. Firstly, for all the parameters, the values obtained from this work are in the same magnitude as the other theoretical and experimental results. Except for the Poisson ratio, the other theoretical values are always larger than the experimental values. It is reasonable since all the theoretical values are upper limits. The minor differences verify the accuracy of the methodology used to obtain the results. Thus, this VRH approximation is applied to the pressurized conditions from -1 GPa to 4.5 GPa. All the results are shown in SI6.

## 3.7.6 Polycrystalline Mechanical Properties (SI6)

This supplementary information SI6 presents the polycrystalline mechanical properties mentioned in Section 3.5.4 of the paper

| Pressure(GPa) | ρ (kg·m$^{-3}$) | B (GPa) | G (GPa) | ν | E (GPa) | $V_p$ (km·s$^{-1}$) | $V_s$(km·s$^{-1}$) |
|---|---|---|---|---|---|---|---|
| -1 | 811.9092 | 2.7537 | 4.2216 | - | 8.3816 | 3.2132 | 2.2803 |
| -0.75 | 865.0019 | 5.3043 | 4.9552 | 0.1438 | 11.3357 | 3.7108 | 2.3934 |
| -0.5 | 904.6824 | 7.4208 | 5.5456 | 0.2009 | 13.3190 | 4.0467 | 2.4759 |
| -0.25 | 935.0127 | 9.2322 | 6.0458 | 0.2312 | 14.8876 | 4.3006 | 2.5428 |
| 0 | 959.0800 | 10.8349 | 6.4899 | 0.2504 | 16.2293 | 4.5077 | 2.6013 |
| 0.1 | 967.4857 | 11.4340 | 6.4933 | 0.2612 | 16.3794 | 4.5571 | 2.5907 |
| 0.2 | 975.3731 | 12.0144 | 6.5117 | 0.2705 | 16.5458 | 4.6064 | 2.5838 |
| 0.3 | 982.8394 | 12.5792 | 6.5283 | 0.2788 | 16.6964 | 4.6535 | 2.5773 |
| 0.4 | 989.9676 | 13.1308 | 6.5437 | 0.2863 | 16.8346 | 4.6986 | 2.5710 |
| 0.5 | 996.8270 | 13.6711 | 6.5585 | 0.2932 | 16.9629 | 4.7421 | 2.5650 |
| 1 | 1028.7546 | 16.2537 | 6.6279 | 0.3205 | 17.5044 | 4.9386 | 2.5382 |
| 1.5 | 1058.8032 | 18.6990 | 6.6782 | 0.3404 | 17.9033 | 5.1059 | 2.5114 |
| 2 | 1087.2312 | 21.0251 | 6.6802 | 0.3564 | 18.1214 | 5.2470 | 2.4788 |
| 2.5 | 1113.0278 | 23.2296 | 6.6194 | 0.3699 | 18.1357 | 5.3666 | 2.4387 |
| 3 | 1135.5304 | 25.3343 | 6.5149 | 0.3816 | 18.0016 | 5.4736 | 2.3953 |

| | | | | | | | |
|---|---|---|---|---|---|---|---|
| 3.5 | 1155.2471 | 27.3975 | 6.4193 | 0.3913 | 17.8629 | 5.5789 | 2.3573 |
| 4 | 1173.8832 | 29.4933 | 6.3952 | 0.3989 | 17.8924 | 5.6911 | 2.3341 |
| 4.5 | 1193.5728 | 31.6588 | 6.4567 | 0.4045 | 18.1370 | 5.8084 | 2.3258 |

# Chapter 4

# 4 Multiscale Piezoelasticity of Methane Gas Hydrates: From Bonds to Cages to Lattices

---

*Reprinted with permission from Zhu, X., Rey, A. D. & Servio, P. Multiscale Piezoelasticity of Methane Gas Hydrates: From Bonds to Cages to Lattices. Energy & Fuels, doi:10.1021/acs.energyfuels.2c01024 (2022).Copyright [2022] American Chemical Society*

## 4.1 Preface

As discussed in Chapter 3, the tensile and compressive stability pressure limits of methane gas hydrates are -1.1 GPa and 7.5 GPa, respectively. These results have been successfully validated from several aspects, such as the DFT simulation results, sensitivity factors and Born stability criteria. These values are the result of averaging all local lattice elements. In other words, they do not represent any local pressure response within the lattice. Specifically, there are areas that are less resistant to pressure, but these characteristics will be averaged out when the mechanical properties are calculated. Thus, Chapter 4 approaches the stability study of gas hydrates from a structural perspective and establishes the connection between the structural response and the values determined in Chapter 3. In Chapter 4, a novel multi-scale analysis in terms of atoms, molecules, cages, and lattices was implemented. Combining the results of Chapter 3 with those of Chapter 4, the electron density distribution under -1.1 GPa, 0 GPa and 7.5 GPa was generated, which shows the difference between the electronic cloud movement under compressive and tensile pressures. For the purpose of studying intermolecular and intramolecular interactions, distributions of bond lengths and bond angles with respect to pressure were generated. At -1.1 GPa and 7.5 GPa, the bond length and angle distribution functions showed clearly abnormal behaviours. In addition, it was revealed that cages respond differently to tensile and compressive pressures. This further verifies the findings of Chapter 3 about the ductile-to-brittle transition. Finally, the findings of this chapter indicates that small and large cages have widely different levels of resistance to compressive pressures, which could influence lattice elasticity. At this stage, the law of mixtures was applied. The results indicate that the bulk modulus derived from Chapter 3 is consistent with that obtained from the general law of mixture. This consistency explains how each element in the lattice contributes to the change of mechanical properties under pressure. In summary, Chapter 4 performs a multiscale structural analysis of the gas hydrate under pressure and determines that the law of mixture is the link between structural changes and mechanical properties. This chapter offers a novel approach to analyzing piezo effects from structural aspect, which shows that the system does have local characteristics under pressure. Considering the calculation of second-order elastic constants in Chapter 3, the higher-order elastic constant may capture and quantify these local characteristics and piezo effects, which is discussed in Chapter 5. In addition, the application of law of mixtures at the end of this chapter implies the segregated heterogeneous structure of gas hydrates. This relevant geometric analysis and stability are illustrated in Chapter 6.

## 4.2 Abstract

For the past several decades, natural gas, also called methane gas, has been recognized as a green energy resource. It can generate energy by burning and produces fewer pollutants and carbon dioxide than coal and petroleum. For these reasons, it is also being viewed as a bridge fuel to renewable energy. Conservative estimates suggest that 80% of the naturally occurring hydrates on the planet contains natural gas. This vast amount translates to approximately twice the amount of energy stored in fossil fuels and oils. In addition, the special guest-host structure of gas hydrates provides a significant storage capacity, which makes the hydrate become a competitive candidate for carbon dioxide sequestration. However, the hydrates' instability during exploration becomes the biggest barrier for the methane gas extraction and carbon dioxide sequestration. Thus, to overcome this barrier, this paper aims to investigate the stability limits and study the piezo-effect of sI methane gas hydrates at 0 Kelvin.

This work investigates the structure, thermodynamics and elasticity sI methane hydrates subjected to pressure loads, at three scales, atoms, cages, and lattice by using density functional theory (DFT) in conjunction with homogenization methods and the theory of mixtures.The distribution functions of bond parameters are characterized in the hydrate system, which provides a novel understanding on the spread of values at the smallest scale. The roles of different types of cages at the mesoscale have been identified, such as continuous phase and disperse inclusion. At the continuum scale, the different deformation mechanisms are observed (affine and non-affine), which corresponds to different fracture mechanisms (brittle and ductile) under tensile and compressive pressures, respectively.

Taken together, the systematic atomic-cage-lattice multiscale characterization proves fruitful in linking processes that connect mechanical properties, cage geometry, and hydrogen bonding. The multi-scale methodology can be generalized to other gas hydrates to improve the fundamental understanding and obtain engineering correlations.

## 4.3 Introduction

Gas hydrates, known as clathrate hydrates, are crystalline solids that resemble ice.[1] They usually appear in the deep ocean and permafrost area, under relatively high pressures and low temperatures.[2] Gas hydrates consist of water molecules and gas molecules.[1] Compared with pure ice, these additional gas molecules contribute to a new structure. The water molecules will form the host cages, and the gas molecules will play the role of guest.[3,4] This special guest-host structure can create a significant gas storage capacity. Generally, 1 $m^3$ of gas hydrate can store 160 $m^3$ gases.[5] The most common gas molecules encapsulated in the gas hydrates are methane and carbon dioxide. Conservative estimates suggest that 80% of gas hydrates contains methane as the guest molecules, which are called natural gas hydrates.[6] Methane is a high-energy gas, which can generate a great amount of energy with relative lower greenhouse gas (GHG) emissions. However, the unburned methane gas has 84 times greater global warming potential than the carbon dioxide.[7] It is reported that the energy contained in the natural hydrates is twice the amount of energy contained in the fossil fuel throughout the world.[8] Considering the problems of energy scarcity and global warming, gas hydrates become competitive and environmental friendly candidates to meet ever increasing energy demand. However, so far there is no significant large-scale exploration for gas hydrates, where challenges include mechanical stability and structural integrity. Another aspect of these gas hydrates that continues to receive attention is the ability to store carbon dioxide thus providing a capture mechanism that can be coupled to the source of methane, creating a potential null process. However, the main challenge of this technology is the inadequate information on the stability of hydrate system under varying mechanical loads. In summary, technology-scale uses of gas hydrates for storage and recovery of methane and carbon dioxide, as well as containers for transportation requires mechanical property profiles across complex stress loads, in addition to better characterized thermodynamic phase diagrams. In this work, we focus on the impact of pressure loads across scales, from bonds to lattices and on the ideal stability limits under both dilation and compression.

Next, we identify some areas lacking a complete fundamental understanding and opportunities that arise by using a multiscale modeling approach. Focusing on the geometric features of methane gas hydrates, we find that the cubic unit lattice of methane gas hydrate (MGH) is composed of six large tetrakaidecahedra ($5^{12}6^{2}$; 12 pentagonal and two hexagonal faces) and two small pentagonal dodecahedra ($5^{12}$, twelve pentagonal faces) or a cage number ratio of three. As a result, the large cages form continuous columnar structures in the three lattice directions while the smaller cages are isolated, but attached to the larger one through their common pentagonal faces. Thus, at the cage length scale, we can consider this material as a binary composite, with a continuous (large cage) phase and a disperse (small cage) phase, whose elasticity can then be captured by the laws of mixtures. At equilibrium, the pentagonal and hexagonal faces formed by hydrogen bonds have different distortion levels in terms of bond lengths and angles to accommodate guest-host constraints, with the latter known to be higher than the former.[9] The presence of pentagonal dodecahedron reflects the fact that the ideal bond valence angle of $108^{\circ}$ is very close to the value of $109.45^{\circ}$ expected in ideal tetrahedrally bonded network and also indicates the need of other cage polyhedra.[10] In addition, the presence of guest methane in both small and large cages introduce molecular interaction gradients, since the cages are structurally different. Taken together the cage geometry, distribution of hydrogen bond angles and lengths, and host-guest interaction create an asymmetric environment, whose response to increasing externally imposed stress loads needs to be determined and established using atomistic simulations coupled with engineering coarse graining methods such as rule of mixtures for material properties. To shed light on material stability limits due to both compression and dilation one needs to consider changes in distributions of hydrogen bond lengths and angles, non-affine distortions of the small and large cages, together with macroscopic ideal strength criteria based on second order elasticity inequalities and brittle-ductile modes.

Previous simulation work on gas hydrate (GH) thermodynamic, mechanical, and interfacial properties have been performed at different scales, including atomic, cage and lattice. Mathews, S. L., et al.[11] studied several thermal properties of gas hydrates via an integrated approach of Density Functional Theory (DFT) with photon calculations. This study proposed a method to obtain the macroscopic results under different temperatures based on the atomistic simulations under 0 K. This paper shows that DFT predictions have a better accuracy under low temperatures, compared with Molecular Dynamics (MD). Also, they proposed that the results from DFT can be used as an input for MD,[11] since experimental data is mainly used as the only input for MD calculations. Jendi, Z. M., et al.[12] calculated the ideal strengths under pressures from first-principles calculations. This study found that the bond angles and lengths of water molecules are similar to the hexagonal ice (Ih). Additionally, this paper demonstrates that the perfect ice is 1.5 times stronger than perfect hydrate crystals. However, the polycrystalline hydrates is 20 times stronger than the polycrystalline ice. In addition, our previous DFT work[13] showed that the stability limits of sI monocrystal methane hydrates at 0 Kelvin are -1.1 GPa and 5.5 GPa under tensile and compressive pressures. The results[13] from piezo sensitivity factors indicated that the volume, second-order elastic constants, and bulk modulus would change their sensitivities significantly on approaching the stability limits. Vlasic, T. M., et al.[14] shows the elastic and acoustic properties of sII gas hydrate with different guest molecules using DFT. They found the single-guest hydrates were less resistant to shear stresses than double-guest hydrates. Also, they found the large cage are more compressible than the small cage. Additionally, the existence of compensation mechanism in the water system has been confirmed in hydrate system as well as by Vlasic, T. M., et al.[14]. Daghash, S. M., et al.[15-17] demonstrated the elastic properties and anisotropic characteristics of sH gas hydrates with different guest molecules under pressures through atomistic calculations. Also, the compensation mechanism has been verified in sH hydrates. Mirzaeifard, S., et al. established the models of water and methane hydrate crystal interface from multiscale computations,[18] and investigated the temperature and pressure effects on the interface by using molecular dynamics.[19] Xu, K., et al.[20] evaluated the structural and mechanical stability of hydrates by examining classical molecular dynamic simulations. They showed that the elastic moduli, such as Young's modulus and tensile strength, evolve non-linearly under pressures. Also, Xu, K., et al.[20] found that two failure mechanisms exist in the hydrate system depending on the size and nature of the guest molecules.

Most previous computational studies on hydrates' properties focus mainly on a single scale but the crucial connections between bonds, cages, and lattices remains poorly characterized. To fill this gap, this paper seeks to establish these connections by using well-established DFT methods previously used for GH, information transfer from lower to higher scales, and materials engineering coarsening methods. The key issues for this paper are (i) to capture and characterize how the bond and cage geometry impact the cages and lattice mechanical properties under increasing pressures, from dilation to compression states, and (ii) to generate a quantitative understanding of controlling mechanisms of stability thresholds of methane gas hydrates under expansion and compression.

This study only considers sI methane hydrate with 100% occupancy under pressure at 0 K. In real life, the hydrate occupancy is approximately 85%,[21] and the hydrate's stability will decrease as the occupancy decreases. To further investigate the piezo-mechanical response, the pressure range studied is from -1.1 GPa to 7.5 GPa, which can be achieved by using the DFT methods. All the simulation parameters setting and calculation algorithms have been verified by our previous work. [13,16,22,23] The positive pressure value indicates the compressive pressures, and vice versa. Temperature effects and guest chemistry other than methane are out of the scope of this paper. Results are presented and discussed in Section 4.5. The organization of this paper is summarized in Figure 4-1. In section 4.5.1, the electron density distributions under different pressures are characterized. In section 4.5.2, the bond parameters distributions (e.g. bond lengths and bond angles) are determined as a function of pressure. In section 4.5.3, the deformation of cages is established. In section 4.5.4, the role of each cage in the unit lattice and the rules of mixtures for elastic property predictions is demonstrated. The Supplementary Information (SI) includes the following: SI1 provides the detailed simulation parameters (associated with section 4.4.1). SI2 presents the bond and electron density calculations (associated with section 4.4.2). SI3 gives a detailed explanation on the electron cloud density (associated with section 4.5.1). SI4 demonstrate the bond parameters evolution under pressures (associated with section 4.5.2).

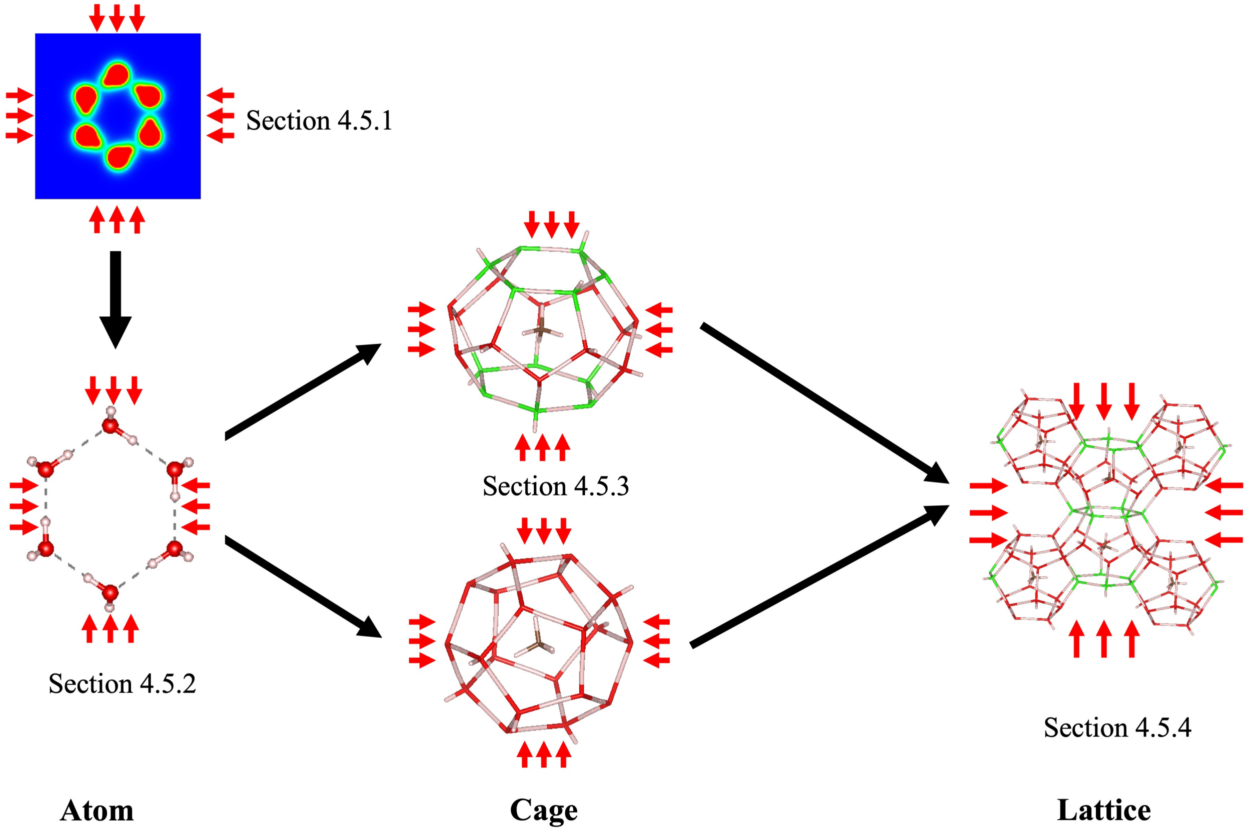

*Figure 4-1 Organization of this paper on piezo-sensitivity and ultimate mechanical stability pf methane GHs under compression and expansion pressure loads. Section 4.5.1 and 4.5.2 provide an atomistic characterization of electronic and bond geometry characterization as a function of pressure. This information feeds into the cage level in Section 4.5.3, where the small and large polyhedra are seen as a composite material system with its own rules of mixtures. Section 4.5.4 characterized the response and stability at the lattice level.*

# 4.4 Methodology

In this section we summarize the main aspects of the methodology, emphasizing the link of methods to applications. In particular, the mechanisms and principles used to illustrate the results will be presented. Section 4.4.1 compromises of two parts, which are used to generate the raw data from the density function theory (DFT). Section 4.4.1.1 introduces the structure of sI methane hydrate. Section 4.4.1.2 discusses the applications of density functional theory (DFT) with the software VASP. Section 4.4.2 is composed of three sections, which demonstrates the methodologies used to process the raw data and obtain the parameter values for analysis. Section 4.4.2.1 shows the calculations of bond angles and bond lengths. Section 4.4.2.2 presents the procedure to generate the electron cloud distribution. Section 4.4.2.3 demonstrate the methods and software used to calculate the cage volume.

## 4.4.1 Structures and simulations

### 4.4.1.1 Lattice Structure

As mentioned above, the unit lattice of sI methane hydrate has 46 water molecules form two small water cages and six large water cages in a cubic structure. The small water cage contains twelve pentagonal polygons ($5^{12}$) and the large water cage contains twelve pentagonal polygons and two hexagonal polygons ($5^{12}6^{2}$).[24] In sI hydrate, each cage can take up to one gas molecule. To determine the positions of water cages, Takeuchi, F. et al. [25] used the X-ray diffraction to determine the water oxygen atoms positions and propose the positions of water hydrogen atoms following the Bernal-Fowler ice rules,[26] where the adopted structures have the lowest net dipole moments. In this work, the guest molecules are place at the centre of the water cages to minimize the net dipole moments.

### 4.4.1.2 DFT simulations

The density functional theory method, which is based on Kohn-Sham equations, is used to simulate the sI methane hydrate system's behaviours under different pressures. All the simulations were performed at 0 K with periodic boundary conditions. The unit lattice of sI methane hydrate is prepared as described in Section 4.4.1.1. The Vienna Ab initio Simulation Package (VASP) was selected for the DFT simulations. Tensile and compressive pressures were applied to explore the piezo effects on the hydrate system. The revPBE exchange-correlation function with DFT-D2 dispersion correction methane was selected for this study based on our previous work[13,16,22,23]. Two types of exchange-correlation functions were utilized following our past paper[13]. The quasi-Newton algorithm was used within the stable pressure range, and the conjugate gradient algorithm was applied in the extreme pressure conditions. To keep the results consistent and comparable, the selection of the simulation parameters are the same as the previous work[13] and shown in Supplementary Information 1 (SI1).

## 4.4.2 Bonds and Electron Density Calculation

The details of (i) bond angles' and bond lengths' calculations, (ii) electron density, and (iii) cage volumes are given in Supplementary Information 2 (SI2). The extrema and mode of the computed hydrogen bond angles and hydrogen bond lengths distribution functions establish the basic geometric properties of the pentagons and hexagons in the small and large cages. The electron density function $\rho(x, y, z)$ gives measures of bonding and repulsive interactions that become important at determining stability thresholds close to critical dilation and compressive loads. The cage volume calculations yield direct measures used to determine the distinct polyhedral distortions under pressures and is also used to determine individual elastic cage moduli.

The electron density is usually shown in a selected plane as a 2D level set projection. In this paper, the selected planes for both small and large cages meet the following criteria: (i) the plane can cross the center or the midpoint of the methane molecule (guest molecule); (ii) the selected plane includes as many surrounding water molecules as possible (iii) the selected plane can clearly quantify the cage distortion or cage deformation. The selected planes are shown in Figure 4-2, and their corresponding defining parameters are shown in Table 4-1.

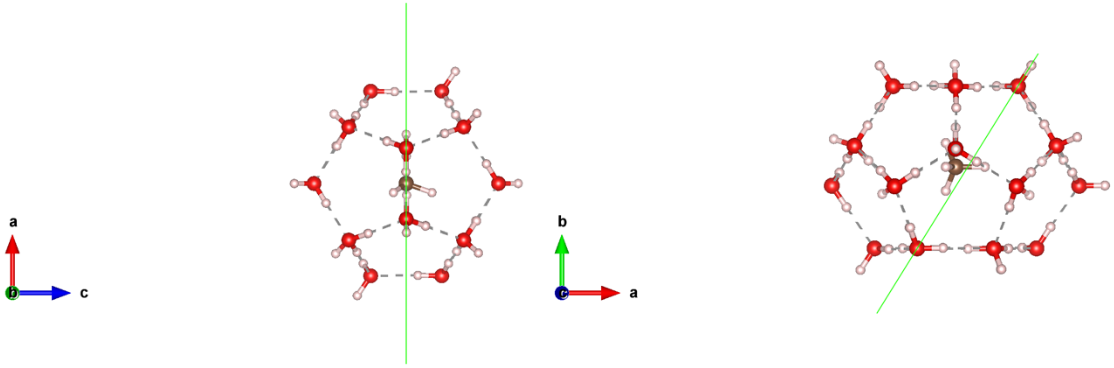

*Figure 4-2. Selected planes for small (left) and large (right) cages electron density visualization. The planes are indicated in green. (a,b,c) are the lattice unit vectors.*

*Table 4-1 Parameters of selected planes*

| | Small cage | Large cage |
|---|---|---|
| Miller indices (hkl) | $(0\quad 0\quad 1)$ | $(-1.6073\quad 1\quad 0)$ |
| Distance form origin | $0.5 \times d$ | $-0.917321 \times d$ |

Note: $d$ is the lattice constant.

Table 4-1 provide the information of the selected planes for the 2D display of electron density distribution. Figure 4-2 (left) shows the selected plane for the small cage. The plane in green, crosses the hydrogen bond (top and bottom) and center of methane molecule at the middle. Figure 4-2 (right) shows the selected plane for the large cages, which crosses the center of four oxygen atoms belonging to the hexagonal rings, and the center methane molecules.

# 4.5 Results and Discussion

## 4.5.1 Electron density distribution

In this section, the cross-sectional electron density r distributions of $5^{12}6^2$ (large) and $5^{12}$ (small) cages in the -1.1 GPa, 0 GPa and 7.5 GPa pressure interval are shown in the central panel of Figure 4-3, and the supporting information given by OH hydrogen bond length (left) and OOO bond angles (right) plots. The size and shape of each electron density r frame are normalized with a common reference to establish relative displacements and non-affine deformations under pressure loads, as follows. A density of 1 electron/Å$^3$ is selected as the threshold of electron density. This threshold is selected based on previous work. All quantitative details are shown in SI3.

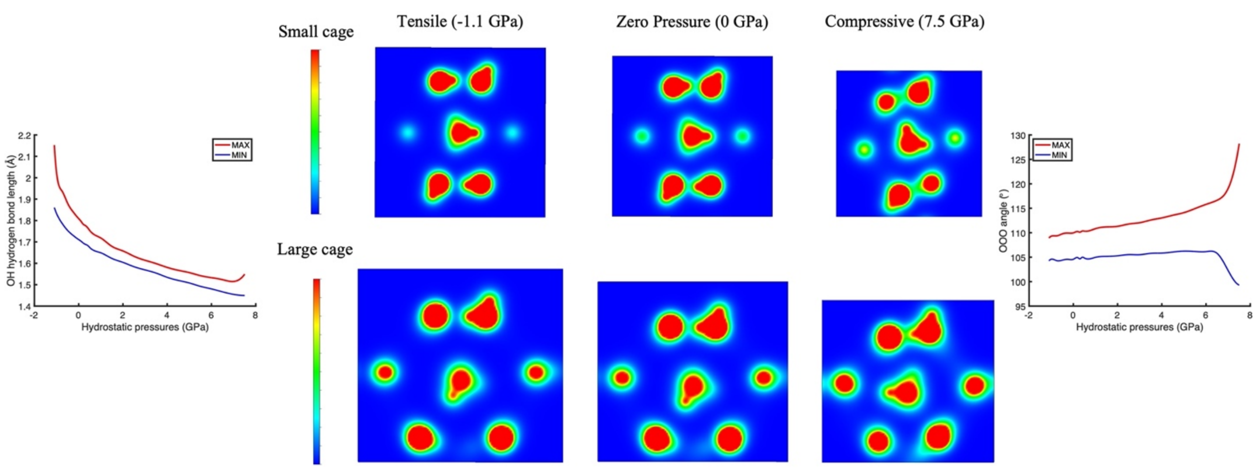

*Figure 4-3. Electron density distribution (middle 2x3 panel) of small (top) and large (bottom) cages at selected planes. The red color indicates the electron density is 1 electron/Å and more, and the blue color means 0 electron/Å3.OH hydrogen bond versus hydrostatic pressures (left figure). OOO angle versus. hydrostatic pressures (right). The red and blue curves correspond to the maximum and minimum value respectively.*

The small cage under zero pressure is selected as the reference. Normalization is based on

:

$$\frac{\text{side length of figure}}{\text{reference side length}} = \left(\frac{\text{cage volume}}{\text{reference cage volume}}\right)^{\frac{1}{3}}$$

Figure 4-3 shows electron density r plots for the two cages for increasing pressures from left to right. In all figures, the center region is methane. Applying pressure produces non-affine deformation that include compaction, rotation (specially in large cage), and out-of-plane displacements.

For the small cages, under 0 GPa, except the two electron clouds on the sides, all show typical pear-like noncircular shapes. This shape is attributed to the OH or CH covalent bonds. The top and bottom electron clouds have the tail towards the center of neighboring oxygen atoms. The electron clouds on the side have less electron density because the selected plane crosses the hydrogen bonds instead of an oxygen center. Under -1.1 GPa, the shape of the electron clouds does not change, only the distances between the electron clouds increase. However, under 7.5

GPa, the electron clouds lose their initial shapes. Firstly, the shape change of the methane molecules is a robust indication of molecular and atomic displacement. Secondly, the top and bottom electron clouds lose their initial pear shape and begins to merge with their neighbors. This means the tails formed by the OH covalent bonds are no longer visible. It is not possible to exactly determine if OH covalent bond is aligned with OH hydrogen bonds, which leads to a difference between HOH angle and OOO angle. However, it is worth mentioning that the degree of tilting of top and bottom electron clouds are similar and the integrity and symmetry of small cages are still maintained.

Similar phenomena are found for the large cages. Under 0 GPa, each electron cloud shows its own distinctive features. Under -1.1 GPa, all the features are maintained. Only the distance between the electron clouds become greater. However, under 7.5 GPa, the displacement of atoms and molecules occurs. The top two electron clouds are tilted, which implies the hexagonal face may distort due to the compression. The shape change of the central electron cloud further confirm the displacement of methane under compression. However, at this instance, the bottom electron clouds do not tilt, only the top electron clouds do. The symmetry properties of the large cages are broken.

Next, the focus is shifted to the stability limits. The greater distance between electron clouds corresponds to the longer OH hydrogen bond length shown in Figure 4-3 (left). The dramatic increase of OH hydrogen bond length under -1.1 GPa indicates that the tensile stability limit is approached. Also, the displacement of molecules under 7.5 GPa is consistent with the wide spread of OOO angle shown in Figure 4-3 (right). The sudden open spread OOO angle distribution implies the compressive pressure limit is approached. These calculations agree with the lattice-based results[13] that failure modes are ductile under expansion and brittle under compression. The ductile modes are associated with OH hydrogen bond length extensions and the brittle modes are associated with the divergence of the OOO angles.

In partial summary, calculating the electron density provides the following important information to characterize GH at the cage level and at the lattice level.

1. Tensile pressure has no impact on the atoms position, only has effect on the cage size (brittle mechanism)
2. Under compressive pressures (ductile mechanism)
    (i) The shape change of the central electron clouds indicates the methane molecule displacement
    (ii) The shape change of the top and bottom electron cloud (no pear shape, no tail) indicate the OH is not on the same line as the OO. Thus, the OOO angle is different from the HOH angle.

## 4.5.2 Bond Parameters

The bond length $[l]$ and bond angles$[\theta]$ are the two types of bond parameters that define the respective distribution functions. The bond lengths include the OH hydrogen bond length, OH covalent bond length, OO distance, while the bond angles include the OOO angle and HOH angle. The five distribution functions are shown in Supplementary Information (SI4).

The water framework of GHs is characterized by bond angle $[\theta]$ and bond length $[l]$ distribution functions whose mean, standard deviation and skewness provide the necessary metrics for bond-scale description of piezo effects and stability limits; the definition and nomenclature of these distribution functions are given in Table 4-2.

*Table 4-2 Distribution functions for bond geometry and bond types*

| | Bond length $[l]$ | | | Bond angle $[\theta]$ | |
|---|---|---|---|---|---|
| | OH covalent $[l^C]$ | OH hydrogen $[l^H]$ | OO distance $[l^O]$ | HOH $[\theta^H]$ | OOO $[\theta^O]$ |
| Mean $[m]$ | $m_l^C$ | $m_l^H$ | $m_l^O$ | $m_\theta^H$ | $m_\theta^O$ |
| Standard deviation $[\sigma]$ | $\sigma_l^C$ | $\sigma_l^H$ | $\sigma_l^O$ | $\sigma_\theta^H$ | $\sigma_\theta^O$ |
| Skewness$[\gamma]$ | $\gamma_l^C$ | $\gamma_l^H$ | $\gamma_l^O$ | $\gamma_\theta^H$ | $\gamma_\theta^O$ |

Figure 4-4 shows the mean $\mathrm{m}_\mathrm{j}^\mathrm{i}$, standard deviation $\sigma_\mathrm{j}^\mathrm{i}$ and skewness $\gamma_\mathrm{j}^\mathrm{i}$ for the five selected parameters, listed in Table 4-2. Here i refers to bond types (covalent, hydrogen bond) and j to geometry (length, angle), as follows.

*(a) Bond lengths.* The top row in Figure 4-4 on bond length $m_l^i$ statistics show the following: (i) the OH covalent bond is weakly perturbed by increasing pressure; (ii) the OH hydrogen bond and OO bond have similar responses, with the mean m decreasing with P and the standard deviation $\sigma$ decreasing with pressure until essentially plateauing, (iii) the skewness $\gamma$ of OH hydrogen bond and OO distance have characteristic oscillations with two local minima; the fluctuations of $\gamma_l^H$ and $\gamma_l^O$, compared with the consistent evolving of $m_l^H$ and $m_l^O$, indicates the non-uniform distribution among the bond lengths; (iv) when comparing OH covalent and OH hydrogen bond we not only see the well-known compensation mechanism[27] in the mean but also in the oscillatory skewness; (v) the stability limits are clearly reflected in $\sigma$ and $\gamma$. A significant increase of the $\sigma_l^H$ and $\sigma_l^O$ under -1.1 GPa, and an unexpected increase of the $\sigma_l^H$ and $\sigma_l^O$ under 7.5 GPa, indicate that the spreads of the bond length distribution become wider. The $\gamma_l^H$ and $\gamma_l^O$

provides further evidence on the stability limits. The significant increase (almost vertical lines) on the two ends, implying the distribution deviates from the Gaussian very abruptly.

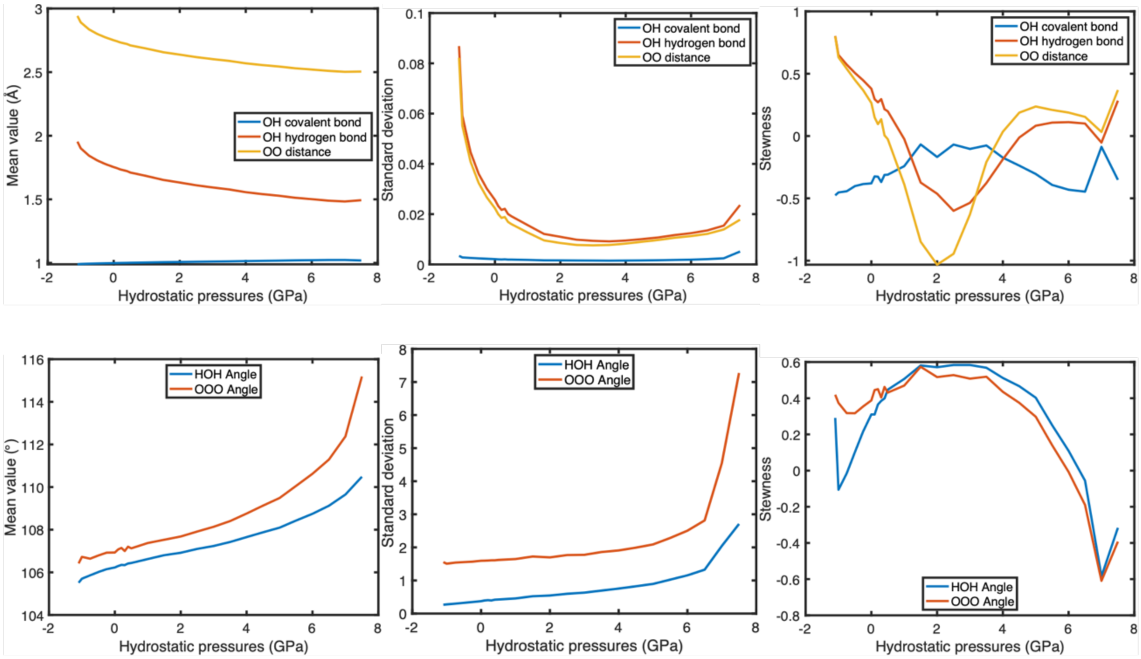

*Figure 4-4 Mean, standard deviation and skewness of five bond parameters, defined in the insets and in Table 4-1. The top three are bond lengths and the bottom three are bond angles.*

*(b) Bond Angles.* The bottom row in Figure 4-4 on bond angles $m_\theta^i$ statistics show the following: (i) $m_\theta^H$ and $m_\theta^O$ show an increasing trend with pressure. A significant increase of $m_\theta^O$ occurs at 7.5 GPa; however, the $m_\theta^H$ still follows it's initial tendency. This implies that the intermolecular interactions are modified instead of the intramolecular interactions. The water molecules are displaced from their original positions, which is a robust indication on the deformation; (ii) $\sigma_\theta^H$ and $\sigma_\theta^O$ has a large increase at 7.5 GPa, meaning that the spread of angles becomes wider; (iii) $\gamma_\theta^H$ and $\gamma_\theta^O$ profiles are concave-down with sharp reversal at the two terminal sides, which is a signal of reaching the stability limits.

In partial summary, the $\sigma_{l,\theta}^{O,H}$ and $\gamma_{l,\theta}^{O,H}$ provide accurate quantitative metrics on the compressive stability limit. For the tensile stability limit, only the $\sigma_l^{O,H}$ and $\gamma_l^{O,H}$ gives significant information, but angle statistics do not. The phenomenon corresponds to the findings in Section 3.1, where it is found that under tensile pressures the system adjusts by size change and under compressive pressures, the system adjusts by shape deformation.

### 4.5.3 Cage deformation

Cage deformation takes places when the hydrate system must adapt to pressurized conditions. This deformation can be described as a non-affine deformation, such that the structure does not shrink or expand proportionally.[28] In the ideal case, if all the atoms and molecules can translate in their initial bonding directions due to the shrinking or expanding of the bond length proportionally, then a homogenous deformation takes place. However, in reality, non-affine or inhomogeneous deformations usually take place under pressure. In section 4.5.1 and 4.5.2, the results from the atomistic level indicate that the cages undergo non-affine deformations.

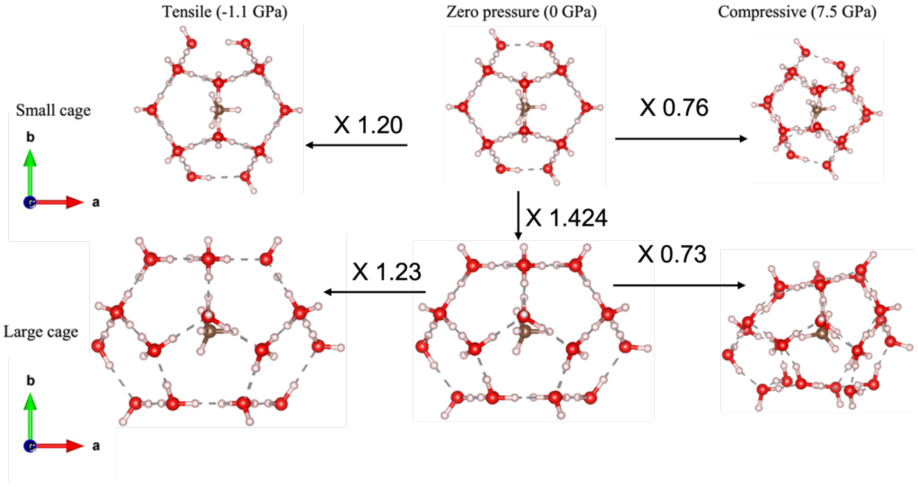

*Figure 4-5 Small and large cage structures under three pressures. The red circles are oxygen atoms. The white circles are hydrogen atoms, and the brown circles are carbon atoms. The grey dashed lines represent the OH hydrogen bonds with a maximum threshold 2.1 Å.*

Figure 4-5, shows the cage structures under three different pressures (-1.1 GPa, 0 GPa and 7.5 GPa). It demonstrates that the cages' structure do not change significantly under tensile pressures (-1.1 GPa), but under 7.5 GPa, both small and large cages display large non-affine deformations that need to be resolved.

The cage deformations can be characterized from three interconnected aspects: (i) volume, (ii) shape and (iii) polygonal face orientation as follows:

The large cage is approximately 42.4% larger than the small cages under zero pressure. Under 7.5 GPa, the large cages expand 23%; however, the small cages only expand 20%. Similarly, under -1.1 GPa, the large cages shrink 27%, but the small cages only shrink 24%. This phenomenon shows that either under tensile or compressive pressures, the large cage volume is more sensitive and changes more significantly.

Figure 4-5 shows that the entire small cage has deformed under a 7.5 GPa load, but in the large cage, only the top hexagonal ring tilted, while pentagons retain their initial shape. On average, at 7.5 GPa, the pentagonal rings in small cages tilt approximately 19.29°. However, hexagonal rings that react most significantly in large cages, only tilt 13.81°. This difference can be explained by the larger area of hexagonal rings which can lead to better load distribution under pressurized conditions.

In partial summary, the cage level analysis reveals the following points when compared to electron cloud-bond analysis:

1. Under both compressive and tensile pressures, the large cages are more sensitive on the size change, compared with the small cages.

2. When approaching the compressive stability limit, both small and large cages have non-affine deformation. The small cages still maintain their integrity and symmetry; however, the large cages do not.

The information transfer to the next higher level is that small and large cages have different levels of resistance under compressive pressures and may have an impact on the lattice elasticity.

## 4.5.4 Bulk modulus

Bulk modulus K is used to evaluate a material's resistance to compressive forces. Either polycrystal or monocrystal, the value of the bulk modulus K is usually used to characterize the entire lattice. Since we have demonstrated above (Section 3.3) the distinct nature of large and small cages, and as the large cages form a continuous phase while the small cages form a disperse cage, an opportunity arises to model the system as a binary composite system. The novel approach is to compute the bulk modulus K of the system and compare it with the bulk modulus using material property mixing rules. This approach sheds light on the different contributions to material properties by the large and small cages. Since as shown in Section 3.3 above large and small cages respond differently to pressure, we can assign main drivers for sensitivity to either cage.

There are several ways to calculate the bulk modulus. The most common ways are the thermodynamic approach, EOS fitting and the Voigt-Reuss-Hill (VRH) approximation. In this section, the thermodynamic approach is used, and it is defined as Equation (4.1).

$$K^{i} = -V_0^{i}\frac{dP}{dV^{i}}; i = l, s \tag{4.1}$$

where the $K^i$ is the "i" cage bulk modulus, P is the pressure, $V_0^i$ is the initial volume of the "i" cage, and the superscripts $l$ and $s$ stand for large and small cages. Equation (4.1) is valid under a constant temperature. In this work, the temperature is 0 K. The volume of the cages and lattices can be evaluated from the methods discussed in Section 2 and the applied pressures can be controlled by the simulation settings. A third-order polynomial fitting is applied to obtain the relationship between the pressures and the volume P(V). The selection of the polynomial order keeps consistency with the EOS fitting in our previous work[13] used for comparison. The averaged values of $K^l$ and $K^s$ are showed in Figure 4-6.

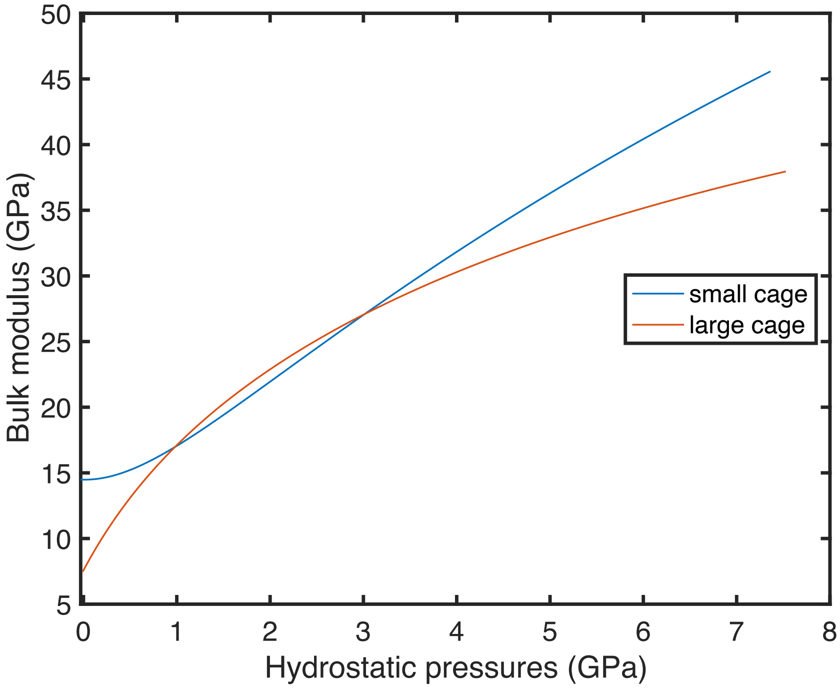

*Figure 4-6 Averaged bulk modulus for small and large cages from 0 GPa to 7.5 GPa. The blue curve represents the averaged $K^s$ and red curve is the averaged $K^l$*

Figure 4-6 shows the averaged values of $K^l$ and $K^s$ from 0 GPa to 7.5 GPa. Although both $K^l$ and $K^s$ increase with pressure, their sensitivity is different. In the low pressure region (from 0 GPa to 1 GPa), $K^l$ increases dramatically but $K^s$ remains essentially constant. Between 1 GPa and 3 GPa, the large and small cages share similar bulk modulus values. Beyond 3 GPa, $K^s$ exceeds and increases faster than the $K^l$. Figure 4-6, clearly shows that small and large cages have different sensitivities, and thus they have different impacts on the lattice piezo-elastic performance. This observation coupled with the geometric fact that small cages are isolated while large cages form the continuous phase points to a possible new approach to characterize GH at the meso-scale.

Thus, assuming the small and large cages form a composite continuum, the rule of mixture can be applied for estimation or prediction of the lattice performance on various properties based on the behaviours of the individual cages. Using standard homogenization methods, the upper and lower bound of the bulk modulus in the terms of the cage moduli are:

$$K_{upper} = f^s K^s + (1 - f^s) \times K^l \tag{4.2}$$

$$K_{lower} = \left(\frac{f^s}{K^s} + \frac{1 - f^s}{K^l}\right)^{-1} \tag{4.3}$$

$$K = -V_0 \frac{dP}{dV} \tag{4.4}$$

Here $K$ is the bulk modulus of the unit lattice, $f^s$ is the volume fraction of the small cages and $(1 - f^s)$ is the volume fraction of the large cages.

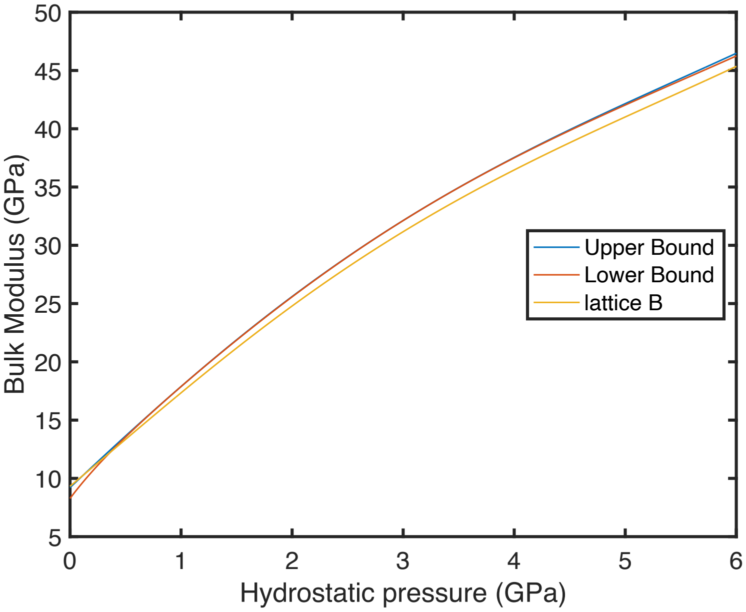

*Figure 4-7 Bulk modulus of unit lattice. The blue curve is the upper bound calculated by using Equation (4.2). The orange curve is the lower bound of bulk modulus calculated by using Equation (4.3). The yellow curve the bulk modulus of the unit lattice calculated using Equation (4.4).*

Figure 4-7 shows the upper $K_{upper}$ (blue), lower $K_{lower}$ (orange) bounds, and the bulk (yellow) modulus K, calculated using equations (4.2-4.4). The figure illustrates that that the three curves essentially overlap. The value of the bulk modulus (shown in yellow) is very close to the bulk modulus obtained by EOS fitting[13] and shows a similar evolving tendency under pressures. In comparison to experimental results, Hirai, H., et al.[29] reported the bulk modulus is 7.4 GPa for sI methane hydrate, and Loveday, J. S., et al.[30] showed the bulk modulus is 15.4 GPa for MH-II (methane hydrate II) by using diffraction methodologies. The bulk modulus generated by our work under 0 GPa and 0 K is 9.5785 GPa, which is very close to the experimental results. The small discrepancy can be explained by the temperature difference. This validates the reproducibility of bulk modulus of the monocrystal hydrates from different approaches.

Overall, from the results shown in Figure 4-7, it can be verified that from 0 GPa to 7.5 GPa, the sI methane hydrate follows the rule of mixtures with high accuracy, and the view of GH as a binary inclusion-continuous phase composites is a novel applicable concept. The upper and lower bounds can give an accurate and reliable prediction on elastic properties.

## 4.6 Conclusion

This paper characterized the pressure response and stability limits of sI methane hydrates from atomistic, cage and lattice scales. The pressure stability limits are found to be -1.1 GPa and 7.5 GPa under 0 Kelvin. Insights, mechanisms, and information transfer from atomistic scales to macroscopic scales are established by using bond energy/geometry, cage mechanics and geometry, and macroscopic lattice elasticity. This theory and computational multiscale approach reveals important information and understanding not obtainable by just computing macroscopic mechanical properties. A condensed summary of the results and interconnections are given in Figure 8.

Starting at the smallest scales (section 4.5.1), from the electron cloud displacement, merging or connections, we can predict the displacement of the atoms and the molecules, which imply the changes of bond length and bond angles used in the next scale (section 4.5.2). The established distribution functions of bond angles and lengths show significant phenomenon when the pressure stability limits being approached (section 4.5.2). Also, the distribution function of bond length and bond angles establishes that the bond parameters are not a constant but change within ranges whose upper and lower limits follow different pressure scaling. The information is used to characterize the cage level (section 4.5.3). Since the small dodecahedron $5^{12}$ cage is a platonic solid with high degree of symmetry and is vertex-uniform, edge-uniform, and face-uniform, it will behave very different under pressure than the large non-regular tetrakaidecahedra $5^{12}6^{2}$ cages. From a geometric view we expect and find the small cage will mostly retain their symmetry properties while the large cages are prone to large distortions even under an isotropic pressure stress load. Accordingly, we found (section 4.5.3) that affine and non-affine deformation under tensile and compressive pressures can be observed at the cage level. The cage level bulk elasticity confirms that only under weak-to-intermediate pressure loads, the two cages have similar stiffness, but the response deviates sharply as the stability limits are approached. Since the large cages form the matrix phase and the small cages are isolated inclusions, this fact opens up the possibility to consider (section 4.5.4) the GH as a composite material system at the mesoscopic cage level that can be subjected to homogenization material composite scaling (laws of mixtures). We find excellent agreement between the calculated independently lattice bulk modulus and the laws of mixtures predictions based on a composite material model. Under compression we find that the bulk modulus varies approximately between 10 GPa and 45 GPa as the pressure increases from 0 GPa to 6 GPa and that the sensitivity or rate of increase weakens at higher pressure. This can be explained by the fact that there are three large cages per small cage and that large cage sensitivity decreases at higher loads, a fact not captured by macroscale computations.

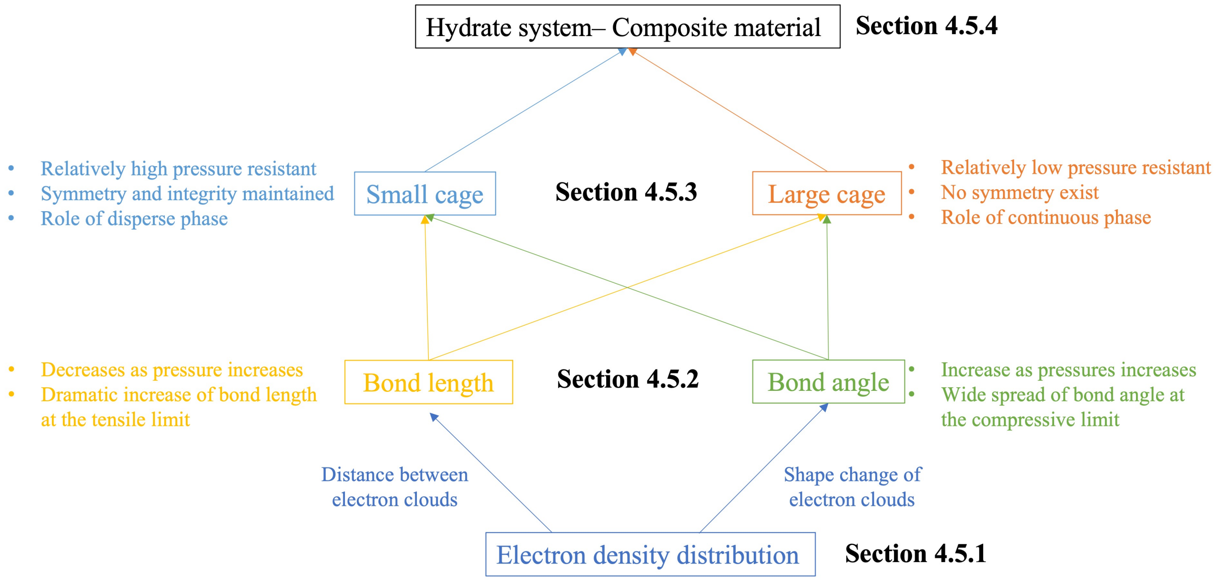

*Figure 4-8 Key findings and multi-scale connections. The key findings are listed on the side in the corresponding color. The arrow indicates the connections between different scales. The text in blue associated with electron density distribution. The two blue arrows show how the electro density distribution have an impact on the bond parameters ( Section 4.5.1).The text in yellow and green are relevant to bond length and bong angle respectively (Section 4.5.2). The blue and orange text represents the small and large cages respectively (Section 4.5.3) The black text shows the information from the lattice view (Section 4.5.4).*

We conclude with specific implications of the results. The pressure stability limits determination of sI methane hydrate under 0 Kelvin provide the upper bound values on the pressure limits, which can be of critical importance during exploration. Also, the mechanical parameter values obtained at 0 K are upper bound values and as such they provide critical information even at lower temperatures. The established connections between different levels are essential to understand the origin of macroscopic properties originating from atomistic and cage level. Firstly, the electron cloud displacement under pressure explain explicitly the bond length and angle changes. This provides a measure of the molecular displacement under pressures instead of simply observations of size or shape changes. Secondly, computing the distribution functions for bond length and angles establishes the variability of these quantities, in contrast to adopting a single value view. Meanwhile, this distribution function emphasizes the importance of maximum and minimum values within the spread, instead of the mean and median, since the maximum and minimum values can be the threshold of instability, where cracks can be triggered. Thirdly, the captured difference between small and large cages indicates that different types of cages can have different features, and the difference can be contributed to the cage shape, occupancy, guest type, etc. Fourthly, the determined roles of small and large cages shows that each type of cages can have its own impact on the lattice. This indicates that the occupancy or the guest type can be determined if we have the information of lattice and the occupied or unoccupied cages with different types of molecules. This can simplify the process for identifying the guest type and increase the success rate of exploration as well as material characterization.

Taken together the multiscale methodology established and used here for methane SI hydrates , based on the integration of atomistic hydrogen bonding, cage geometry and composite-like inclusion/matrix structure, and macroscopic elasticity can be an additional tool to further develop the material physics and technology of other gas hydrates.

# 4.7 Reference

1 Englezos, P. Clathrate hydrates. **32**, 1251-1274, doi:10.1021/ie00019a001 (1993).

2 Ruppel, C. D. Methane Hydrates and Contemporary Climate Change. *Nature Education Knowledge 3(10):29* (2011).

3 Sloan Jr., E., Koh, C., Koh, C. . Clathrate Hydrates of Natural Gases., 752 pages (2007).

4 Dillon, W. P. in *Encyclopedia of Physical Science and Technology (Third Edition)* (ed Robert A. Meyers) 473-486 (Academic Press, 2002).

5 National Research, C. *et al. Charting the Future of Methane Hydrate Research in the United States*. (National Academies Press, 2004).

6 Council of Canadian Academies. Expert Panel on Gas, H. (Council of Canadian Academies = Conseil des académies canadiennes, Ottawa, 2008).

7 Connection, C. C. *CO2 EQUIVALENTS*, <https://climatechangeconnection.org/emissions/co2-equivalents/> (2021).

8 Yu, Y.-S., Zhang, X., Liu, J.-W., Lee, Y. & Li, X.-S. Natural gas hydrate resources and hydrate technologies: a review and analysis of the associated energy and global warming challenges. *Energy & Environmental Science* **14**, 5611-5668, doi:10.1039/d1ee02093e (2021).

9 Lyakhov, G. A. & Mazo, D. M. Realization of 3D random Voronoi mosaic cell in hydrate phases of clathrate compositions. *Physics of Wave Phenomena* **17**, 289-300, doi:10.3103/s1541308x09040062 (2009).

10 Shevelkov, A. & Kovnir, K. Vol. 139 97-142 (2011).

11 Mathews, S. L., Servio, P. D. & Rey, A. D. Heat Capacity, Thermal Expansion Coefficient, and Grüneisen Parameter of CH4, CO2, and C2H6 Hydrates and Ice Ih via Density Functional Theory and Phonon Calculations. *Crystal Growth & Design* **20**, 5947-5955, doi:10.1021/acs.cgd.0c00630 (2020).

12 Jendi, Z. M., Servio, P. & Rey, A. D. Ideal Strength of Methane Hydrate and Ice Ih from First-Principles. *Crystal Growth & Design* **15**, 5301-5309, doi:10.1021/acs.cgd.5b00829 (2015).

13 Zhu, X., Rey, A. D. & Servio, P. Piezo-elasticity and stability limits of monocrystal methane gas hydrates: Atomistic-continuum characterization. *The Canadian Journal of Chemical Engineering* **101**, 639-650, doi:https://doi.org/10.1002/cjce.24433 (2023).

14 Vlasic, T. M., Servio, P. D. & Rey, A. D. Effect of Guest Size on the Mechanical Properties and Molecular Structure of Gas Hydrates from First-Principles. *Crystal Growth & Design* **17**, 6407-6416, doi:10.1021/acs.cgd.7b01072 (2017).

15 Daghash, S. M., Servio, P. & Rey, A. D. Elastic properties and anisotropic behavior of structure-H (sH) gas hydrate from first principles. *Chemical Engineering Science* **227**, 115948, doi:https://doi.org/10.1016/j.ces.2020.115948 (2020).

16 Daghash, S. M., Servio, P. & Rey, A. D. First-Principles Elastic and Anisotropic Characteristics of Structure-H Gas Hydrate under Pressure. *Crystals* **11**, 477 (2021).

17 Daghash, S. M., Servio, P. & Rey, A. D. Structural properties of sH hydrate: a DFT study of anisotropy and equation of state. *Molecular Simulation* **45**, 1524-1537, doi:10.1080/08927022.2019.1660326 (2019).

18 Mirzaeifard, S., Servio, P. & Rey, A. D. Multiscale Modeling and Simulation of Water and Methane Hydrate Crystal Interface. *Crystal Growth & Design* **19**, 5142-5151, doi:10.1021/acs.cgd.9b00578 (2019).

19 Mirzaeifard, S., Servio, P. & Rey, A. D. Molecular Dynamics Characterization of Temperature and Pressure Effects on the Water-Methane Interface. *Colloid and Interface Science Communications* **24**, 75-81, doi:https://doi.org/10.1016/j.colcom.2018.04.004 (2018).

20 Xu, K. *et al.* Structural and mechanical stability of clathrate hydrates encapsulating monoatomic guest species. *Journal of Molecular Liquids* **347**, 118391, doi:https://doi.org/10.1016/j.molliq.2021.118391 (2022).

21 Chazallon, B. *et al.* Characterizing the variability of natural gas hydrate composition from a selected site of the Western Black Sea, off Romania. *Marine and Petroleum Geology* **124**, 104785, doi:https://doi.org/10.1016/j.marpetgeo.2020.104785 (2021).

22 Jendi, Z. M., Rey, A. D. & Servio, P. Ab initio DFT study of structural and mechanical properties of methane and carbon dioxide hydrates. **41**, 572-579, doi:10.1080/08927022.2014.899698 (2015).

23 Vlasic, T. M., Servio, P. & Rey, A. D. Atomistic modeling of structure II gas hydrate mechanics: Compressibility and equations of state. *AIP Advances* **6**, 085317, doi:10.1063/1.4961728 (2016).

24 Sloan, E. D. Fundamental principles and applications of natural gas hydrates. *Nature* **426**, 353-359, doi:10.1038/nature02135 (2003).

25 Takeuchi, F. *et al.* Water proton configurations in structures I, II, and H clathrate hydrate unit cells. *The Journal of Chemical Physics* **138**, 124504, doi:10.1063/1.4795499 (2013).

26 Bernal, J. D. & Fowler, R. H. A Theory of Water and Ionic Solution, with Particular Reference to Hydrogen and Hydroxyl Ions. *The Journal of Chemical Physics* **1**, 515-548, doi:10.1063/1.1749327 (1933).

27 Pruzan, P. Pressure effects on the hydrogen bond in ice up to 80 GPa. *Journal of Molecular Structure* **322**, 279-286, doi:https://doi.org/10.1016/0022-2860(94)87045-4 (1994).

28 Gründemann, H. Ogden, R. W., Non-Linear Elastic Deformations. Ellis Horwood Ltd. 1984. Chichester, Distributors: John Wiley & Sons Ltd., XV, 532 S., £ 35.00. ISBN 0-85 312-273-3. *ZAMM - Journal of Applied Mathematics and Mechanics / Zeitschrift für Angewandte Mathematik und Mechanik* **65**, 404-404, doi:https://doi.org/10.1002/zamm.19850650903 (1985).

29 Hirai, H. *et al.* High-pressure structures of methane hydrate observed up to 8 GPa at room temperature. *The Journal of Chemical Physics* **115**, 7066-7070, doi:10.1063/1.1403690 (2001).

30 Loveday, J. S. *et al.* Stable methane hydrate above 2 GPa and the source of Titan's atmospheric methane. *Nature* **410**, 661-663, doi:10.1038/35070513 (2001).

31 Ritchie, J. P. & Bachrach, S. M. Some methods and applications of electron density distribution analysis. *Journal of Computational Chemistry* **8**, 499-509, doi:10.1002/jcc.540080430 (1987).

32 Castillo, N., Robertson, K. N., Choi, S. C., Boyd, R. J. & Knop, O. Bond length and the electron density at the bond critical point: X□X, Z□Z, and C□Z bonds (X = Li-F, Z = Na-Cl). *Journal of Computational Chemistry* **29**, 367-379, doi:https://doi.org/10.1002/jcc.20795 (2008).

33 Waasmaier, D. & Kirfel, A. New analytical scattering-factor functions for free atoms and ions. *Acta Crystallographica Section A* **51**, 416-431, doi:10.1107/S0108767394013292 (1995).

34 Koichi MOMMA, F. I. *VESTA: a Three-Dimensional Visualization System for Electronic and Structural Analysis*. (2019).

35 Britannica, T. E. o. E. hydrogen bonding. *Encyclopedia Britannica* (2019).

36 Bader, R. F. W. *An introduction to the electronic structure of atoms and molecules*. 240 pages illustrations 24 cm (Clarke, Irwin, 1970).

# 4.8 Supplementary Information (SI)

## 4.8.1 Simulations (SI1)

This supplementary information SI1 provides a detailed description of the DFT simulation settings related to Section 4.4.1 of the paper.

*Table 4-3 Simulation parameters in DFT*

| | |
|---|---|
| Cut-off energy | 520 eV |
| Global break conditions the electronic self-consistent loop | $1\times10^{-4}$ eV |
| Break conditions for the ionic relaxation | $5\times10^{-3}$ eV/Å |
| Number of k-points | 4 |
| Grid generation mode | Gamma centered |

## 4.8.2 Bonds and Electron density calculations (SI2)

The supplementary information SI2 provides the detailed background information on the bond and electron density calculations discussed in Section 4.4.2 of the paper.

### 4.8.2.1 Bond angle and bond length distributions

In this paper, the distributions of five bond parameters are evaluated to characterize the water molecules' geometry, and intermolecular and intramolecular interactions under pressure: (i) three bond lengths (OH covalent bond length, OH hydrogen bond length, and OO distance) and (ii) two bond angles (OOO angle and HOH water bond angle).

The software MATLAB was used for the calculations of bond lengths and bond angles. The calculations are based on the atoms' positions, which can be obtained from the CONTCAR file of the VASP software. The relevant distances and angles are resolved using standard vector operations. Each vector has three components (position difference between two atoms) in the selected frame, as shown in Figure 4-9.

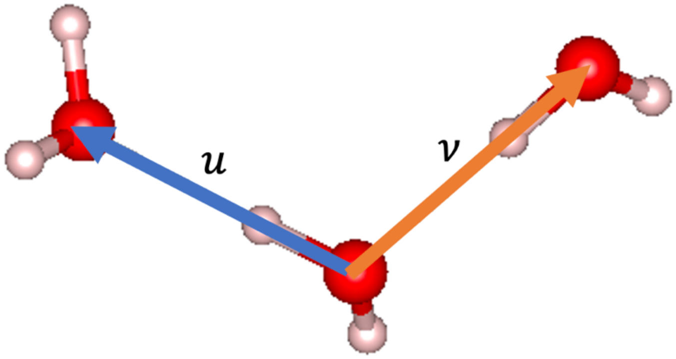

*Figure 4-9 Vectors between atoms. The red circle are water oxygen atoms, and the white circles are the water hydrogen atoms. The vector u is from the central oxygen atom to the left oxygen atom. The vector v is from the central oxygen atom to the right oxygen atom*

The bond lengths can be calculated using Equation (4.S1). The bond angles were calculated by using Equation (4.S2). Note: u and v are bond vectors from the central water oxygen atom to its neighboring oxygen or hydrogen atoms and θ is the corresponding bond angle between two vectors. The three generic components of vector are indicated as a, b and c respectively.

Bond length:

$$u = \begin{bmatrix} a \\ b \\ c \end{bmatrix}$$

$$|u| = \sqrt{a^2 + b^2 + c^2} \tag{4.S1}$$

Bond angle:

$$\theta = acos\left(\frac{u \cdot v}{|u||v|}\right) \tag{4.S2}$$

### 4.8.2.2 Electron cloud distribution

Electron density distribution is the most fundamental and basic parameter to illustrate the system's behaviours. This is because the atoms are formed by electrons and neutrons, and the electrons are much lighter than the neutrons. Once the conditions change, the electrons are more likely to react or react more dramatically than the neutrons, which can provide information on the reaction tendency of the material system.

In this section, the software and methodologies used to generate the electron density will be discussed since electron cloud distribution or distortion would provide atomic level understanding under pressures. The electron cloud, which is also called the electron density distribution, shows the probability of the existence of electrons around the atoms. This information can be used to predict the interactions between atoms,[31] and critical bond length.[32]

To evaluate the electron density, we used the Visualization for Electronic and Structural Analysis (VESTA) software. The CONTCAR file generated from the DFT simulation provides the atomic positions. The electron densities are then calculated from the Fourier transform of structure factors, $F(\boldsymbol{h})$, that in turn are calculated from structural parameters and the atomic scattering factors of free atoms[33] with Equation (4.S3).

In X-ray diffraction, $F(\boldsymbol{h})$ represents that structure factor $F$ of reflection $\boldsymbol{h}$ with diffraction indices $hkl$. In Equation (S3), where $j$ is the atom number, n is the total atom number in the unit lattice, $g_j$ is the occupancy, $f_j(\boldsymbol{h})$ is the atomic for factor, $T_j(\boldsymbol{h})$ is the Debye-Waller factor, and $x_j,\ y_j,\ and\ z_j$ are the fractional coordinates.[34]

$$F(\boldsymbol{h}) = \sum_{j=1}^{n} g_j f_j(\boldsymbol{h}) T_j(\boldsymbol{h}) exp\left[2\pi i\left(hx_j + ky_j + lz_j\right)\right] \tag{4.S3}$$

The spatial resolution of electron densities is specified in the unit of Å. Although smaller resolution could give more accurate results, the computational and time costs are significant. Comparing the results obtained from scale resolutions of 0.05 Å and 0.1 Å, the discrepancy is found to be negligible. The spatial resolution of electron densities is then selected as 0.1 Å. The electron density, $\rho(x, y, z)$ at the coordinates of $(x, y, z)$ is calculated by Equation (4.S4). $N_i$ is the number of grids along each crystallographic “i” axis, which is automatically set. $N_x$ gives a resolution close to the specified value and it satisfies symmetrical constraints.[34]

$$\rho(x, y, z) = \frac{1}{V} \sum_{h=\frac{-N_x}{2}}^{\frac{N_x}{2}} \sum_{k=\frac{-N_y}{2}}^{\frac{N_y}{2}} \sum_{l=\frac{-N_z}{2}}^{\frac{N_z}{2}} F(\boldsymbol{h}) exp[2\pi i(hx + ky + lz)] \tag{4.S4}$$

After computing the electron density for the entire lattice, 2D data display was used to visualize the electron density distribution on a specified plane. The selected plane in this paper aims to capture the guest-host interactions and water molecules displacements. To further discover the cage features, two planes were chosen for the small and large cages respectively. Each plane crosses the centre of the guest molecule and passes the closest water oxygen atoms.

### 4.8.2.3 Cage Volume Calculations

Considering that two types of cages are involved in sI methane hydrates, the intrinsic features of each type of cages are possible to have its own impacts on the performance of the entire lattice. The cage volume is a representative and fundamental parameter to provide the indications of cage performance under pressures. To estimate the cage volume, the MATLAB software and the convex hull algorithm are applied. Once the atomic coordinates are available, the convex hull algorithm can be used to generate the smallest surface that contains all the atoms provided. Then, the volume can be approximated through the enclosed surface. Since convex hull is an approximation way, a subtle discrepancy (around 5%) exists within the pressure range from -1.1 GPa to 7.5 GPa, which is acceptable.

## 4.8.3 Electron cloud density (SI3)

This supplementary information SI3 discussed the details of electron density distribution discussed in Section 4.5.1 of the paper.

### Interpretation of electron density distribution

To explain the general electron distribution of the water molecules, it is necessary to characterize the bond types between the oxygen and hydrogen atoms. Within a water molecule, an oxygen atom is covalently bonded to two hydrogen atoms.[35] Their electrons are shared unequally due to oxygen's high affinity of electrons. Thus, the hydrogen atoms have a slight positive charge and the electrons are closer to the oxygen atom.[35] Beyond the covalent bonds, hydrogen bonds can be created by the oxygen and hydrogen atoms from different water molecules. Oxygen atom still has two pairs of unshared electrons after forming two covalent bonds with hydrogen atoms,, which gives it a slight negative charge. Through the electrostatic attraction, the oxygen atoms (electron donors) are inclined to share the electrons with the hydrogen atoms (electron acceptors), forming a hydrogen bond.[35] According to these, the electrons gather at the central oxygen atom, and electron distribution has two tails in the direction of hydrogen atoms.

**(i) Small cage:** The selected plane for small cage include four water molecules at the top and bottom. On the two sides, this plane can capture the electron density of the middle of two OH hydrogen bonds. Since the electrons are closer to the oxygen atoms, the electron density is lower at the middle of OH hydrogen bonds than the center of oxygen atoms. Thus under tensile and zero pressure, the top and bottom electron clouds have higher densities than the side clouds.

The four top and bottom water molecules, the density has pear-shape electron clouds under -1.1 GPa. Under zero pressure, the high electron density region, (where is greater than 1 electron/Å$^3$) of the top electron clouds, shown in red, keep the pear-shape; however, in the low electron density regions (less than 1 electron/Å$^3$), shown in green, start to connect with each other. When a 7.5 GPa compressive pressure is applied, the electron clouds become closer to each other, but the pear-shape is still kept for the high electron density region. Additionally, from zero to -1.1 GPa, the midpoints of the electron clouds are on the same horizontal line, which indicates the water molecules are found on the same original plane. However, when pressure increases to 7.5 GPa, a significant tilt can be detected. Their midpoints are not on the same horizontal line. This phenomenon indicates the displacement of water molecules.

Under tensile or zero pressures, the two electron clouds on the sides reflect the electron density distribution of the middle of OH hydrogen bonds. Since the hydrogen atom is an electron acceptor, the oxygen atom is an electron donor. The electron density at the middle of OH hydrogen bond is much lower than the center of oxygen atom. However, when 7.5 GPa is applied, the electron clouds on the sides become stronger, indicated as the yellow circles at the centre. This phenomenon shows that the oxygen atoms move towards the initial place of midpoint of OH hydrogen bonds. This can be illustrated as the displacement of molecules and perhaps cage begins to deform, and thus the plane could become closer to the oxygen atoms instead of the midpoint of hydrogen bonds. These two side clouds near the methane molecule instead of the initial OH hydrogen bonds, exert some effects on the shape and intensity of the methane electron cloud. The electron cloud of methane molecule could not maintain the pear shape. It changes to a big circle with two small tails. This shows the methane molecule starts to rotate to minimize the dipole interactions with its surrounding water molecules.

Additionally, the size of the selected plane and the shape forming by the six surrounding electron clouds can reflect the size change of the cage and the deformation. For the small cages, the size of the selected plane changes a lot. Compared with behaviours under zero pressure, it would expand approximately 6.3% on the side under -1.1 GPa and shrink around 8.7% on the side under 7.5 GPa. From these numerical values, it infers that the volume size of small cages are more sensitive to the tensile conditions than the compressive conditions. However, the small cage under compressive conditions is more likely to displace the molecules. The shape formed by the six surrounding electron clouds changes from a regular hexagon to an irregular hexagon. But the shape is maintained under tensile pressures.

### Large cage

The selected plane for large cage can compromise the water molecules in both hexagonal rings (top and bottom) and two water molecules in the pentagonal rings (on the two sides). This plane can provide plenty of information on the atoms' and cages' behaviours.

Under zero pressure, each electron cloud has its own shape. The central methane molecule still has the pear shape, as in the small cages. Once the tensile pressure is applied, each electron cloud becomes independent and they do not have a direct interaction with each other. The water molecules on the same horizontal line have similar electron densities.

However, when the pressure reaches 7.5GPa, there are significant changes on the large cages. Firstly, the tail direction of the electron cloud of methane molecule changes. Instead of the towarding left bottom, the central methane molecules towards to the left. Meanwhile, two top electron clouds show a tilting tendency. Two bottom water molecules have a similar electron clouds, but their electron clouds become relatively diverse under 7.5 GPa, which is shown as the larger green circle part. The changes on the electron cloud density are good indicators of the distance between the molecules and the selected plane. For the two water molecules on the sides, belonging to the pentagonal rings, they shows a stronger electron density under high compressive pressures, which implies the displacement of the oxygen atoms.

To compare the shape of electron cloud of large cages under -1.1 GPa, 0 GPa and 7.5 GPa, the performance under 0 GPa is selected as a reference. Under -1.1 GPa, the shape of electron clouds did not change, only the distance between electron clouds becomes greater. Even the shape formed by the surrounding six electron electrons did not change. However, under 7.5 GPa, the molecular displacement took place. The top two electron clouds showed a tilting tendency. The central methane molecule also showed a displacement tendency.

To conclude the behaviours of electron clouds in small and large cages, the volume of both cages are more sensitive to the tensile pressures, and the molecular displacement is more likely to occur under compressive pressures. This phenomenon indicates that under tensile and compressive pressures, the hydrate cages have two different mechanisms to react. Also, compared the changing magnitude of both types of cages, the large cages are more stable under pressures.

### 4.8.4 Bond Parameters (SI4)

This supplementary information SI4 discusses the performance on the bond parameters (OH hydrogen bond lengths, OH covalent bond lengths, OO distances, OOO angle and HOH bond angles) presented in Section 4.5.2 of the paper. Among these five parameters, the most important bond length and angle are: OH hydrogen bond length and OOO angle respectively. Since these two parameters can reflect the cage behaviour directly. All five parameters will be discussed below.

#### OH hydrogen bond length

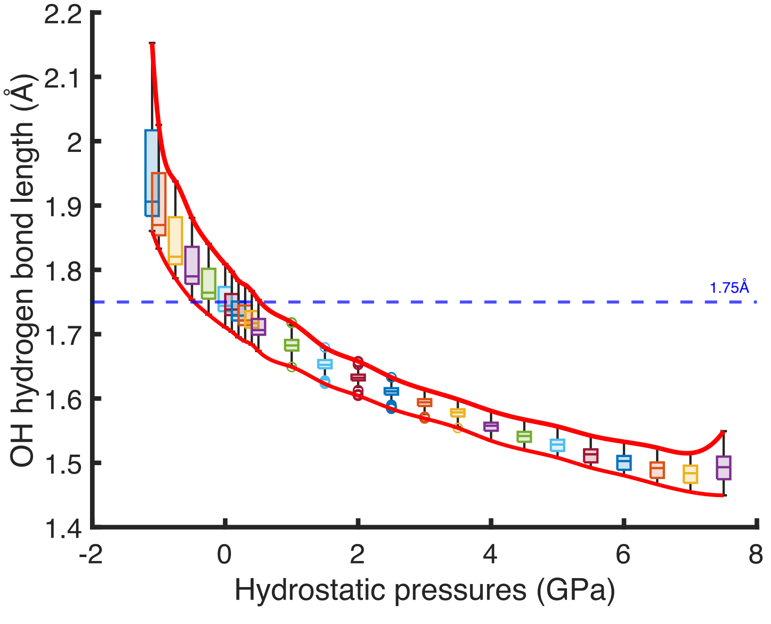

*Figure 4-10 OH hydrogen bond length distribution under pressures from -1.1 GPa to 7.5 GPa. 92 hydrogen bonds are in one unit lattice, and each bond has its own length under a specified pressure. Under each pressure, the hydrogen bond lengths is shown in the box and whiskers. The top and bottom of each box are the 25 and 75 percentiles of the bond lengths under a specified pressure, respectively. The line in the middle of each box is the median. The whiskers are the lines extending above and below the box to the maximum value and minimum values of the bond lengths under the pressure. The two red lines show the evolutions of maximum and minimum values under pressures. The blue dash line is for H-bond in ice at 1.75Å.*

Figure 4-10 shows the response of OH hydrogen bond lengths under pressures from -1.1 GPa to 7.5 GPa. The two red lines are created by the maximum and minimums values. Their symbols within the upper and lower values denote the following: the height of middle box is the 25-75% percentile of the distribution, the middle segment is the median, and the length of upper and lower vertical connectors illustrate the variance. As the hydrate lattice is mainly supported by the hydrogen bonds, the hydrogen bond lengths correspond to the selected lattice size. In Figure 4-10, the OH hydrogen bond lengths decrease as the hydrostatic pressures increase. The sensitivity of hydrogen bond lengths is much greater under tensile pressure than under compressive pressures.

The size of the box and the position of median can summarize key information on the hydrogen bond length distribution. When the tensile pressures are applied, the position of the entire box and connectors move upwards and their lengths increase. However, the position of the median value is still closer to the bottom of the box. This indicates that the 25 and 50 percentile are very close and the distribution inside the box is not uniform, implying a negative skewness distribution. The upper connector become longer once the tensile pressures become greater. This implies the initial long hydrogen bonds are more sensitive to the tensile pressures compared with the short hydrogen bonds, which indicates a greater standard deviation. Once the compressive pressures are applied, the range of the box-connectors becomes smaller, the upper and lower connectors keep a similar length and the median locates at the centre of the box, which is a good indication of a normal distribution, zero skewness. The smooth and consistent tendency is maintained until 7.5 GPa. Once 7.5 GPa is applied, the range of the box-connectors becomes greater and the position move upwards, indicating a positive skewness, which is opposite to the previous tendency and is a robust indication of approaching a stability limit.

## OOO Angle

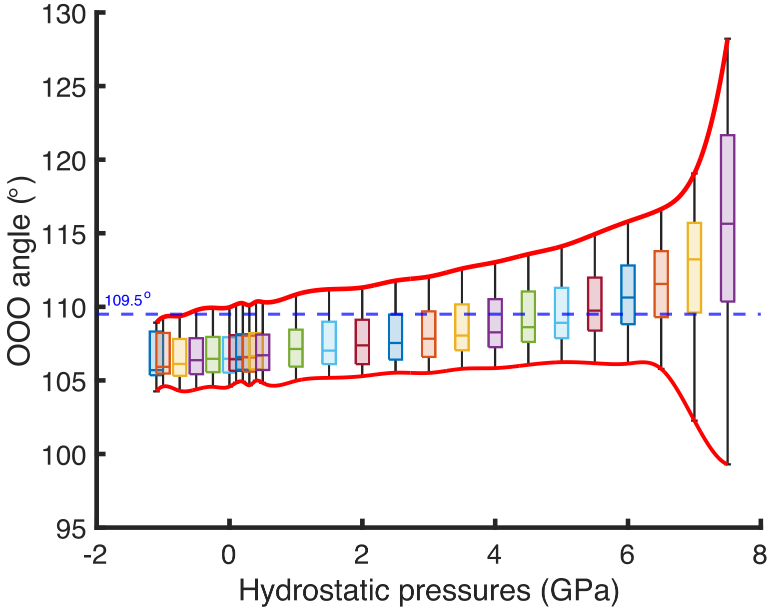

*Figure 4-11 OOO angle distribution under pressures from -1.1 GPa to 7.5 GPa. 46 OOO angle are in one unit lattice. Under each pressure, the OOO angels are shown in the box and whiskers. The top and bottom of each box are the 25 and 75 percentiles of the angles under a specified pressure, respectively. The line in the middle of each box is the median. The whiskers are the lines extending above and below the box to the maximum value and minimum values of the OOO angles under the pressure. The two red lines show the evaluations of maximum and minimum values under pressures. The horizontal dash line is the ideal tetragonal angle* 109.5°.

Figure 4-11 shows the OOO angle distribution from -1.1 GPa to 7.5 GPa. This angle is a representative parameter to evaluate the water network system and structure. The ideal tetrahedral angle for tetragonal coordination is 109.5°. In principle, the HOH water bond angle is 104.45°. In the ideal case, the structure of one single water molecule and the structure forming by the water molecule and the adjacent four water molecules are tetrahedral, and thus the OH covalent bond and the OH hydrogen bond should be on the same horizontal line, which is the most uniform and stable structure for one central atom with four substituents, and the OOO angle should be the same as the HOH angle. However, in reality the OH covalent bond and OH hydrogen bond are not on the same line due to the intermolecular interactions and the applied pressures. Meanwhile, the lone pair of electrons belonging to the water oxygen atoms distort the water molecule angle (HOH angle) from 109.5° to 104.45°. Thus, there is a discrepancy between the standard values of OOO angle and the HOH angle.

OOO angle can capture the interactions between water molecules. From Figure 4-11, it shows the distribution of OOO angle becomes wider as the pressure increases. The two red lines are the maximum and minimum values along with pressures, which shows a funnel effect. This diverging tendency means the interactions among the water molecules cannot be maintained in the tetrahedral structure. Once 7.5 GPa is applied, the spread of the OOO angle values diverges so that most angles are not close to 109.5°.

Additionally, as the pressures increase, the box and whiskers change their sizes and positions. The box size increases as the pressures increases. This can be explained as under high pressures, the atoms or molecules could not move or get closer in the initial bonding directions with the limited volume. Thus, the atoms or molecules would prefer to deviate from their initial direction and the OOO angles get wider. Inside the box, from 0 GPa to -1.1 GPa, the median is closer to the bottom of the box. This implies that although there is a wide distribution, most OOO angles are still around 105°, which is the standard angle value for water molecule. Also, the difference between the maximum and minimum values are small between -1.1 GPa to 0.5 GPa, approximately 5°. As the pressure increases, the median moves to the centre of the box, which is an indication of the normal distribution. But the sudden open-funnel effect at 6.5 GPa is an indication of instability as well.

To conclude the behaviours of OH hydrogen bond lengths and OOO angles, we found that under high pressures the OH hydrogen bond lengths would shrink at the expense of the larger OOO angles. Thus, the lattice volume would become smaller and some shape deformation or plane tilting are expected under high pressures.

## HOH bond angles

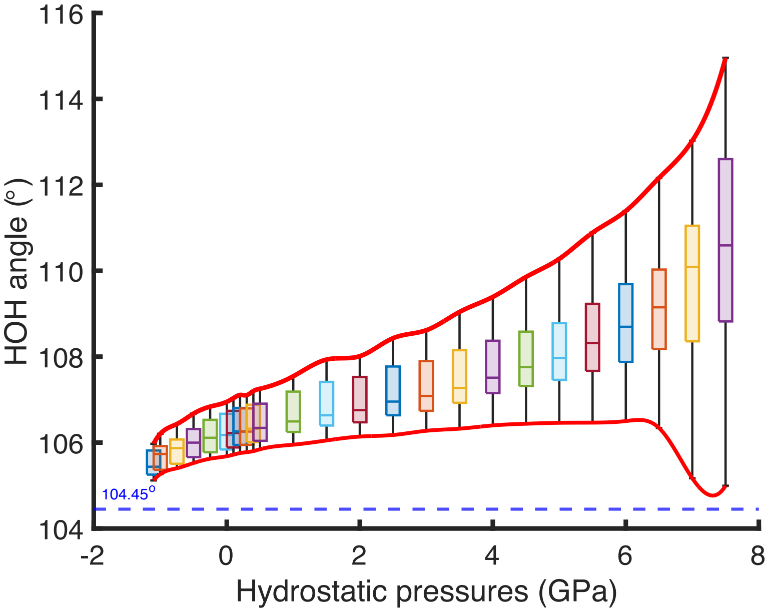

*Figure 4-12 HOH bond angle distribution under pressures from -1.1 GPa to 7.5 GPa.*

HOH bond angle, also called water molecule angle, which reflects the intrinsic reaction of the water molecules under pressures. In Figure 4-12, before 6.5 GPa, a steady increasing and expanding spread is showing. The box size becomes large when the pressure increases, and the difference between the maximum and minimum values becomes greater as well. The median values present a similar behaviours as those in the other bond parameters. It locates close to the box bottom when the pressures are low, and move to the centre of the box as pressures increase.

The most interesting feature of the HOH angle distribution is the upper and lower bound tendency when approaching the compressive pressures. A sudden wide spread takes place once 6.5 GPa is applied. The maximum values show an exponential increase. However, the minimum values show a sudden decrease and keep the angle value between 104° and 105°.

The lower bound of HOH angle is always greater than the standard tetrahedral angle 104.45° can be explained as the distribution of energy intensity.[36] 104.45° has been recognized as the most stable energy distribution for the tetrahedral structure. If the bond angle becomes greater, the energy can be spread on a greater area. However, if the bond angle becomes smaller, the energy accumulates at one spot, which will lead to uneven energy distribution for the entire lattice. Thus, the lower bound of HOH bond angle is always greater than 104.45°.

## OH covalent bond length

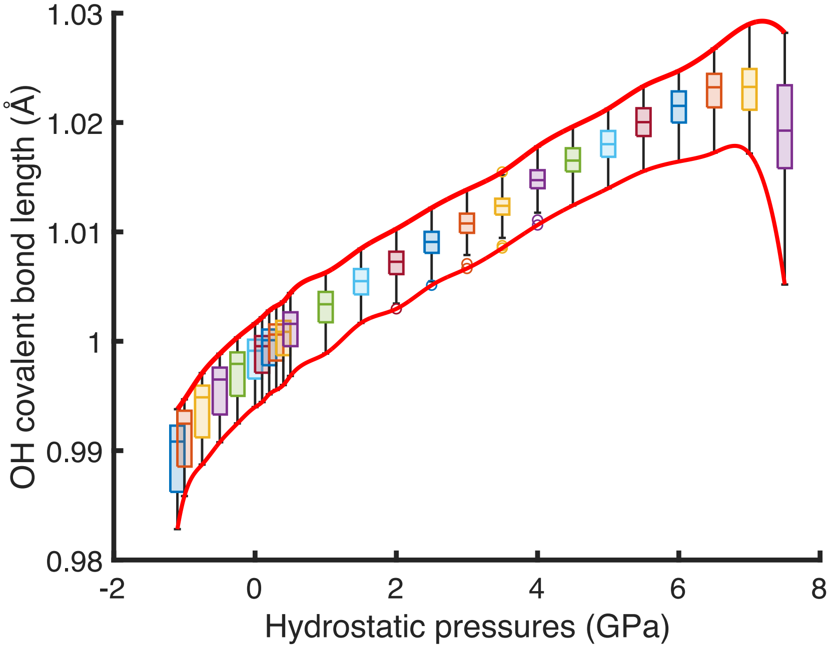

*Figure 4-13 OH covalent bond length distribution under pressures from -1.1 GPa to 7.5 GPa. The two red lines show the evolutions of the maximum and minimum values under pressures.*

Figure 4-13, shows the distribution of OH covalent bond lengths under pressures from -1.1 GPa to 7.5 GPa. An increasing tendency is observed from -1 GPa to 6.5 GPa, which is completely different from the evolution tendency of OH hydrogen bond lengths. These opposite behaviours imply the compensation mechanism present in the hydrate system, which have been verified by several groups.[27] The main principle is that there are one OH hydrogen bond and one OH covalent bond between two water oxygen atoms. Once one of these two bonds stretches or shrinks, the other bond would shrink or expand to compensate.

Between -1 GPa and 6.5 GPa, the evolution of the OH covalent bond length is very stable. The difference between the maximum and minimum values at each pressures is almost constant. Inside the box, the median is closer to the top of the box when the pressures are from -1 GPa to 0.5 GPa. After 0.5 GPa, the median moves to the centre box. This phenomenon is very similar the behaviours in OH hydrogen bond length discussed in Section 4.5.2.

Once -1.1 GPa is applied, the changing magnitude becomes more significant but still keeps the same tendency. However, when 7.5 GPa is applied, both evolving tendency and magnitude change significant. The discrepancy between the maximum and minimum values changes from 0.015 Å to 0.028 Å, which is nearly twice the magnitude as before. These abnormal behaviours indicates the stable pressure limits are reached.

## OO distances

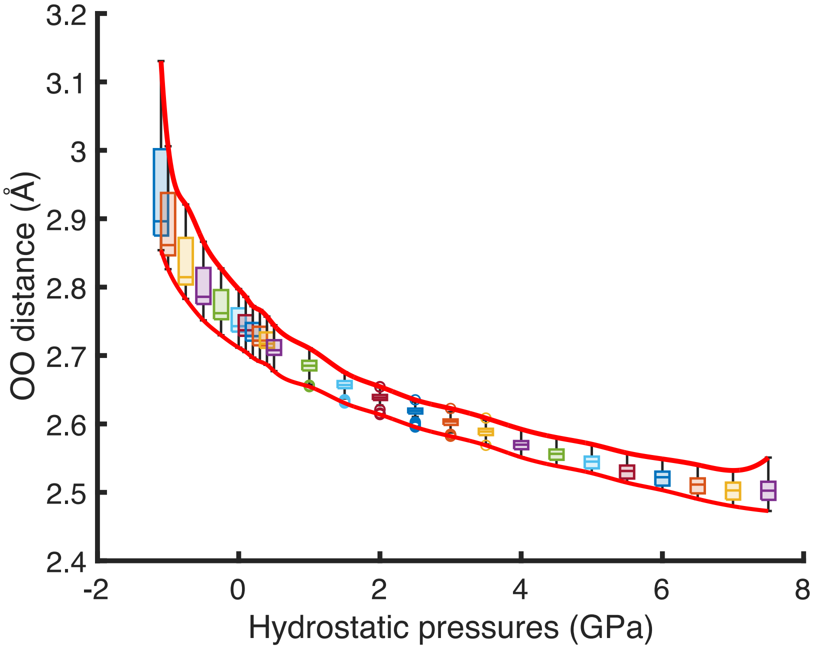

*Figure 4-14 OO distance distribution under pressures from -1.1 GPa to 7.5 GPa. The two red lines are the maximum and minimum values under each pressure.*

Figure 4-14, shows the OO distance distribution under pressures from -1.1 GPa to 7.5 GPa. It shows a similar tendency as the OH hydrogen bonds. In the ideal case, the OO distance is the sum of the OH hydrogen bonds length and the OH covalent bond length, the two water oxygen atoms and the hydrogen are on the same line. Considering all three bond lengths, it can be concluded that OH hydrogen bond length dominates the OO distance performance. The compensation mechanism would not have an impact on the cage or lattice, since all the effects have been offset by the OH hydrogen bond lengths.

## Bond length versus bond angle

To investigate the interaction of bond angle and length under pressures, two pairs of bond angle and bond lengths were selected. They are OH covalent bond length vs HOH bond angle (water molecule) and OH hydrogen bond length vs. OOO angle (water molecule interactions), as shown in Figure 4-15.

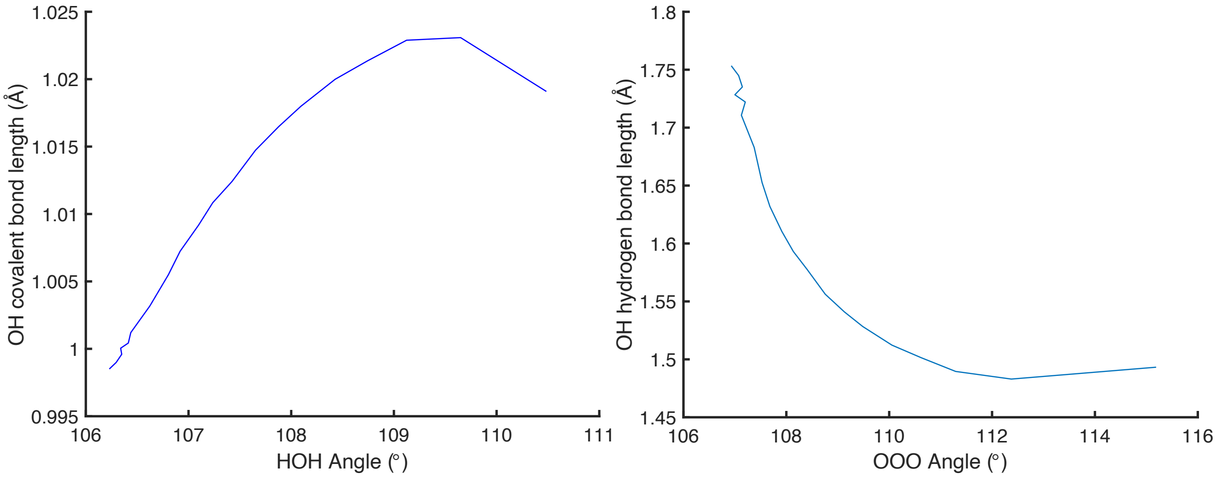

*Figure 4-15 OH covalent bond length vs. HOH angle (left) and OH hydrogen bond length vs. OOO angle (right)*

Figure 4-15 shows the OH covalent bond length vs HOH bond angle and OH hydrogen bond length vs. OOO angle from 0 GPa to 7.5 GPa. The mean values are selected for each bond parameter for plots. For Figure 4-15 (left), it shows that both OH covalent bond length and HOH angle increase as pressure increases until 7 GPa. Once 7.5 GPa is applied, the HOH angle still keeps the increasing tendency; however, the OH covalent bond length shrinks. This abnormal behaviour can be explained by approaching the stability limits and indicates that the bond angle is more pressure resistant than the bond length. The sudden decrease of OH covalent bond length implies that the water molecules start to sacrifice under 7.5 GPa.

The increasing magnitude of both OH covalent bond length and HOH angle seems to be a constant between 0 GPa to 6 GPa. The small fluctuations between 0 GPa and 0.5 GPa can be explained the small increment (0.1 GPa) selected, which might be too small to reflect the piezo effect on the bond length and angles. Beyond 6 GPa, the HOH angle seems to increase at the faster rate; however, the OH covalent bond length seems to reach a steady state and increase with a slow rate. The different responses of OH covalent bond length and HOH bond angle at high pressure region ( > 6GPa) indicates that the water molecules prefers angle changes rather than bond length under extreme high pressure conditions.

For Figure 4-15 (right), it shows the relationship between OH hydrogen bond length and OOO angle from 0 GPa to 7.5 GPa. The OH hydrogen bond length shows an opposite behaviours compared with the OH covalent bond length. It first decreases as the pressures increases. The decreasing tendency of OH hydrogen bond length is significant between 0 GPa and 6 GPa. Beyond 6 GPa, the OH hydrogen bond length becomes a constant, approximately 1.47 Å until 7 GPa. Once 7.5 GPa is applied, the OH hydrogen bond length seems to increase, which corresponds to the sudden decrease of OH covalent bond length. For the OOO angle, it increases faster under great pressures. A sudden increase from 112.2°to 115.2° when the pressure changes from 7 GPa and 7.5 GPa, implying the initial arrangement between water molecules is not able to withstand 7.5 GPa. Thus, a sudden increase of OOO angle to rearrange the structure is observed which can also probably indicate the trigger of a  fracture mechanism.

To conclude, within the stability limits, bond length and bond angle should show a linear relationship. When approaching the stability limits, the bond length will not change significantly, but the bond angle keeps increasing. Once the stability limit is approached, the bond length will show a opposite behaviour and the bond angle will increase significantly.

# Chapter 5

# 5 DFT-continuum Characterization of Third-order Elasticity of sI Methane Hydrates under Pressure

---

*Reproduced with permission from Zhu, X., Guerra, A., Servio, P. & Rey, A. D. DFT-continuum characterization of third-order elasticity of sI methane hydrates under pressure. Materials Research Express, doi:10.1088/2053-1591/acbf0a (2023).Copyright [2023] IOP Publishing*

## 5.1 Preface

As highlighted in Chapter 3, the second-order elastic constants (SOECs) are indispensable for calculating mechanical properties in all materials, including gas hydrates. In other words, the values of SOECs under varying pressures are a fundamental component of material physics. Nevertheless, due to the high computational cost and the time required to obtain the values at each pressure, the simulation method mention in Chapter 3 is essentially not viable in the long run. To overcome this limitation, it was proposed to use higher-order elastic constants, such as third-order elastic constants (TOECs), to estimate the effects of pressure on the SOECs. After establishing the non-trivial relationship among the TOECs, SOECs and pressure, the values of SOECs and TOECs at zero pressure only are needed for the calculation of SOECs under pressure. Then the mechanical properties, and pressure stability limits under any pressure can be estimated.

To achieve the aforementioned objective, the TOEC values at zero pressure were first determined. Elastic3rd, an open-source Python package was utilized for calculating third-order elastic constants from first-principles computations. After obtaining the TOEC values, two fittings were used to predict the SOEC values under pressure. The first nonlinear equation involves both the SOEC and TOEC values at zero pressure. The second fitting only includes the SOEC values at zero pressure. Both fittings were compared with the results of DFT-based direct numerical simulation (DNS), which are presented in Chapter 3, to determine the accuracy of the fittings. When the strains exceeded 3%, the results indicated that non-linear fitting, which involves TOECs, is required to predict the SOECs values under pressure. In addition, the SOECs values derived from this non-linear fitting provide more accurate predictions in terms of Born stability criteria and transition from ductile to brittle. In conclusion, the TOEC values can save considerable computational time and resources when calculating SOEC values under pressure. Additional calculations and evaluations on the mechanical properties and the stability have been successfully implemented and validated. Consequently, these findings and established relationships can also be utilized for other hydrate-based systems.

## 5.2 Abstract

Methane gas hydrates (GHs) are polyhedral crystalline guest-host materials found under high pressure and low-temperature conditions, which can serve as an energy source. Previous work on methane GH material physics was limited to simple linear models, which only involves second-order elasticity. However, this is not fully suited to high-stress load conditions in technological applications and fundamental material physics. For other material systems, it has been demonstrated that third-order elasticity and pressure derivatives of second-order elasticity have a strong and hence significant correlation. To narrow a critical theory-simulation gap in gas hydrates materials research, in this work we expand prior work from second-order elastic constants (SOECs) to third-order elastic constants (TOECs). By using the open-source Python tool Elastic3rd and the DFT calculation software Vienna Ab initio Simulation Package (VASP), we found that the non-linear fitting involving TOECs gave a better overall prediction and a smaller root-mean-square deviation on pressure-strain evaluation when compared with linear fitting. In addition, the non-linear fitting provides robust results on the piezo-effect on the shear constant $C_{44}$ and the ductile-to-brittle transition (P=-0.5 GPa). These results are not achievable from previous work based on a linear model and these findings prove that non-linear models, including TOECs, are needed under high pressures. In addition, this research includes a detailed analysis of the calculation of TOECs and mechanical properties to study pressure stability limits and ductile-

brittle transitions. Together the results, findings, and analyses from this work are a novel and significant contribution to the material physics knowledge of gas hydrates and hydrogen-bonded crystalline materials.

## 5.3 Introduction

Extreme environments are always an important area of material science and technology investigation. These severe conditions (e.g., high pressures and low temperatures) preclude routine laboratory research. As a result, theoretical and computational modelling are indispensable to characterize material properties under high pressure-low temperature conditions. For routine material characterization, linear elastic theory has been widely applied to evaluate elastic constants/ mechanical properties. However, a wide range of research shows that the second-order elastic constants (SOECs) have intrinsic limitations due to linearity. On the other hand, higher-order elastic constants can overcome the SOECs' limitations and describe non-linear responses, which can provide more accurate high-fidelity results. Third-order elasticity has been proven that they have a strong relationship with the pressure derivative of second-order elastic constants (SOECs)[1]. It is noteworthy that TOEC calculations have already been performed on metallic materials[2,3]. Several research groups have also found that third-order elastic constants can provide reliable predictions on piezo-elastic effects on the elastic constants[1,4]. De Jong, M., et al.[5] showed that the SOECs and TOECs can provide reliable indications on the ductile-to-brittle transitions and the failure mode under uniaxial loading. The type of mechanical instability can also be revealed. Kaga, H.[2] presented that for calcite, the SOECs and TOECs can be used to calculate the pressure derivative of the bulk modulus. The results remarkably agreed with Bridgman's data for the change in compressibility with pressure[2]. Wang, X., et al.[3] found that the third-order elastic constants from first principle calculations by an energy-strain methodology are extremely useful in characterizing and understanding the anharmonicity of ZnO due to finite strain. Importantly, the TOEC can be used to calculate the strain-dependent mechanical properties, such as Young's moduli.

TOEC computations have so far been limited to metallic and ceramic materials and experimental data on the topic is scant. Calculations and experimental measurements targeting TOEC on a complex crystalline material such as gas hydrates and their associated applications have not been fully explored. Thus, in this work, we will use a particular gas hydrate as a target material system, which has a unique guest-host hydrogen-bonded structure. To better evaluate the results from computational techniques with supporting experimental data, our research team has created an integrated experimental-computational platform for studying the materials science of gas hydrate systems[6]. This has resulted in contributions to the study of interfacial phenomena[7,8] as well as the physical and transport aspects of gas hydrate systems[9-15]. Details of gas hydrates and previous work are discussed below.

Gas hydrates (GHs), a novel water-based guest-host crystalline material, usually appears in the deep ocean and permafrost area[16]. It encompasses a special guest-host structural feature, which provides significant gas storage capacity. The lattice structure of clathrate hydrates is formed by the hydrogen bonds of water and the entire structure is thermodynamically stabilized by the presence of trapped gas molecules and distributed van der Waals forces[17]. When brought to the surface, 1 $m^3$ of hydrate can release 160 $m^3$ of gases[18]. In nature, 80% of hydrates contain natural gas, which is mostly composed of methane[19]. With a conservative estimation, the energy contained in natural hydrates is at least twice the amount of the currently explored fossil fuels[20]. However, the harsh circumstances prevent commercial exploration and laboratory study; therefore the performance of hydrates under high pressure is rarely studied. Thus, computational simulation becomes a more feasible approach to examine hydrates' mechanical properties and stability under extreme conditions.

Previous work has been directed to study gas hydrates' mechanical and thermodynamic properties under pressure. Vlasic, T. M., et al.[10] evaluated the sII hydrates' robustness through the equation of state formulation (EOS) and the effects of different guest molecules on the hydrates' mechanical properties. They found a positive linear relationship between the bulk modulus and the hydrogen bond density. Also, they determined that the larger gas molecules would push outward on the cages through van der Waals repulsions, increasing the size of cages and then increasing the lattice volume. Daghash, S., et al.[21] characterized the sH gas hydrate's properties under pressure by first-principles DFT. The pressure-effects on five second-order elastic constants were evaluated. Positive tendencies have been present in all SOECs (Second Order Elastic Constants). Same piezo effects take place on bulk modulus, Young's modulus, and shear modulus as well. Also, Daghash, S. M., et al.[22] illustrated the pressure dependency of the hydrate's bulk, shear and Young's moduli, Poisson's ratio, and the speed of sound in the hydrate structure. Mathews, S. L., et al.[23] investigated the sI hydrate's thermodynamic properties under different temperatures and had a robust conclusion that DFT (Density Functional Theory) can give more reliable results than molecular dynamics (MD) under lower temperatures. Jendi, Z. M., et al.[24] reported that the tensile and compressive ideal strengths of sI pure methane gas hydrates are -1.10 GPa and 90 GPa, respectively, by using density functional theory. Jia, J., et al.[25] figured out that there were significant relationships between the elastic modulus and pressure. Mirzaeifard, S., et al.[7] calculated the water-methane surface tension using pressure and temperature relationships that agreed with conventional scaling principles. Guerra, A., et al.[26] studied the temperature and pressure effects on the viscosities of methane and carbon dioxide hydrates. They found temperature usually resulted in one order of magnitude larger viscosity effects than pressures. Also, the influence of pressure on the viscosity of carbon dioxide hydrate systems was one order of magnitude greater than that of methane hydrate systems. These findings imply that there are strong relationships between the hydrates' mechanical properties and temperature and pressures

As mentioned above, previous work on SOECs under pressure has revealed that SOECs values can be used to predict the mechanical properties under limited pressure ranges. To improve the modelling process and fill the knowledge gap on hydrate TOECs, in this work, we will first calculate TOECs values at zero pressure and identify the advantages of using TOECs for SOECs prediction under pressure. We used the open-source Python package Elastic3rd, a tool for calculating third-order elastic constants from first-principles calculations[4]. Vienna Ab initio Simulation Package (VASP) was selected to perform all the first-principles calculations. Specifically, the sI methane hydrate structure was selected to be the studied material in this project. All simulations were performed at zero Kelvin. No gas hydrates' structural transition was considered during simulation. It is known that occupancy impacts stability, as lower occupancy is less stable under the same condition. However, in this project, we only consider the 100% occupancy case. In other words, each cage is occupied by a methane molecule. Any considerations related to occupancy, temperature and structural transition are out of this project's scope.

The organization of this paper is as follows. In section 2, all the methodologies and computational software used in this work will be discussed. Section 2.1 discusses the algorithm of the energy-strain method. Section 2.2 presents the detailed information on the DFT simulations, and sI methane hydrates' structure Section 2.3 introduces three material characterization methods that were applied in this study. Section 2.4 and 2.5 shows the equations for Born Stability criteria and Pugh's ratio and Pettifor criterion respectively. In Section 3, all the results obtained for SOECs and TOECs under zero pressure will be presented. Section 5.5.1 demonstrates the values of SOECs and TOECs under zero pressure for the sI methane hydrates. Section 5.5.2 shows the relationship between hydrostatic pressures and strains and the relationship between SOECs under pressures and strains. Section 5.5.3 demonstrates the values of SOECs under pressure by three different characterization approaches. Section 5.5.4 presents the values of mechanical properties under pressures estimated by non-linear fitting involving TOECs. Section 5.5.5 shows the hydrate's stability evaluated by Born Stability Criteria. Section 5.5.6 shows the prediction on the ductile-to-brittle transition by using classical Pugh ratio and Pettifor criteria. Section 5.5 presents the conclusions, novelty, and significance of this work. All the technical details are given in the Supporting Information (SI), including specific examples.

We wish to emphasize that we use DFT at zero Kelvin and that the material symmetries of the gas hydrates remain cubic at all pressures, and that the studied thermodynamic phase known sI methane gas hydrate does not transform into other gas hydrates such sII or other structures through complex nucleation and growth and/or spinodal decomposition and/or complex polyhedral transformations. The methane sI hydrate has full gas occupancy and periodic boundary conditions are always applied in the simulations, representing an infinitely large material volume. Conditions, symmetries, chemical composition and processes beyond those described above are outside the scope of the present work.

# 5.4 Methodology

## 5.4.1 Energy-strain Methodology

This section briefly introduces the basics of the energy-strain method used for the calculations of elastic constants in this paper[27-29]. While stress-strain analysis can be applied, the energy-strain method is preferable based on the results from previous work[14,30,31]. Within the stability region, the lattice energy E is given by an expansion of the applied strains $\eta_{ij}$[32], as shown in Eqn (5.1). The Eqn (5.1) presented below, is expanded to the third-order, which is the maximum order of applied strain $\eta$:

$$E = E_0 + V_0\left(\frac{1}{2!}C_{ijkl}\eta_{ij}\eta_{kl} + \frac{1}{3!}C_{ijklmn}\eta_{ij}\eta_{kl}\eta_{mn} + \cdots\right) \qquad (5.1)$$

where $E_0$ is the ground-state energy of the unstrained system, $V_0$ is the unstrained lattice volume, the strain subscripts $\{ij, kl, mn\}$ represent spatial directions, $C_{ijkl}$ are the second order elastic constants and $C_{ijklmn}$ the third order ones. The symmetry properties of these latter tensors are dictated by the Voigt symmetries and lattice symmetry[33,34], which in our case is always cubic. sI methane hydrate has a cubic structure, and thus it only has three SOECs and six TOECs. The detailed definition of elastic constants and the simplification process for the cubic material are shown in the Supporting Information 1 (SI1).

To obtain the values of elastic constants ($C_{ijkl}, C_{ijklmn}$), imposing cubic symmetry, using Voigt notation[33,34] and known Lagrangian strains, Equation (5.1) can be expressed in scalar form as Equation (5.2)[4]:

$$\frac{E - E_0}{V_0} = \frac{1}{2!} A_2 \eta^2 + \frac{1}{3!} A_3 \eta^3 + \cdots \qquad (5.2)$$

$E - E_0$ and $V_0$ are found from our DFT simulations, the applied strains $\eta$ are known independent variables and the material property functions ($A_2$, $A_3$) are the unknowns, resulting in a classical inverse problem[2,4]. In this work, the Lagrangian strain $\eta$ is the applied strain for energy-strain calculation. $A_2$ and $A_3$ are linear functions of second-order elastic constants and the third-order elastic constants, respectively; see Table 5-1 for the correspondence between $A_2$ and SOECs, and the correspondence between $A_3$ and TOECs.

Table 5-1 is valid if Eqn (5.2) terminates at cubic terms. If Eqn (5.2) ends at quadratic terms, $A_2$, then different strain sets must be applied. Details are shown in the Supporting Information (SI2).

Table 5-1, shows the definitions $A_2$ and $A_3$ for the six selected strain modes (M1-M6) for gas hydrates, again using the Voigt notation. Six strain modes were applied because there are six third-order elastic constants for cubic structures. In this work, the applied strains η vary from -6% to 6% with increments of 2%. This range and step increase captures the non-linear response of the system and ensure the results' accuracy.

*Table 5-1. Lagrangian strain modes ($Mi$) and the corresponding coefficients for cubic symmetry4*

*(see Eqn. (5.2))*

| No. | $A_2$ | $A_3$ | Strain mode (M) |
|---|---|---|---|
| M1 | $C_{11}$ | $C_{111}$ | $[\eta, 0,0,0,0,0]$ |
| M2 | $2C_{11}+2C_{12}$ | $2C_{111}+3C_{112}+3C_{113}$ | $[\eta, \eta, 0,0,0,0]$ |
| M3 | $C_{11}+4C_{44}$ | $C_{111}+12C_{144}$ | $[\eta, 0,0,2\eta, 0,0]$ |
| M4 | $C_{11}+4C_{44}$ | $C_{111}+12C_{155}$ | $[\eta, 0,0,0,2\eta, 0]$ |
| M5 | $3C_{11}+6C_{12}$ | $3C_{111}+9C_{112}+9C_{113}+6C_{123}$ | $[\eta, \eta, \eta, 0,0,0]$ |

|  |  |  |  |
|---|---|---|---|
| M6 | $12C_{44}$ | $48C_{456}$ | $[0,0,0,2\eta,2\eta,2\eta]$ |

Note: In M2 and M5, the elastic constant $C_{112}$ equals to $C_{113}$.

In partial summary, the energy-strain method results in an inverse problem where the unknowns are the second- and third-order elastic constants and the known values are the applied strain ($\eta$) inputs and DFT-computed energy outputs. A representative example on calculating the SOECs and TOECs is shown in Supporting Information (SI2).

## 5.4.2 DFT Simulations and sI Methane Hydrate Structure

DFT computations are performed using the VASP software[35] which can relax the lattice to its lowest-energy state. To start a DFT simulation, a unit lattice of sI methane hydrate must be constructed. Periodic boundary conditions are applied. The water molecules build the hydrate lattice, where two small cages ($5^{12}$) and six large cages ($5^{12}6^2$) are involved in one unit lattice. The abbreviation $5^{12}$ stands for polyhedrons that contain 12 pentagonal faces. The abbreviation $5^{12}6^2$ stands for polyhedrons that contain 12 pentagonal faces and two hexagonal faces. The initial atomic positions of oxygens and hydrogens were proposed by Takeuchi, F., et al.[36]. The oxygen atoms' positions were obtained from the X-ray diffraction and hydrogen atom's positions were followed the Bernal-Fowler ice rules[37]. Methane molecules were selected to be the only guest molecules in the simulation box. As above-mentioned we assume 100% occupancy, such that each cage has a methane molecule at the centre in the initial structure. The details of structural information are summarized in Supporting Information 3 (SI3) and our previous work[14].

Besides the structural configuration, constraint parameters are fixed to specify the relaxation mode. A conjugate gradient algorithm was used, and the cut-off energy, 520 eV was selected, which was at 30% above the maximum element energy. The electronic energy tolerance used was $10^{-4}$ eV, and the ionic optimization force tolerance used was 0.5 meV/Å, in accordance with our previous work[12,23,38,39]. Projector augmented wave potential[40,41] were employed for all calculations. The revised Perdew-Burke-Ernzerhof (revPBE) exchange correlation functional with DFT-D2 dispersion correction were applied based on their great performance in our previous work[14,15,31]. We used a gamma-centered $4 \times 4 \times 4$ mesh to ensure proper convergence with respect to the total energy for all systems[14,15]. A summary of these parameters is shown in Supporting Information 3 (SI3).

### 5.4.3 Three Material Characterization Methods

In this paper we use, integrate and compare three calculation methods to evaluate gas hydrates' performance under arbitrary pressure:

1. Direct Numerical Simulation (DNS): (i) use the energy-strain method to calculate SOEC at zero pressure and (ii) under arbitrary pressures;
2. Linear Model (L): (i) use the energy-strain method to calculate SOEC at zero pressure and then (ii) using continuum formulation to calculate SOEC under pressure using (i);
3. Nonlinear Model (NL): (i) use energy-strain method to calculate SOEC and TOEC at zero pressure, and (ii) use continuum formulation to calculate SOEC under pressure using (i).

The direct numerical simulation (DNS) method uses the energy-strain method to obtain SOECs at zero pressure and under load. In other words, under zero pressure or load, the lattice system will first completely relax to its ground state. Then the strains would be applied to calculate the strained system energy. The predictions of this methods serve as a reference frame. The details of executing the energy-strain equation, shown as Eqn (5.3), and the highest order is quadratic. $A_2$ is the coefficient, which involves the SOECs values.

$$\frac{E - E_0}{V_0} = \frac{1}{2!} A_2 \eta^2 \tag{5.3}$$

The linear model (L) uses the same energy-strain Equation as DNS, Eqn (5.3), to obtain SOECs at zero pressures. Then Eqns. (5.4-5.7)[42] were applied for the predictions of SOECs under pressure. The deformed strain $\varepsilon$, is defined as the uniformed deformation in x, y, z directions due to hydrostatic pressure P:

$$\mathrm{P} = \frac{-1}{\sqrt{1+2\varepsilon}} [(C_{11}^{o} + 2C_{12}^{o})\varepsilon] \tag{5.4}$$

$$C_{11} = \sqrt{1+2\varepsilon} C_{11}^{o} \tag{5.5}$$

$$C_{12} = \sqrt{1+2\varepsilon} C_{12}^{o} \tag{5.6}$$

$$C_{44} = \sqrt{1+2\varepsilon} C_{44}^{o} \tag{5.7}$$

However, for the non-linear method (NL), a different energy-strain equation was applied, Eqn (5.8), for the calculation of SOECs and TOECs under zero pressure. Compared with Eqn (5.3), an extra term is involved, $A_3$ , which includes the TOECs:

$$\frac{E - E_0}{V_0} = \frac{1}{2!} A_2 \eta^2 + \frac{1}{3!} A_3 \eta^3 \tag{5.8}$$

Once the SOECs and TOECs under zero pressures are obtained, the predictions of values under pressure are found using Eqn (5.9-5.12)[42]. The definition of deformed strain $\varepsilon$ is the same as in the equations shown above.

$$\mathrm{P} = \frac{-1}{\sqrt{1+2\varepsilon}} \left[ (\mathrm{C}_{11}^{o} + 2\mathrm{C}_{12}^{o})\varepsilon + \left( \frac{1}{2} \mathrm{C}_{111}^{o} + 3\mathrm{C}_{112}^{o} + \mathrm{C}_{123}^{o} \right) \varepsilon^2 \right] \tag{5.9}$$

$$\mathrm{C}_{11} = \sqrt{1+2\varepsilon} [\mathrm{C}_{11}^{o} + (\mathrm{C}_{111}^{o} + 2\mathrm{C}_{112}^{o})\varepsilon] \tag{5.10}$$

$$\mathrm{C}_{12} = \sqrt{1+2\varepsilon} [\mathrm{C}_{12}^{o} + (2\mathrm{C}_{112}^{o} + \mathrm{C}_{123}^{o})\varepsilon] \tag{5.11}$$

$$\mathrm{C}_{44} = \sqrt{1+2\varepsilon} [\mathrm{C}_{44}^{o} + (\mathrm{C}_{144}^{o} + 2\mathrm{C}_{155}^{o})\varepsilon] \tag{5.12}$$

Summarizing, we find:

$$\mathrm{SOEC}^{\mathrm{DNS}}(\mathrm{P}=0)=\mathrm{SOEC}^{\mathrm{L}}(\mathrm{P}=0)\neq\mathrm{SOEC}^{\mathrm{NL}}(\mathrm{P}=0)$$

$$\mathrm{SOEC}^{\mathrm{DNS}}(\mathrm{P})\neq\mathrm{SOEC}^{\mathrm{L}}(\mathrm{P})\neq\mathrm{SOEC}^{\mathrm{NL}}(\mathrm{P})$$

The main goal to use three different characterization methods to evaluate the SOECs values under pressures is to assess how well the linear and non-linear models perform when compared with DNS. DNS approach is considered the most reliable one because there are no fitting process applied. However, the time and computational cost for DNS are significant. Thus, if the linear and non-linear models generate accurate results of SOECs under pressure, then more cost-effective high-fidelity methods can be deployed with confidence.

## 5.4.4 Born Stability Criteria

Born stability criteria[43,44] are widely used for estimating a material's stability under different pressures using SOECs. Since SOECs are known to change with pressure[14], the pressure term should be included while evaluating stability. If one of these criteria is violated, it indicates material failure The simplified Born stability conditions for cubic material under load are given by[45,46]:

$$B_T=(C_{11}+2C_{12}+P)/3>0 \tag{5.13}$$

$$G'=(C_{11}-C_{12}-2P)/2>0 \tag{5.14}$$

$$G=4(C_{44}-P)>0 \tag{5.15}$$

where $B_T$ is the bulk stiffness modulus, $G'$ the tetragonal shear stiffness modulus, and $G$ is the rhombohedral shear stiffness modulus. The entire resistance of the material to tensile and compressive pressures is determined by Equation (5.13). Equation (5.14-5.15) incorporates the shear stress applied on the system.

## 5.4.5 Pugh’s Ratio and Pettifor Criterion

Two common metrics for determining a material's ductility and brittleness are the Pugh's ratio and the Pettifor criterion. The two criteria have undergone numerous revisions, but the core principle of evaluating the brittle-ductile transition has remained unchanged. The bulk-shear modulus ratio is determined by Pugh's ratio: $B/G$. If the ratio is more than 1.75, the material is said to be ductile, and otherwise it is considered brittle[47]. In the Pettifor criterion $C_{12}$ is compared to $C_{44}$: $C_{12} - C_{44}$, where this difference is the Cauchy stress coefficients. A non-metallic system is referred to as ductile when the $C_{12}$-$C_{44}$ >0, and otherwise it is considered brittle[48].The goal of this paper is to integrate the two techniques in order to determine the pressure threshold for the ductile-to-brittle transition in sI methane hydrate.

## 5.5 Results & Discussion

This section will present all the data acquired using the methods described above, as well as discuss their physical significance and contribution. The predictions of various methods are identified by superscripts as defined above. Figure 5-1 shows the organization of the presentation, the flow of information and the connections between results given in the six subsections.

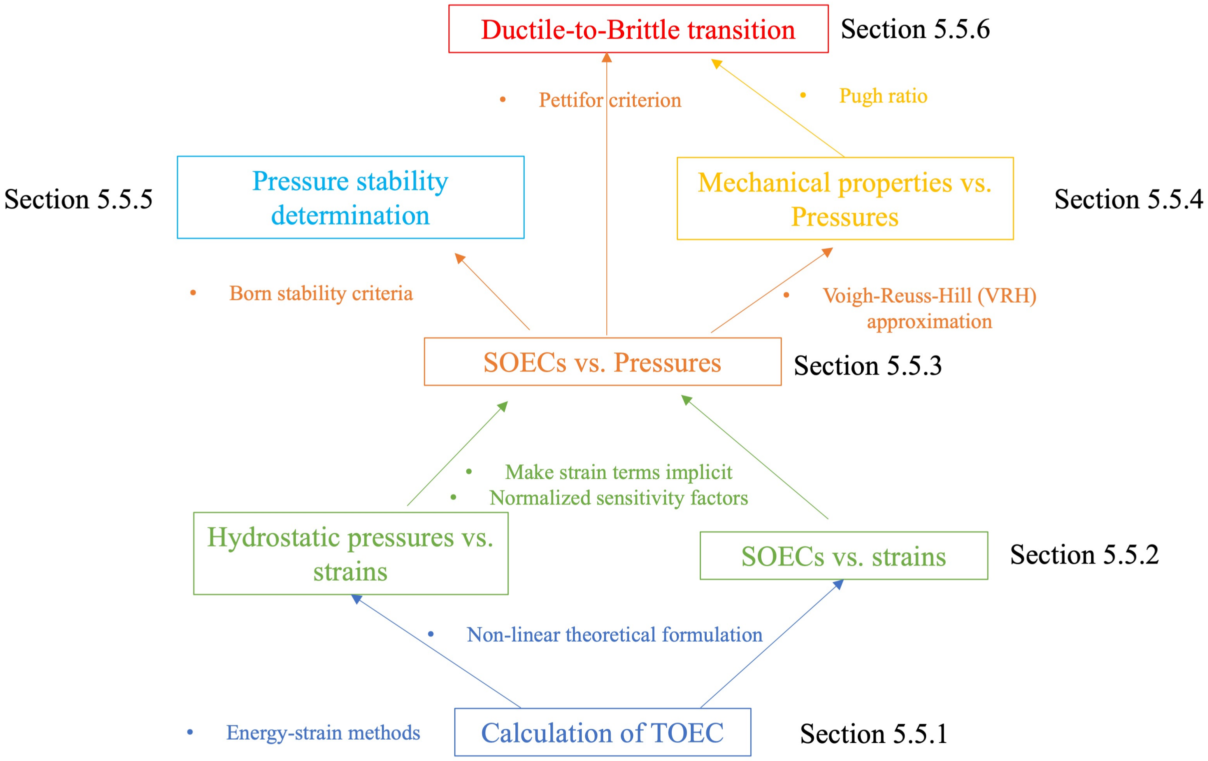

*Figure 5-1. Organization of computational results and flow of information in Section 5.5. The values of SOECs and TOECs for sI methane hydrates, as well as the impacts on SOECs brought on by considering the third order, will be presented in Section 5.5.1. The established relationships between pressure and strains and between SOECs and strains will be shown in Section 5.5.2. Then using strains as the link, we establish the relationship between pressure and SOECs with three different approaches in Section 5.5.3. Once the pressure-constants relationship is established, we use the SOECs under pressures for the further mechanical property's calculations and stability determination in Section 5.5.4 and Section 5.5.5 respectively. Also, by using the calculated mechanical properties, the ductile-to-brittle transition can be determined as shown in Section 5.5.6.*

## 5.5.1 SOECs and TOECs at Zero Pressure

The energy-strain approach is used to determine the SOECs and TOECs of sI methane hydrates with maximum strain changes of ±6%. The coefficients for the quadratic and cubic components are presented in Table 5-2. These coefficients were obtained using six different strain modes (M1-M6). The details on the calculation methods and examples are shown in the SI2. In Table 5-2, all quadratic components were found to be positive ($A_2>0$), while all cubic components were found to be negative ($A_3<0$). Furthermore, $A_3$ appears to be one order of magnitude larger than $A_2$. The difference in sign between $A_2$ and $A_3$ is explained as follows. The physical meaning of ground-state and energy-strain lead to $A_2 >0$. All three degrees of freedom must be relaxed to reach the ground state. Since the lattice volume, shape and atomic positions would be relaxed to their lowest-energy state first. Then the strains are applied to the relaxed system. To evaluate the energy of the strained system, the lattice volume and shape will remain unchanged. Otherwise, the strained system will return to its initial state. As a result, the energy-strain relationship is always concave-up, with minima at zero strain and as a result, $A_2 >0$. On the other hand, $A_3 <0$. The negative cubic components would change the sign of the product of the third-order coefficients and the cubic term . As a result, for positive strains, the estimated energy involving the cubic term will be lower than the model with only quadratic terms, and vice versa. Taking this feature into account, the lattice will attain a local maximum at a particular positive strain and subsequently decline to the lowest-energy state or even lower value, indicating system failure. When considering the negative strain side, when more stresses are applied with a negative third-order coefficient, the energy increases.

This negative sign can also be rationalized by the ductile-to-brittle transition of hydrates. Previous DNS results[14] suggest that the sI methane hydrate displays a brittle behaviour when the tensile forces are applied and becomes ductile when compressive forces are applied. Thus, when the compressive pressures are applied, there would be a plastic region beyond the elastic region. Hence, the energy would accumulate. On the other side, when the tensile pressures are applied, the system would fail after reaching the threshold, which is analogous to the curve with negative coefficients for the cubic terms.

The fact that TOECs have a higher order of magnitude than SOECs can be explained by the additional strain term of the cubic terms. In the selected strain interval (-0.06 to + 0.06) the large magnitude values of $A_3$ can compensate the decreasing effect of strain. As shown in Table 5-2, the $A_3$ values for M2 and M5 are significantly greater than for other $A_3$. M2 and M5 are two strain sets that applied shear strains, which are in diagonal directions. The large values of $A_3$ imply that the nonlinear terms are significant in order to simulate shear deformation and emphasize the necessity of TOEC.

*Table 5-2 Coefficients of the quadratic and cubic terms from Eqn (5.8)*

| | M1 | M2 | M3 | M4 | M5 | M6 |
|---|---|---|---|---|---|---|
| $A_2$ | 20.1758 | 59.0210 | 46.9522 | 46.9522 | 114.2478 | 80.3293 |
| $A_3$ | -715.0942 | -1855.9695 | -755.1979 | -806.5927 | -3315.7932 | -242.5375 |

The exact expressions of $A_2$ and $A_3$ are given in the Section 5.4.1. By using these expressions, the values of three SOECs and six TOECs can be obtained, as presented in Table 5-3. The values of TOECs are negative except for $C_{123}$. This can be contributed to the negativity of $A_3$. Since TOECs have positive correlations with $A_3$, they share the same sign. $C_{123}$ is the only TOEC that has a positive value. This exception has been noticed for other materials as well[2,4,49].

For metals and some carbonates, such as silicon, cadmium carbonate and calcite, $C_{144}$>0[2,4], and for germanium and carbon, $C_{123}$>0[4,49]. The alkali halides, such as LiF and NaI, have three positive TOECs $(C_{123}, C_{456}, C_{144})$ and three negative TOECs $(C_{111}, C_{112}, C_{166})$ under 25 °C [50]. The semiconductor GaAs has a positive value of $C_{144}$ under 25 °C[51]. For other semiconductor, like Ge, under 25 °C, the results obtained from two research groups are different. Bateman, T., et al.[49] showed that $C_{123}$ is a positive value; however, McSkimin, H. J. and P. Andreatch[52] found all TOECs for Ge under 25 °C were negative. The sign difference has been discovered for more than half a decade but does not have a physical explanation. Thus, further investigations on the sign different would be our future work.

*Table 5-3. SOEC and TOEC of sI methane hydrate at zero pressure by NL approach*

<table>
<tr><td rowspan="2">SOEC<br>(GPa)</td><td colspan="2">$C_{11}^{o}$</td><td colspan="2">$C_{12}^{o}$</td><td colspan="2">$C_{44}^{o}$</td></tr>
<tr><td colspan="2">20.1758</td><td colspan="2">8.5721</td><td colspan="2">6.6941</td></tr>
<tr><td rowspan="2">TOEC<br>(GPa)</td><td>$C_{111}^{o}$</td><td>$C_{112}^{o}$</td><td>$C_{123}^{o}$</td><td>$C_{144}^{o}$</td><td>$C_{155}^{o}$</td><td>$C_{456}^{o}$</td></tr>
<tr><td>-715.0942</td><td>-70.9635</td><td>17.8055</td><td>-3.3420</td><td>-7.6249</td><td>-5.0529</td></tr>
</table>

To estimate the effects of TOEC on the prediction of $\mathrm{SOEC}^{\mathrm{NL}}$ under pressure, we compared the results with our previous data[14] of $\mathrm{SOECs}^{\mathrm{DNS}}$. Under 0 K, the sI methane hydrate has the following values for $C_{11}^{oDNS}$, $C_{12}^{oDNS}$, and $C_{44}^{oDNS}$: 17.802 GPa, 7.231 GPa and 6.086 GPa, respectively[14]. The superscript 'oDNS' indicates results obtained at zero pressure by DNS approach. The $\mathrm{SOECs}^{\mathrm{NL}}$ are higher than $\mathrm{SOECs}^{\mathrm{DNS}}$, and the differences range from 10% to 18.55%. This difference can be explained by the presence of TOECs. The negative TOECs will have an opposite effect on the value. Thus, greater SOECs values are required to compensate this effect.

### 5.5.2 Hydrostatic Pressures as a Function of Strains

If the TOECs at zero pressure are known, it is possible to calculate the hydrostatic pressures P surrounding the sI methane hydrates, by imposing a deformed strain $\varepsilon$. Since the elastic constants may characterize the material reaction under a given stress/pressure, the surrounding pressures can be deduced from the TOECs and strains. In this section, three (DNS, L, NL) approaches described in section 5.4.3 are applied to evaluate the hydrostatic pressure with a given deformed strain.

Firstly, the direct numerical simulation (DNS) relaxes the entire system under certain pressure. The strains can be calculated based on the deformed lattice volume and the initial lattice volume. The L and NL methods were shown in Equation (5.4-5.9). The linear fitting used Equation (5.4) but stopped at the first-order of $\varepsilon$ where only SOECs were involved. The nonlinear fitting used the whole Equation (5.9), which contains first- and second-order calculations $(\varepsilon, \varepsilon^2)$ and involves both SOECs and TOECs.

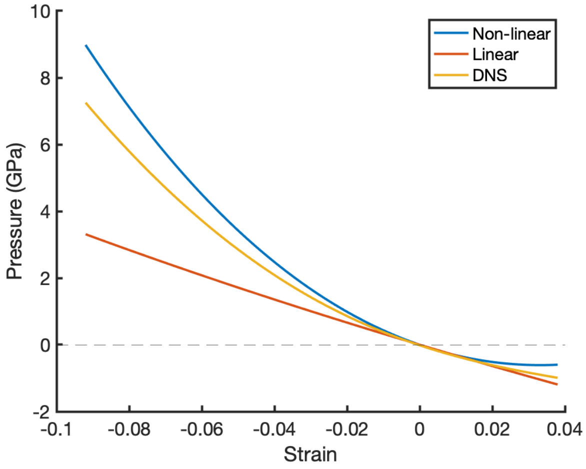

*Figure 5-2 Hydrostatic pressure as a function of strain by three different approaches (DNS, NL, L) with strain ranging from -0.092 to 0.038. Yellow curve represents the DNS result. The blue NL curve shows the non-linear results calculated by using Eqn (5.9). The orange L curve shows the linear fitting approach by using Eqn (5.3a).*

Figure 5-2 presents the (DNS, L, NL) hydrostatic pressures at a given strain. DNS provides the raw simulation data, which can serve as reference. This is because, through DNS approach the lattice was fully relaxed to its lowest-energy state under a given hydrostatic pressure and the relaxed volume was calculated by VASP directly. The deformed strain was calculated as $\left(\frac{V}{V_0}-1\right)^{1/3}$ for the DNS approach. Specifically, the hydrostatic pressure is the input and the deformed strain is the output. However, for the linear model and non-linear model, the deformed strain ε is an input parameter, and the hydrostatic pressure P becomes output, which is opposite from the DNS approach.

Figure 5-2 shows that the linear fitting underestimates the pressures at a specific strain and the nonlinear fitting always overestimates the pressures at a given strain compared with DNS. When the absolute strain values increase, the difference between linear and nonlinear approaches becomes more significant. From the curvature aspect, the nonlinear fitting has a closer nonlinear curvature with the DNS, compared with linear model. The maximum relative difference between the nonlinear and DNS under compressive pressures is 24.55%; however, the maximum relative discrepancy increases to 46.85% between linear and DNS. For the tensile pressures, the maximum relative discrepancy for both linear and nonlinear are approximately 40%. As partial conclusion, if the uniform strains $\varepsilon$ are less than 4%, there is no advantage to use nonlinear fitting for tensile pressure prediction. In other words, linear fitting is preferable under tensile pressure because it requires less computational effort. In the case where the strain is less than 3% under compressive pressure, linear fitting can produce a similar or even better forecast than nonlinear fitting for compressive loading. If the strain exceeds 3%, the nonlinear fitting should be explored for a more accurate pressure forecast. The difference between the linear and nonlinear approaches from the DNS is quantified using root-mean-square deviation estimates. The linear fitting's root-mean-square deviation is 1.25 over the whole strain range, while the nonlinear fitting's is 0.676. These findings strongly suggest that nonlinear fitting can produce a considerably more accurate estimate of hydrostatic pressures, given strain changes, than the linear fitting, especially when the strains are greater than 3%.

## 5.5.3 SOECs under Pressure by Three Characterization Methods

Elastic properties are frequently used to describe how a material behaves under different load conditions. SOECs are widely acknowledged as critical data for estimating other mechanical properties. The results of Section 5.5.2 reveal that TOECs have a substantial advantage when estimating pressures with specified strains. Thus, this section will illustrate how well TOECs evaluate piezo-elastic effects on SOECs.

For the SOECs under pressure, $\mathrm{C}_{11}, \mathrm{C}_{12}$ and $\mathrm{C}_{44}$ can be computed using Equation (5.5-5.7) from linear model or Equation (5.10-5.12) from non-linear model. Engineering sensitivity analysis would be required for the examination of piezo-elastic effects, according to our earlier work[14]. The standard normalized sensitivity factor of response Q to changes in parameter P, using method m is shown below as Equation (5.16)

$$S_Q^m = \frac{P}{Q}\frac{\partial Q}{\partial P}; m = DNS, L, NL \tag{5.16}$$

Here we compute and discuss $S_{C_{11}}^{NL/L/DNS}, S_{C_{12}}^{NL/L/DNS}$ $and$ $S_{C_{44}}^{NL/L/DNS}$

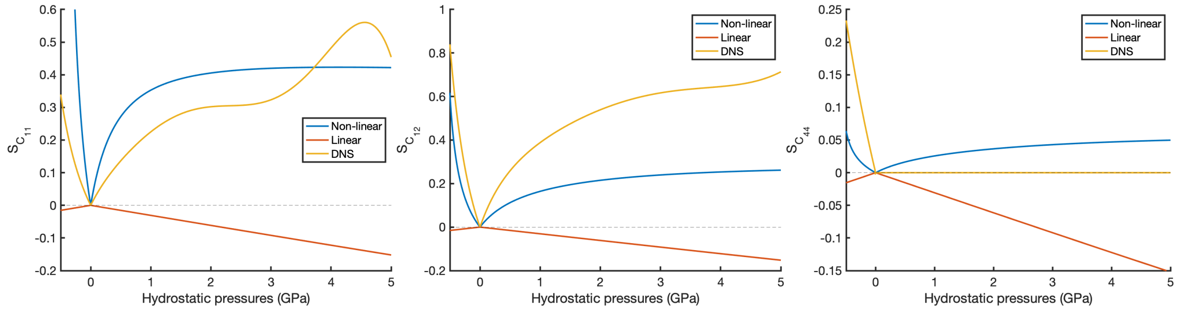

Figure 5-3 Normalized sensitivity factors of $C_{11}$, $C_{12}$ and $C_{44}$ under pressures evaluated by the three different approaches: non-linear model, linear model and direct numerical simulations indicated as blue, orange and yellow curves. The values of $C_{11}$, $C_{12}$ and $C_{44}$ calculated through linear fitting approach by using Eqn (5.5-5.7) and through non-linear fitting approach by using Eqn (5.10-5.12). Then the obtained results were applied into Eqn (5.10) to calculate their corresponding sensitivity factors; equations are shown in Section 1. The predictions from the linear model deviated sharply from DNS and NL.

Figure 5-3, shows the three normalized sensitivity factors, $S_{C_{11}}^{NL/L/DNS}$ (left), $S_{C_{12}}^{NL/L/DNS}$(middle) and $S_{C_{44}}^{NL/L/DNS}$(right) at hydrostatic pressures ranging from -0.5 to 5 GPa. The blue, orange and yellow curves represent the non-linear fitting, linear fitting and direct numerical simulation approaches, respectively.

The DNS curve is used as the reference to evaluate linear and non-linear models' reliability on predicting the SOECs' piezo-sensitivity. Focusing on the curvatures of these factors, the non-linear fitting share similar curvature on all three normalized sensitivity factors under both tensile and compressive pressures. Besides $S_{C_{44}}$, both non-linear fitting and direct numerical simulation demonstrate that $S_{C_{11/12}}^{NL/DNS}$ have an increasing trend once either tensile or compressive pressure was applied. The values of $S_{C_{11/12}}^{NL/DNS}$ are always positive. From the magnitude aspect, there are some discrepancies between the $S_{C_{11/12}}^{NL}$and $S_{C_{11/12}}^{DNS}$. For $S_{C_{11}}$, it seems that the $S_{C_{11}}^{NL}$ always have a greater value than the $S_{C_{11}}^{DNS}$ from -0.5 GPa to 3.5 GPa. Between 3.5 GPa and 5 GPa, there are some fluctuations in $S_{C_{11}}^{DNS}$, but the values of $S_{C_{11}}^{DNS}$ and $S_{C_{11}}^{NL}$ at 5 GPa are sufficiently close. From the continuous value evolving aspect, the $S_{C_{11}}^{NL}$ trend and curvature is more reasonable and acceptable. For $S_{C_{12}}$, $S_{C_{12}}^{NL}$ shows a smaller value than $S_{C_{12}}^{DNS}$ under pressures. The values under tensile pressures are close; however, a greater discrepancy is observed on the compressive side as the compressive pressure increases.

For $S_{C_{44}}$, the DNS approach are based on the raw data $C_{44}$ with fluctuations around 7.2957 GPa under compressive pressures; the particular computational issues and existing data for gas hydrates for $C_{44}$ was previously discussed[14]. Thus, it was assumed that $C_{44}$ is not subject to compressive pressures and thus the $S_{C_{44}}^{DNS}$ is zero. However, it might not be the fact. $S_{C_{44}}^{NL}$ increase from 0 to 0.058 under pressures ranging from 0 GPa to 5 GPa. This would be more reasonable and acceptable than $S_{C_{44}}^{DNS}$ from the physical aspect. This is because, firstly from the curvature aspect, the positive $S_{C_{44}}^{NL}$ under compressive pressures have a similar behavior with $S_{C_{11/12}}^{NL/DNS}$. Secondly, the $S_{C_{44}}^{NL}$ has a constant value of 0.058 from 1 GPa to 5 GPa, which is very close to the value of $S_{C_{44}}^{DNS} = 0$. Thus, from both curvature and magnitude aspects, the predictions of $S_{C_{44}}^{NL}$ are more reasonable than $S_{C_{44}}^{DNS}$.

To consider the behavior of $S_{C_{11/12/44}}^{L}$, due to the linear feature of linear fitting, the $S_{C_{11/12/44}}^{L}$ showed straight lines along with pressures. From either curvature or magnitude aspects, linear fitting could not provide a good prediction of the normalized pressure sensitivity factor. Firstly, the non-linear part could not be captured by the linear fitting. Secondly, the values of $S_{C_{11/12/44}}^{NL/DNS}$ are always positive; however, $S_{C_{11/12/44}}^{L}$ has negative values along with pressures. This indicates that linear fitting is a poor tool on estimating the piezo-effects on SOECs. On the other hand, the non-linear fitting gives a very good estimation in terms of magnitude and curvature aspect.

## 5.5.4 Mechanical Properties under Pressure

SOECs are always served as the fundamental parameters for mechanical properties' calculations. Thus, the SOECs values under pressure become rather important on the evaluations on the mechanical properties under load. In this section, four parameters are selected to characterize for the comparisons among three approaches. All mechanical properties in terms of pressures are summarized in terms of normalized sensitivity factors. The Voigt-Reuss approximation equations used to calculate the mechanical properties are shown in the SI4.

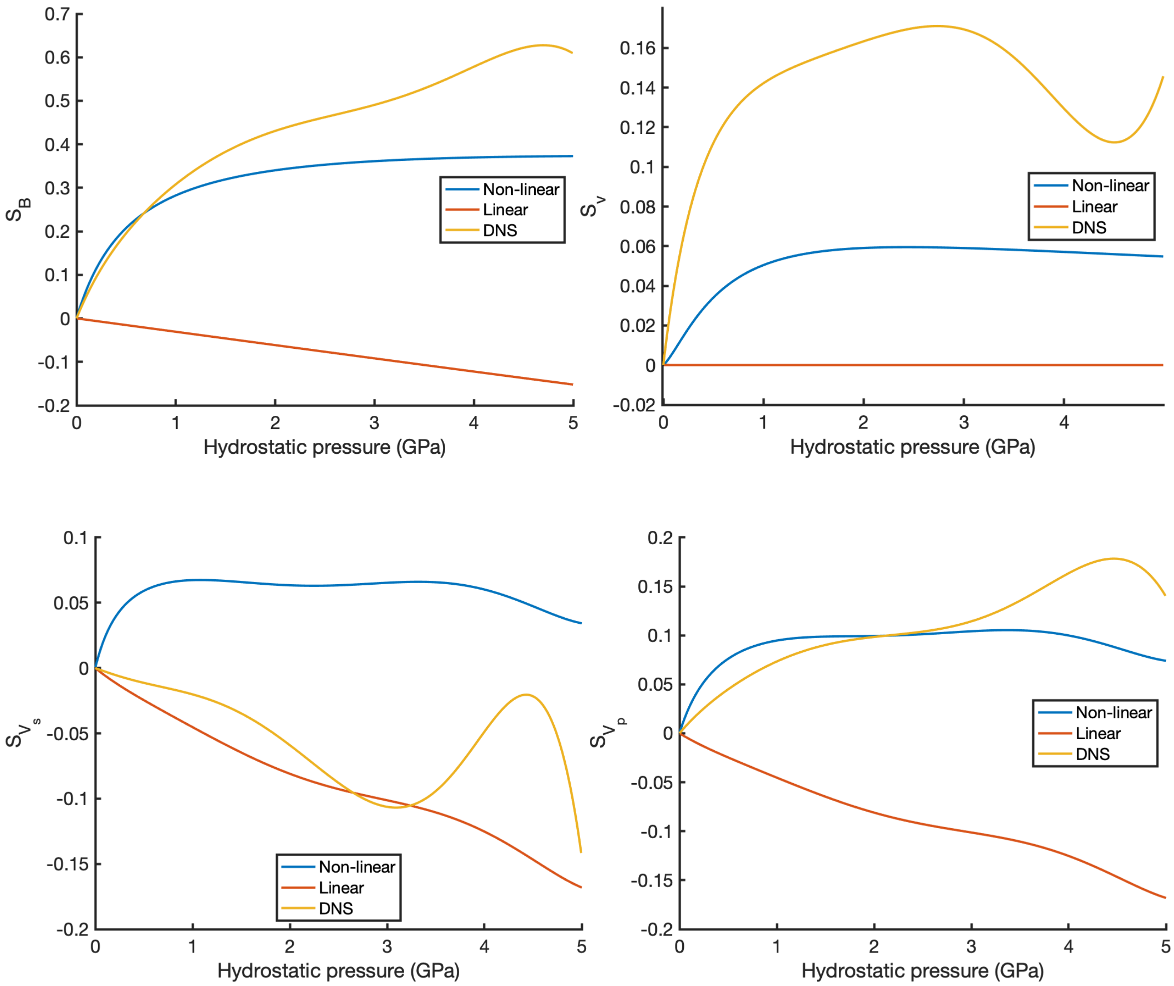

*Figure 5-4 Normalized sensitivity factors of mechanical properties under pressures, from 0 GPa to 5 GPa. (Top left) Bulk modulus [Eqn (5.S8) in SI4]. (Top right) Poisson ratio [Eqn (5.S9) in SI4]. (Bottom left) Transverse wave speed [Eqn (5.S12) in SI4]. (Bottom right) Longitudinal wave speed [Eqn (5.S11) in SI4]. The results obtained through non-linear, linear and DNS approaches are shown in blue, orange and yellow curves respectively. The non-linear fitting used Eqn (5.10-5.12) to obtain the*

*values of $C_{11}, C_{12}$ and $C_{44}$, and then applied in the corresponding equations shown in SI4. Then the parameter values under pressure will are applied through Eqn (5.10) in Section 5.4 to get their sensitivity factors. The linear fitting approach used the same methodology but used Eqn (5.5-5.7) to obtain the values of $C_{11}, C_{12}$ and $C_{44}$. The results show that the NL model predictions are consistent with DNS except for the transverse wave speed.*

Figure 5-4 shows the normalized sensitivity factors values of bulk modulus (B), Poisson ratio (v), transverse wave speed ($V_s$), and longitudinal wave speed ($V_p$). The blue/orange/yellow curves stand for non-linear, linear and DNS respectively.

For $S_B$, both $S_B^{NL}$ and $S_B^{DNS}$show positive values under compressive pressures and values are very close to each other when the pressure is lower than 1 GPa. The average absolute difference between $S_B^{NL}$ and $S_B^{DNS}$ is only 0.0078 when pressure is lower than 1 GPa. Although, at 5 GPa, the value of $S_B^{DNS}$ is twice of the $S_B^{NL}$, $S_B^{NL}$ is still able to capture the general tendency. On the other hand, $S_B^{L}$ shows a negative value under compressive pressures. From both curvature and magnitude aspects, the non-linear fitting shows higher accuracy than the linear fitting.

For $S_v$, both $S_v^{NL}$and $S_v^{DNS}$ show positive values under pressure, but $S_v^{L}$ is equal to 0, which indicates the Poisson ratio by linear fitting approach is a constant value under pressure. Although the magnitude of both $S_v^{NL}$and $S_v^{DNS}$ are very small, the maximum discrepancy from 0 GPa to 5 GPa in $S_v^{DNS}$ is 2.5 times greater than $S_v^{NL}$ at 3 GPa. Since $S_v^{DNS}$ shows an increasing trend with some fluctuations, $S_v^{NL}$ showed a similar tendency smooth curvature, we can conclude that $S_v^{NL}$ has a better performance on the prediction of the Poisson ratio change under pressures, than $S_v^{L}$.

Transverse wave speed and longitudinal wave speed are the two most essential parameter to show the importance of TOECs. In Figure 5-4, the bottom left panel is the sensitivity factor of transverse wave speed, and the bottom right panel is the sensitivity factor of the longitudinal wave speed. They showed that the non-linear fitting could give a close result with DNS for the longitudinal wave speed in terms of the sensitivity factor. However, for the transverse wave speed, the results between linear fitting and DNS are closer. Both wave speeds, $S^{L}_{V_p/V_s}$ show a decreasing trend under compressive pressures. $S^{NL}_{V_p/V_s}$, however; showed an increasing trend initially and converged to a constant value after 1 GPa. From these results it can be concluded that TOECs has an advantage in predicting the longitudinal wave speed. For the transverse wave speed, more studies need to be performed to rationalize the presented differences.

### 5.5.5 Born Stability Criteria

The most common material criterion for evaluating a system's stability under pressure are Born stability criteria. To access different features of pressures, such as shear stress and tensile stress, three criteria are used. The criteria have evolved into many versions over time, but the essential notion remains the same. The details are shown in Equation (5.13-5.15).

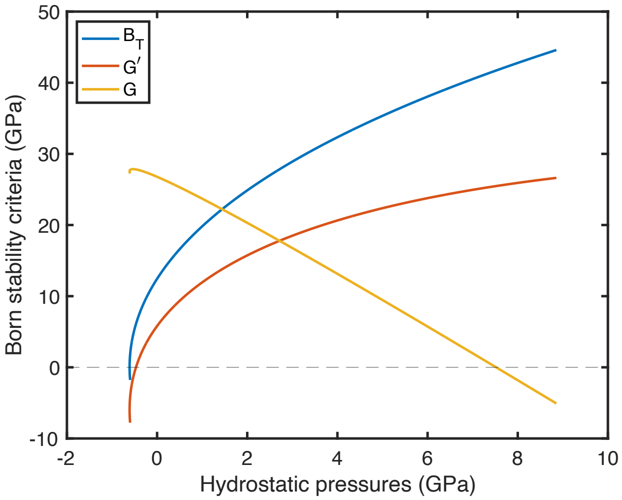

*Figure 5-5 Born stability criteria. The blue, orange and yellow curves represent the results obtained for Eqn (5.13-5.15) respectively. The grey dashed line is the threshold line at zero. Stability is lost if any of the criteria is negative.*

Based on Equation (5.13-5.15), Figure 5-5 depicts the values of assessed terms as well as pressures. Equation (5.13) relates to the blue curve, which shows the bulk stiffness resistance ability. It evaluates the material's total resistance to external loads in all directions. Equation (5.14), shown as a red curve, is mostly used to analyze the term $C_{11}$-$C_{12}$, which is a different shear stress than $C_{44}$. The shear stress term $C_{44}$ is calculated using Equation (5.15), shown as a yellow curve. Because Equation (5.15) is the only one that cannot hold a value greater than zero under compressive forces, the $C_{44}$ plays a substantial role under compressive pressures, as seen in Figure 5-5. It crosses the dashed grey line (y=0) at 7.8 GPa. This indicates that the compressive stability limits of the system have been reached. On the tensile side, there was a competition between the $C_{11}$ and the $C_{11}$-$C_{12}$. Furthermore, the pressures at the places where they cross the barrier are around -0.5 GPa. These phenomena, on the other hand, differs from previous observations. We previously established that the terms $C_{11}$-$C_{12}$ had a considerable impact on both compressive and tensile stresses[14]. In the previous study, a decreasing trend of $C_{11}$ was predicted under high compressive pressures and the values of $C_{12}$ were larger than $C_{11}$ leading the term $C_{11}$-$C_{12}$ to cross the grey dashed line on the compressive side.

To conclude, the Born stability criteria with SOECs evaluated from the non-linear method show that the compressive and tensile limits are 7.5 GPa and -0.5 GPa, respectively. Compared with the data from DNS, the non-linear fitting results show the same prediction on the compressive limits, both being 7.5 GPa. For the tensile limit, there is a small discrepancy between DNS and non-linear model. The tensile pressure limit from the DNS approach is -1 GPa[14], while the value from the non-linear model is -0.5 GPa. Nevertheless, the two tensile limits are of the same magnitude.

### 5.5.6 Ductile-to-Brittle Transition

To examine the fracture mechanisms of a material, it is necessary to understand the ductile or brittle properties. Two commonly used criteria are presented in this section: the Pugh ratio and Pettifor criterion. The SOECs obtained from the non-linear approach was used to determine the necessary quantities including the bulk modulus, shear modulus. To investigate the significance of non-linear fitting, we compared the results with the results from DNS approach from previous work.

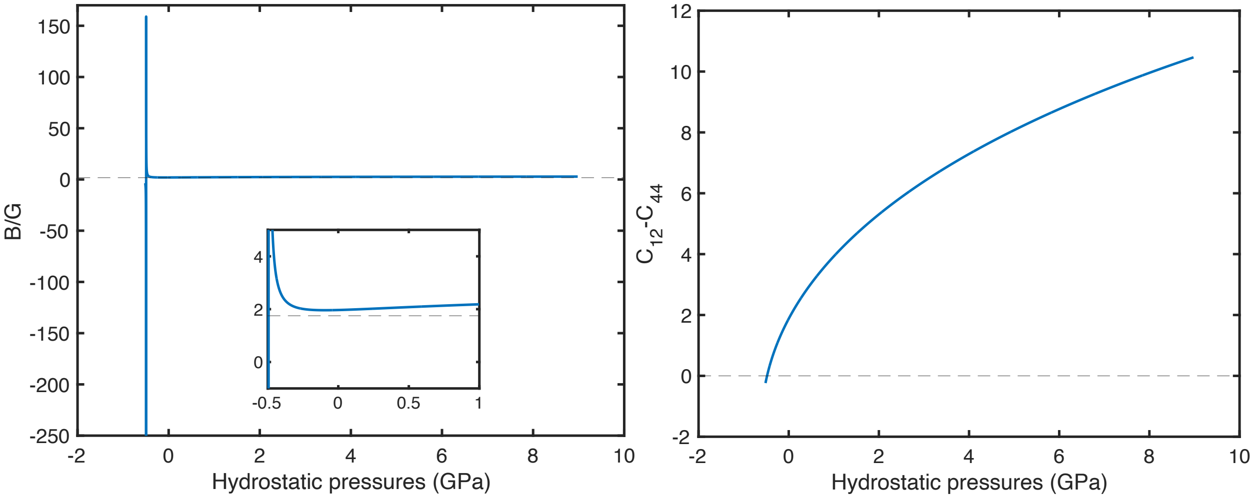

*Figure 5-6 (Left) Pugh ratio evaluated by the ratio of B/G (Right) Pettifor criterion evaluated by the difference of $C_{12}$-$C_{44}$ under pressures. The transition threshold of Pugh ratio and Pettifor criterion are 1.75 and 0, respectively (shown as grey dashed lines). If the value is above the threshold, then it is recognized as ductile and vice versa.*

The Pugh ratio and Pettifor criterion are used to assess the ductile-to-brittle transition in Figure 5-6. The ductile-to-brittle transition threshold of Pugh ratio and Pettifor criterion are 1.75 and 0, respectively, which are shown as grey dashed lines in Figure 5-6. If the assessed terms are greater than the threshold value, the material is considered as ductile, and vice versa. Specifically, if the B/G value is greater than 1.75 or the $C_{12}$-$C_{44}$ value is greater than 0, the material can be recognized as ductile material. The insert of Figure 5-6 (left) shows that the B/G value has an increasing tendency under compressive pressures and is always above the grey dashed lines. Even though the tendency and assessed term values differ between the two criteria, sI methane hydrate exhibits ductile-to-brittle transition at similar pressures. Pugh's and Pettifor's ductile-to-brittle transition threshold pressures are -0.4941GPa and -0.4806GPa, respectively. Although there is a minor difference between the two criteria, it is small enough to be considered acceptable. In comparison to prior findings[14], which showed a ductile feature under compressive pressures and a brittle feature under tensile stresses, The SOECs values under pressure from the non-linear model reflect not only general pattern and but also provide more quantitative results.

We can conclude that sI methane hydrate would be ductile under compressive forces based on this solid quantitative data. The ductile-to-brittle transition occurs under tensile pressures in the low-pressure zone, and brittle behaviour occurs when the pressure reaches -0.5 GPa.

## 5.6 Conclusions

This paper’s objective is to characterize the elasticity of monocrystal ideal methane sI gas hydrate under pressure using linear and nonlinear models; the scope, assumptions and restrictions are specified in the introduction and emphasized throughout the paper. First, we calculated the SOECs and TOECs values at zero pressure, at zero Kelvin for sI methane hydrate through three approaches. The results show that the differences of SOECs are between 10% and 18.55%. Secondly, we investigate the relationship between the TOECs and the SOECs under pressure. The results show that the non-linear model involving the TOECs gives a closer prediction of the DNS results between the pressures and strains than the linear model. In addition, SOECs under pressure from non-linear models in terms of normalized sensitivity factors have revealed smoother shifting patterns. The mechanical properties, e.g., bulk modulus, shear modulus, Young's modulus, and Poisson ratio, in terms of pressure, were calculated based on the SOECs from the non-linear model. The prediction of the sensitivity factor from the non-linear model can be only 0.0078 from the DNS approach.  Born Stability criteria are utilised to assess the hydrate's structure stability by using SOECs under pressures from the non-linear model. It shows that the compressive and tensile limits are 7.5 GPa and -0.5 GPa from the non-linear model, which is consistent with previous work. The results are satisfactory and can provide reliable information about the pressure stability limitations. The ductile-to-brittle transition was determined using Pugh's ratio and the Pettiford criterion. The resultant transitions, at approximately -0.5 GPa, are remarkably similar across the two techniques.

The significance and contribution of TOECs can be highlighted with these excellent outcomes. Instead of simulating each pressure to determine how it affects the attributes, TOECs at zero pressure could provide all the information needed for the prediction of SOECs under pressure. Since the mechanical properties, stability determinations and ductile-to-brittle transitions are all based on the SOECs values under corresponding conditions, the ability of TOECs on the evaluation of piezo-effect on SOECs would significantly save simulation and time costs in piezo-effects research. It is noteworthy that all the findings presented here are transferable and can be applied to other hydrogen-bonded lattice structure systems.

## 5.7 Acknowledgments

This work was supported by Compute Canada and Calcul Québec. A.D.R. and P.S. are thankful for the Natural Sciences and Engineering Council of Canada (NSERC) for funding through the Discovery Grant Program. A.D.R. is thankful for the James McGill Professorship appointment funding, McGill University. X.Z. is thankful for the support through the McGill Engineering Doctoral Awards (MEDA), the Graduate Excellence Award, and the McConnell Memorial Fellowship Award of the Chemical Engineering department, McGill University. A.G. is thankful for the NSERC Canada Graduate Scholarship-Doctoral (CGS-D) award.

# 5.8 Reference

1 Luo, C., Tromp, J. & Wentzcovitch, R. M. Ab initio calculations of third-order elastic coefficients. *arXiv preprint arXiv:2204.07608* (2022).

2 Kaga, H. Third-Order Elastic Constants of Calcite. *Physical Review* **172**, 900-919, doi:10.1103/physrev.172.900 (1968).

3 Wang, X., Gu, Y., Sun, X., Wang, H. & Zhang, Y. Third-order elastic constants of ZnO and size effect in ZnO nanowires. *Journal of Applied Physics* **115**, 213516, doi:10.1063/1.4881775 (2014).

4 Liao, M. *et al.* Elastic3rd: A tool for calculating third-order elastic constants from first-principles calculations. *Computer Physics Communications* **261**, 107777, doi:https://doi.org/10.1016/j.cpc.2020.107777 (2021).

5 De Jong, M., Winter, I., Chrzan, D. C. & Asta, M. Ideal strength and ductility in metals from second- and third-order elastic constants. *Physical Review B* **96**, doi:10.1103/physrevb.96.014105 (2017).

6 Guerra, A., Mathews, S., Marić, M., Rey, A. D. & Servio, P. An Integrated Experimental and Computational Platform to Explore Gas Hydrate Promotion, Inhibition, Rheology, and Mechanical Properties at McGill University: A Review. *Energies* **15**, 5532 (2022).

7 Mirzaeifard, S., Servio, P. & Rey, A. D. Molecular Dynamics Characterization of Temperature and Pressure Effects on the Water-Methane Interface. *Colloid and Interface Science Communications* **24**, 75-81, doi:https://doi.org/10.1016/j.colcom.2018.04.004 (2018).

8 Mirzaeifard, S., Servio, P. & Rey, A. D. Multiscale Modeling and Simulation of Water and Methane Hydrate Crystal Interface. *Crystal Growth & Design* **19**, 5142-5151, doi:10.1021/acs.cgd.9b00578 (2019).

9 Guerra, A., Mathews, S., Marić, M., Servio, P. & Rey, A. D. All-Atom Molecular Dynamics of Pure Water&ndash;Methane Gas Hydrate Systems under Pre-Nucleation Conditions: A Direct Comparison between Experiments and Simulations of Transport Properties for the Tip4p/Ice Water Model. *Molecules* **27**, 5019 (2022).

10 Vlasic, T. M., Servio, P. & Rey, A. D. Atomistic modeling of structure II gas hydrate mechanics: Compressibility and equations of state. *AIP Advances* **6**, 085317, doi:10.1063/1.4961728 (2016).

11 Vlasic, T. M., Servio, P. D. & Rey, A. D. Effect of Guest Size on the Mechanical Properties and Molecular Structure of Gas Hydrates from First-Principles. *Crystal Growth & Design* **17**, 6407-6416, doi:10.1021/acs.cgd.7b01072 (2017).

12 Vlasic, T. M., Servio, P. D. & Rey, A. D. THF hydrates as model systems for natural gas hydrates: comparing their mechanical and vibrational properties. *Industrial & Engineering Chemistry Research* **58**, 16588-16596 (2019).

13 Daghash, S. M., Servio, P. & Rey, A. D. From Infrared Spectra to Macroscopic Mechanical Properties of sH Gas Hydrates through Atomistic Calculations. *Molecules* **25**, doi:10.3390/molecules25235568 (2020).

14 Zhu, X., Rey, A. D. & Servio, P. Piezo-Elasticity and Stability Limits of Monocrystal Methane Gas Hydrates: Atomistic-Continuum Characterization. *The Canadian Journal of Chemical Engineering* **n/a**, doi:https://doi.org/10.1002/cjce.24433 (2022).

15 Zhu, X., Rey, A. D. & Servio, P. Multiscale Piezoelasticity of Methane Gas Hydrates: From Bonds to Cages to Lattices. *Energy & Fuels*, doi:10.1021/acs.energyfuels.2c01024 (2022).

16 Ruppel, C. D. Methane Hydrates and Contemporary Climate Change. *Nature Education Knowledge 3(10):29* (2011).

17 Sloan Jr., E., Koh, C., Koh, C. . Clathrate Hydrates of Natural Gases., 752 pages (2007).

18 National Research, C. *et al. Charting the Future of Methane Hydrate Research in the United States*. (National Academies Press, 2004).

19 Council of Canadian Academies. Expert Panel on Gas, H. (Council of Canadian Academies = Conseil des académies canadiennes, Ottawa, 2008).

20 Yu, Y.-S., Zhang, X., Liu, J.-W., Lee, Y. & Li, X.-S. Natural gas hydrate resources and hydrate technologies: a review and analysis of the associated energy and global warming challenges. *Energy & Environmental Science* **14**, 5611-5668, doi:10.1039/d1ee02093e (2021).

21 Daghash, S., Servio, P. & Rey, A. First-Principles Elastic and Anisotropic Characteristics of Structure-H Gas Hydrate under Pressure. *Crystals* **11**, 477, doi:10.3390/cryst11050477 (2021).

22 Daghash, S. M., Servio, P. & Rey, A. D. From Infrared Spectra to Macroscopic Mechanical Properties of sH Gas Hydrates through Atomistic Calculations. *Molecules* **25**, 5568, doi:10.3390/molecules25235568 (2020).

23 Mathews, S. L., Servio, P. D. & Rey, A. D. Heat Capacity, Thermal Expansion Coefficient, and Grüneisen Parameter of CH<sub>4</sub>, CO<sub>2</sub>, and C<sub>2</sub>H<sub>6</sub> Hydrates and Ice I<sub>h</sub> via Density Functional Theory and Phonon Calculations. *Crystal Growth &amp; Design* **20**, 5947-5955, doi:10.1021/acs.cgd.0c00630 (2020).

24 Jendi, Z. M., Servio, P. & Rey, A. D. Ideal Strength of Methane Hydrate and Ice Ih from First-Principles. *Crystal Growth & Design* **15**, 5301-5309, doi:10.1021/acs.cgd.5b00829 (2015).

25 Jia, J., Liang, Y., Tsuji, T., Murata, S. & Matsuoka, T. Elasticity and Stability of Clathrate Hydrate: Role of Guest Molecule Motions. *Scientific Reports* **7**, doi:10.1038/s41598-017-01369-0 (2017).

26 Guerra, A. *et al.* Dynamic viscosity of methane and carbon dioxide hydrate systems from pure water at high-pressure driving forces. *Chemical Engineering Science* **252**, 117282, doi:https://doi.org/10.1016/j.ces.2021.117282 (2022).

27 Barron, T. H. K. & Klein, M. L. Second-order elastic constants of a solid under stress. *Proceedings of the Physical Society* **85**, 523-532, doi:10.1088/0370-1328/85/3/313 (1965).

28 Mehl, M. J., Osburn, J. E., Papaconstantopoulos, D. A. & Klein, B. M. Structural properties of ordered high-melting-temperature intermetallic alloys from first-principles total-energy calculations. *Physical Review, B: Condensed Matter; (USA)* **41**, 10311-10323, doi:10.1103/PhysRevB.41.10311 (1990).

29 Wang, S. Q. & Ye, H. Q. First-principles study on elastic properties and phase stability of III-V compounds. *physica status solidi (b)* **240**, 45-54, doi:10.1002/pssb.200301861 (2003).

30 Zhao, J., Winey, J. M. & Gupta, Y. M. First-principles calculations of second- and third-order elastic constants for single crystals of arbitrary symmetry. *Physical Review B* **75**, 094105, doi:10.1103/PhysRevB.75.094105 (2007).

31 Jendi, Z. M., Rey, A. D. & Servio, P. Ab initioDFT study of structural and mechanical properties of methane and carbon dioxide hydrates. *Molecular Simulation* **41**, 572-579, doi:10.1080/08927022.2014.899698 (2015).

32 Zhao, J., Winey, J. M. & Gupta, Y. M. First-principles calculations of second- and third-order elastic constants for single crystals of arbitrary symmetry. *Physical Review B* **75**, doi:10.1103/PhysRevB.75.094105 (2007).

33 Marmier, A. *et al.* ElAM: A computer program for the analysis and representation of anisotropic elastic properties. *Computer Physics Communications* **181**, 2102-2115, doi:https://doi.org/10.1016/j.cpc.2010.08.033 (2010).

34 Brugger, K. Pure Modes for Elastic Waves in Crystals. *Journal of Applied Physics* **36**, 759-768, doi:10.1063/1.1714215 (1965).

35 Georg Kresse, M. M., ,J¨urgen Furthm¨uller. (2018).

36 Takeuchi, F. *et al.* Water proton configurations in structures I, II, and H clathrate hydrate unit cells. *The Journal of chemical physics* **138**, 124504 (2013).

37 Bernal, J. D. & Fowler, R. H. A Theory of Water and Ionic Solution, with Particular Reference to Hydrogen and Hydroxyl Ions. *The Journal of Chemical Physics* **1**, 515-548, doi:10.1063/1.1749327 (1933).

38 Daghash, S. M., Servio, P. & Rey, A. D. Structural properties of sH hydrate: a DFT study of anisotropy and equation of state. *Molecular Simulation* **45**, 1524-1537 (2019).

39 Jendi, Z. M. *Multiscale modelling of gas hydrate mechanical and thermal properties*. (McGill University (Canada), 2016).

40 Blöchl, P. E. Projector augmented-wave method. *Physical review B* **50**, 17953 (1994).

41 Kresse, G. & Joubert, D. From ultrasoft pseudopotentials to the projector augmented-wave method. *Physical review b* **59**, 1758 (1999).

42 Wang, H. & Li, M. Nonlinear theoretical formulation of elastic stability criterion of crystal solids. *Physical Review B* **85**, 104103, doi:10.1103/PhysRevB.85.104103 (2012).

43 Born, M. Thermodynamics of Crystals and Melting. *The Journal of Chemical Physics* **7**, 591-603, doi:10.1063/1.1750497 (1939).

44 Mouhat, F. & Coudert, F.-X. Necessary and sufficient elastic stability conditions in various crystal systems. *Physical Review B* **90**, doi:10.1103/physrevb.90.224104 (2014).

45 Sin$rquot$ko, G. V. & Smirnov, N. A. Ab initio calculations of elastic constants and thermodynamic properties of bcc, fcc, and hcp Al crystals under pressure. *Journal of Physics: Condensed Matter* **14**, 6989-7005, doi:10.1088/0953-8984/14/29/301 (2002).

46 Wang, H. & Li, M. The elastic stability, bifurcation and ideal strength of gold under hydrostatic stress: an ab initio calculation. *Journal of Physics: Condensed Matter* **21**, 455401, doi:10.1088/0953-8984/21/45/455401 (2009).

47 Liu, Y. *et al.* Theoretical study of the mechanical properties of CrFeCoNiMo<sub>x</sub> (0.1 ≤ <i>x</i> ≤ 0.3) alloys. *RSC Advances* **10**, 14080-14088, doi:10.1039/d0ra00111b (2020).

48 Senkov, O. N. & Miracle, D. B. Generalization of intrinsic ductile-to-brittle criteria by Pugh and Pettifor for materials with a cubic crystal structure. *Scientific Reports* **11**, doi:10.1038/s41598-021-83953-z (2021).

49 Bateman, T., Mason, W. P. & McSkimin, H. J. Third-Order Elastic Moduli of Germanium. *Journal of Applied Physics* **32**, 928-936, doi:10.1063/1.1736135 (1961).

50 Ghate, P. B. Third-Order Elastic Constants of Alkali Halide Crystals. *Physical Review* **139**, A1666-A1674, doi:10.1103/PhysRev.139.A1666 (1965).

51 McSkimin, H. J. & Jr., P. A. Third-Order Elastic Moduli of Gallium Arsenide. *Journal of Applied Physics* **38**, 2610-2611, doi:10.1063/1.1709955 (1967).

52 McSkimin, H. J. & Andreatch, P. Measurement of Third-Order Moduli of Silicon and Germanium. *Journal of Applied Physics* **35**, 3312-3319, doi:10.1063/1.1713214 (1964).

53 Bentahar, M., Brahim, R., Benchaala, A. & Brahim, R. in *Proceedings, World Conference on Nondestructive Testing: Material Characterization and Testing, 15th, Roma, Italy, October.* 15-21.

54 Lazar, M., Agiasofitou, E. & Böhlke, T. Mathematical modeling of the elastic properties of cubic crystals at small scales based on the Toupin–Mindlin anisotropic first strain gradient elasticity. *Continuum Mechanics and Thermodynamics* **34**, 107-136, doi:10.1007/s00161-021-01050-y (2022).

# 5.9 Supplementary Information (SI)

## 5.9.1 SOECs and TOECs definition (SI1)

This Supporting Information (SI1) provides the fundamental definitions of SOECs and TOECs.

Second order elastic constant (SOECs) are determined with the linear elastic theory while the third order constants required the use of the acoustoelastic theory[53]. The SOECs can be expressed as the fourth-rank constitutive tensor $C_{ijkl}$, because the stress and strain can be expressed as second-rank tensors, such as $\sigma_{ij}$, or $\varepsilon_{kl}$, and thus the second order elastic constants would be fourth-rank. To simplify the expression, using the Voigt notation, for cubic crystals is contracted to the symmetric $6 \times 6$ matrix, $C_{\alpha\beta}, \alpha, \beta = 1, \cdots, 6$ in a reference system whose axes coincide with the axes of the cubic crystal[54], as shown below.

$$C_{\alpha\beta} = \begin{pmatrix} C_{11} & C_{12} & C_{12} & 0 & 0 & 0 \\ C_{12} & C_{11} & C_{12} & 0 & 0 & 0 \\ C_{12} & C_{12} & C_{11} & 0 & 0 & 0 \\ 0 & 0 & 0 & C_{44} & 0 & 0 \\ 0 & 0 & 0 & 0 & C_{44} & 0 \\ 0 & 0 & 0 & 0 & 0 & C_{44} \end{pmatrix}$$

For cubic crystals, there are only six elastic constants: $C_{111}$, $C_{112}$, $C_{123}$, $C_{144}$, $C_{155}$ and $C_{456}$. Here we show how to obtain these constants using a reduction procedure starting from the most general case. The third-order elastic constants can be shown in the form of $C_{ijklmn}$, which is a sixth-order tensor containing 729 ($3^6$) components. When using the Voigt notation, it is simplified to a 6-dimensional vector. There are only 216 ($6^3$) components. The matrices look very close to the second-order matrix as shown above. Thus, there are six $6 \times 6$ matrices, shown as step 1; see below. Based on the elastic matrix symmetry, the upper and lower triangles in the matrix are the same, and we thus keep the upper triangle for the following calculations. So, in the first row, from step 1 to step 2, the matrix remains as 6 × 6, but only the upper triangle is kept. For the second row, from step 1 to step 2, the matrix size changes from 6 × 6 to 5 × 5. This is because the first row and first column have been included in the last row matrix (first row, step 2 matrix). The same methodology will be used for the following rows. Thus, the matrix in step 2 reduces its dimensionality but retains their square feature. From step 2 to step 3, the simplification or reduction is based on the cubic crystal features. Some values do not exist, so they are indicated as '0'. Some others will be replaced by other symbols due to equivalence. At the end only six components are left: $C_{111}$, $C_{112}$, $C_{123}$, $C_{144}$, $C_{155}$ and $C_{456}$. The equivalences among TOECs are shown in Table 5-4. The first column shows the symbols for the third-order elastic constants and the second column is their equivalence.

*Table 5-4 Third order elastic constants equivalence due to cubic symmetry*

| | |
|---|---|
| 111 | 222/333 |
| 112 | 113/122/133/223/233 |
| 123 | N/A |
| 144 | 255/366 |
| 155 | 166/244/266/344/355 |
| 456 | N/A |

Step 1 Step 2 Step 3

$$\begin{bmatrix} 111 & 112 & 113 & 114 & 115 & 116 \\ 121 & 122 & 123 & 124 & 125 & 126 \\ 131 & 132 & 133 & 134 & 135 & 136 \\ 141 & 142 & 143 & 144 & 145 & 146 \\ 151 & 152 & 153 & 154 & 155 & 156 \\ 161 & 162 & 163 & 164 & 165 & 166 \end{bmatrix} \rightarrow \begin{bmatrix} 111 & 112 & 113 & 114 & 115 & 116 \\ 0 & 122 & 123 & 124 & 125 & 126 \\ 0 & 0 & 133 & 134 & 135 & 136 \\ 0 & 0 & 0 & 144 & 145 & 146 \\ 0 & 0 & 0 & 0 & 155 & 156 \\ 0 & 0 & 0 & 0 & 0 & 166 \end{bmatrix} \rightarrow \begin{bmatrix} 111 & 112 & 112 & 0 & 0 & 0 \\ 0 & 112 & 123 & 0 & 0 & 0 \\ 0 & 0 & 112 & 0 & 0 & 0 \\ 0 & 0 & 0 & 144 & 0 & 0 \\ 0 & 0 & 0 & 0 & 155 & 0 \\ 0 & 0 & 0 & 0 & 0 & 155 \end{bmatrix}$$

$$\begin{bmatrix} 211 & 212 & 213 & 214 & 215 & 216 \\ 221 & 222 & 223 & 224 & 225 & 226 \\ 231 & 232 & 233 & 234 & 235 & 236 \\ 241 & 242 & 243 & 244 & 245 & 246 \\ 251 & 252 & 253 & 254 & 255 & 256 \\ 261 & 262 & 263 & 264 & 265 & 266 \end{bmatrix} \rightarrow \begin{bmatrix} 222 & 223 & 224 & 225 & 226 \\ 0 & 233 & 234 & 235 & 236 \\ 0 & 0 & 244 & 245 & 246 \\ 0 & 0 & 0 & 255 & 256 \\ 0 & 0 & 0 & 0 & 266 \end{bmatrix} \rightarrow \begin{bmatrix} 111 & 112 & 0 & 0 & 0 \\ 0 & 112 & 0 & 0 & 0 \\ 0 & 0 & 155 & 0 & 0 \\ 0 & 0 & 0 & 144 & 0 \\ 0 & 0 & 0 & 0 & 155 \end{bmatrix}$$

$$\begin{bmatrix} 311 & 312 & 313 & 314 & 315 & 316 \\ 321 & 322 & 323 & 324 & 325 & 326 \\ 331 & 332 & 333 & 334 & 335 & 336 \\ 341 & 342 & 343 & 344 & 345 & 346 \\ 351 & 352 & 353 & 354 & 355 & 356 \\ 361 & 362 & 363 & 364 & 365 & 366 \end{bmatrix} \rightarrow \begin{bmatrix} 333 & 334 & 335 & 336 \\ 0 & 344 & 345 & 346 \\ 0 & 0 & 355 & 356 \\ 0 & 0 & 0 & 366 \end{bmatrix} \rightarrow \begin{bmatrix} 111 & 0 & 0 & 0 \\ 0 & 155 & 0 & 0 \\ 0 & 0 & 155 & 0 \\ 0 & 0 & 0 & 144 \end{bmatrix}$$

$$\begin{bmatrix} 411 & 412 & 413 & 414 & 415 & 416 \\ 421 & 422 & 423 & 424 & 425 & 426 \\ 431 & 432 & 433 & 434 & 435 & 436 \\ 441 & 442 & 443 & 444 & 445 & 446 \\ 451 & 452 & 453 & 454 & 455 & 456 \\ 461 & 462 & 463 & 464 & 465 & 466 \end{bmatrix} \rightarrow \begin{bmatrix} 444 & 445 & 446 \\ 0 & 455 & 456 \\ 0 & 0 & 466 \end{bmatrix} \rightarrow \begin{bmatrix} 0 & 0 & 0 \\ 0 & 0 & 456 \\ 0 & 0 & 0 \end{bmatrix}$$

$$\begin{bmatrix} 511 & 512 & 513 & 514 & 515 & 516 \\ 521 & 522 & 523 & 524 & 525 & 526 \\ 531 & 532 & 533 & 534 & 535 & 536 \\ 541 & 542 & 543 & 544 & 545 & 546 \\ 551 & 552 & 553 & 554 & 555 & 556 \\ 561 & 562 & 563 & 564 & 565 & 566 \end{bmatrix} \rightarrow \begin{bmatrix} 555 & 556 \\ 0 & 566 \end{bmatrix} \rightarrow \begin{bmatrix} 0 & 0 \\ 0 & 0 \end{bmatrix}$$

$$\begin{bmatrix} 611 & 612 & 613 & 614 & 615 & 616 \\ 621 & 622 & 623 & 624 & 625 & 626 \\ 631 & 632 & 633 & 634 & 635 & 636 \\ 641 & 642 & 643 & 644 & 645 & 646 \\ 651 & 652 & 653 & 654 & 655 & 656 \\ 661 & 662 & 663 & 664 & 665 & 666 \end{bmatrix} \rightarrow [666] \rightarrow [0]$$

## 5.9.2 Energy-strain methodology (SI2)

This supplementary information SI2 provides the detailed information on the energy-strain methodology used in Section 5.4.1 of the paper.

The main principle of energy-strain is shown in Eqn (5.S1). This equation can stop at either quadratic term or cubic term, depending on if TOECs are involved.

$$E = E_0 + V_0\left(\frac{1}{2!}C_{ijkl}\eta_{ij}\eta_{kl} + \frac{1}{3!}C_{ijklmn}\eta_{ij}\eta_{kl}\eta_{mn} + \cdots\right) \quad (5.S1)$$

If Eqn (5.S1) stops at the quadratic term, it shows in a simplified version as Eqn (5.S1a). As mentioned in SI1, there are only three SOECs for cubic material, and thus only three strain sets are required.

$$E = E_0 + V_0\left(\frac{1}{2!}C_{ijkl}\eta_{ij}\eta_{kl}\right) \quad (5.S1a)$$

For the direct numerical simulation (DNS) and linear fitting modules, the strain sets shown below were applied.

$$\Delta E = V(C_{11} + C_{12})\eta^2 + O(\eta^4) \quad (5.S2)$$

$$\eta = \begin{bmatrix} \eta & 0 & 0 \\ 0 & \eta & 0 \\ 0 & 0 & 0 \end{bmatrix}$$

where $\Delta E = E - E_0$.

The tetragonal strains were applied, and the changes of the total energy from its unstrained system can give $(C_{11} - C_{12})$

$$\Delta E = V(C_{11} - C_{12})\eta^2 + O(\eta^4) \quad (5.S3)$$

$$\eta = \begin{bmatrix} \eta & 0 & 0 \\ 0 & -\eta & 0 \\ 0 & 0 & \frac{\eta^2}{1-\eta^2} \end{bmatrix}$$

The value of $C_{44}$ was computed using the following strains.

$$\Delta E = \frac{V}{2} C_{44} \eta^2 + O(\eta^4) \tag{5.S4}$$

$$\eta = \begin{bmatrix} 0 & \frac{\eta}{2} & 0 \\ \frac{\eta}{2} & 0 & 0 \\ 0 & 0 & \frac{\eta^2}{4-\eta} \end{bmatrix}$$

For the non-linear approach, the Eqn (5.S1) will be shown in the form of Eqn (5.S1b), where $C_{ijklmn}$ are the six third-order elastic constants. Thus, the six strain sets were applied, which are shown in the Section 5.4.1 in the manuscript.

$$E = E_0 + V_0 \left( \frac{1}{2!} C_{ijkl} \eta_{ij} \eta_{kl} + \frac{1}{3!} C_{ijklmn} \eta_{ij} \eta_{kl} \eta_{mn} \right) \tag{5.S1b}$$

An example of elastic constants' calculations is shown below. We chose the third-order energy-strain equation, Eqn (5.S1b), with Mode 6 applied strain as the example.

This method is used to obtain the results shown in Section 3.1 in the paper.

1. Relax the unit lattice with all three degrees of freedom under 0 GPa: atomic position, lattice shape and lattice volume
2. Use the relaxed system as the reference system and apply strains.
   In this example, we use Mode 6.

   | | |
   |---|---|
   | M6 | $[0,0,0,2\eta,2\eta,2\eta]$ |

   The strain matrix for M6 is

   $$\begin{bmatrix} 1 & \eta & \eta \\ \eta & 1 & \eta \\ \eta & \eta & 1 \end{bmatrix}$$

   The value of $\eta$ ranges from -0.06 to 0.06.
3. Then relax the strained system only with the freedom of atomic position. This is because the system has already reached the lowest-energy state from step 1.

4. Obtain the corresponding the lattice energy and the strain. Use the unstrained system as the reference and calculate the energy difference.
5. Plot the energy-strain curve, as shown in Figure 5-7

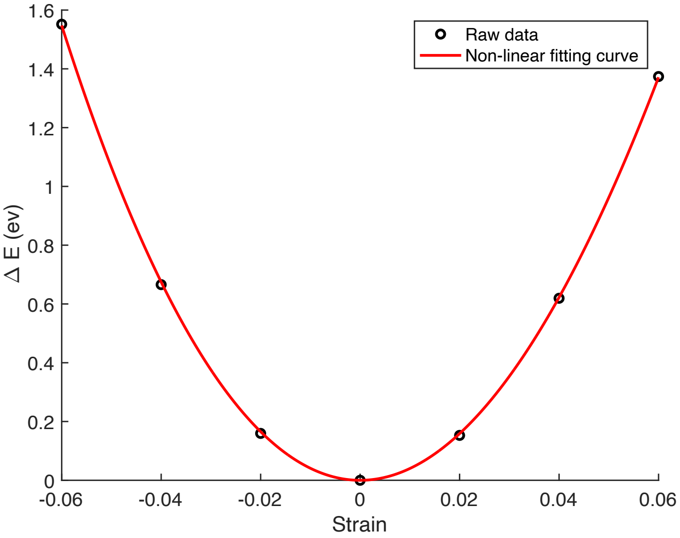

*Figure 5-7 Raw and fitting data for the energy-strain curve under Mode 6 applied strain*

6. Using the MATLAB software to perform the fitting process and fitting equation is Eqn (5.2) in the paper. For Mode 6, we obtained the $A_2$=80.3294 and $A_3$= -242.5375.
7. Table 1 in the paper shows the relationship between the $A_2$, $A_3$ and the SOECs and TOECs. For Mode 6, $A_2$=12$C_{44}$ and $A_3$=46$C_{456}$.
8. The values of $C_{44}$ and $C_{456}$ can be calculated by the values and rules shown in rules 6 and 7. Thus $C_{44}$= 6.6941 and $C_{456}$=-5.0529.

The same process can be applied for the Eqn (S1a), which stops at the quadratic term.

## 5.9.3 sI methane hydrate structure and simulation parameters (SI3)

This supplementary information SI3 provides the detailed information on the hydrate structures and simulation parameters used in Section 5.4.2 of the paper.

The structure of small and large cages in sI methane hydrate is shown in Figure 5-8. White circles represent hydrogen atoms. Brown circles represent carbon atoms. Solid lines represent the covalent bonds between two atoms. The solid is presented with two colors (red and white), which indicate the atoms contributing to the covalent bond. The dashed lines represent the O-H hydrogen bonds.

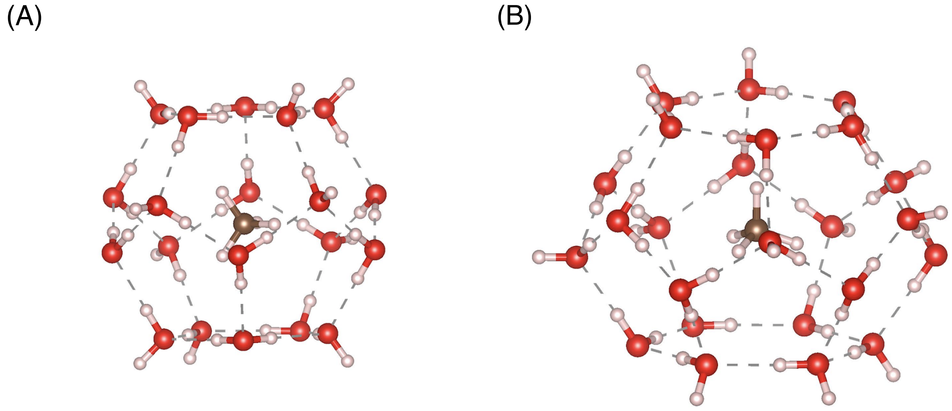

*Figure 5-8 sI methane hydrate (A) small cage, which is the pentagonal dodecahedral water cage, denoted* $5^{12}$ *(B) large cage, which compromises 12 pentagons and 2 hexagons, denoted* $5^{12}6^{2}$*. Red circles represent oxygen atoms. White circles are hydrogen atoms, and brown circles are carbon atoms.*

Density Functional theory (DFT) was manipulated in this paper to run the simulation on the hydrates' relaxation. The key simulation parameters used are listed in Table 5-5.

Table 5-5 Simulation parameters

| | |
|---|---|
| Exchange-correlation functional | revPBE+DFT-D2 dispersion correction |
| Cut-off energy | 520 eV |
| Global break conditions for the electronic self-consistent loop | $1 \times 10^{-4}$ eV |
| Break conditions for the ionic relaxation | $5 \times 10^{-3}$ eV/Å |
| Calculation algorithm | Conjugate gradient algorithms |
| Number of k-points | 4 |
| Grid generation mode | Gamma centered |

## 5.9.4 Mechanical properties calculations (VRH approximation) (SI4)

This supplementary information 4 (SI4) presents all the definitions of elastic properties used in Section 5.5.4 of the paper.

Shear moduli:

$$\mathrm{G_{Reuss}} = \frac{5(\mathrm{C_{11}} - \mathrm{C_{12}})\mathrm{C_{44}}}{4\mathrm{C_{44}} + 3(\mathrm{C_{11}} - \mathrm{C_{12}})} \tag{5.S5}$$

$$\mathrm{G_{Voigt}} = \frac{(\mathrm{C_{11}} - \mathrm{C_{12}} + 3\mathrm{C_{44}})}{5} \tag{5.S6}$$

$$\mathrm{G} = \frac{\mathrm{G_{Reuss}} + \mathrm{G_{Voigt}}}{2} \tag{5.S7}$$

Bulk moduli:

$$\mathrm{B} = \mathrm{B_{Voigt}} = \mathrm{B_{Reuss}} = \frac{(\mathrm{C_{11}} + 2\mathrm{C_{12}})}{3} \tag{5.S8}$$

Poisson’s ratio:

$$\mathrm{v} = \frac{\frac{3}{2}\mathrm{B} - \mathrm{G}}{\mathrm{G} + 3\mathrm{B}} \tag{5.S9}$$

Young’s modulus:

$$\mathrm{E} = 2\mathrm{G}(1 + \mathrm{v}) \tag{5.S10}$$

Longitudinal wave speed:

$$\mathrm{V_p} = \left(\frac{\mathrm{B} + \frac{4}{3}\mathrm{G}}{\rho}\right)^{\frac{1}{2}} \tag{5.S11}$$

Transverse wave speed:

$$\mathrm{V_s} = \left(\frac{\mathrm{G}}{\rho}\right)^{\frac{1}{2}} \tag{5.S12}$$

# Chapter 6

# 6 Atomistic-geometric simulations to investigate the mechanical stability of monocrystalline sI methane hydrates under pressure

---

*Reproduced with permission from Springer Nature, 'Zhu, X., Guerra, A., Servio, P. & Rey, A. D. Atomistic-geometric simulations to investigate the mechanical stability of monocrystalline sI methane hydrates under pressure. Scientific Reports* ***13****, 1907, doi:10.1038/s41598-023-29194-8 (2023).'*

## 6.1 Preface

As discussed in Chapter 4, small and large cages respond differently to pressure, and the law of mixtures can be applied to estimate the effects of small and large cages on the lattice. Therefore, in Chapter 6, a comprehensive geometric analysis of the hydrate lattice was conducted to determine the function of the small and large cages as well as the guest molecules.

It was first determined that sI gas hydrate possesses a two-phase structure. On the basis of the connectivity of the faces, it was concluded that the large cages constitute the matrix phase; in other words, they support the entire lattice structure. The small cages have a role of dispersed inclusions. Then, four scenarios were proposed for occupied cages , and methane was chosen as the sole guest in this work. It was determined that if the large cages are filled, then the entire hydrate lattice can withstand a greater amount of pressure, and can exhibit a multistage fracture mechanism. On the other hand, if only the small cages are occupied, the entire lattice would collapse at once, as a one-step fracture mechanism. This further verifies the previously discovered dispersed inclusion and matrix phase roles of small and large cages in Chapter 4. In addition, to better quantify the relationship between the effects of occupied cages and the pressure stability limits, an equation that takes into account not only the effects of each individual occupied cage, but also their interaction, was proposed. In this study, we also identified the steepest ascending and descending pathways that strengthen and weaken the pressure stability of the hydrate lattice by manipulating chemical composition. In conclusion, Chapter 6 is a continuation and novel extension of Chapter 4. Additional research was conducted on the hydrate lattice structure, and a correlation was established between the occupancy and the pressure stability limits. The equations presented in Chapters 4 and 6 can be used to calculate the stability limits and the mechanical properties of a gas hydrate with any cage occupancy and under pressure.

## 6.2 Abstract

Gas hydrate mechanical stability under pressure is critically important in energy supply, global warming, and carbon-neutral technologies. The stability of these polyhedral guest-host crystals under increasing pressure is affected by host cage type and face connectivity as well as guest gas occupancy. The geometry-imposed cage connectivity generates crystal lattices that include inclusion-matrix material composite structures. In this paper, we integrate Density Functional Theory simulations with a polyhedral-inspired composite material model that quantifies stability limits, failure modes, and the impact of the type of cage occupancy. DFT reveals the existence of two failure mechanisms under increasing pressure: (i) a multistep lattice breakdown under total occupancy and under only large cage occupancy and (ii) a single-step breakdown under zero occupancy as well as with only small cage occupancy. The DFT-composite model predicts optimal occupancy pathways to generate strength and critical occupancy pathways to promote decomposition.

# 6.3 Introduction

Energy production and sustainability have been critical in the past century. An increasing population, diminishing natural resources, and climate change continue to generate challenges and opportunities for high-energy storage materials. Gas hydrates (GH) are hydrogen-bonded polyhedral guest-host materials that have the versatility to store gases critical to energy supply and climate change and yet be formed by water[1]. Energy supply GH includes sI methane and sII hydrogen, where the distinction (sI, sII) refers to the polyhedral cage types and volume fraction in a crystal lattice.

The stability of gas hydrates is crucial and serves as the foundation for all exploration and research. Natural gas hydrates occur in subsea and artic reservoirs on Earth and contain a substantial amount of methane, which has more than 25 times the effect of carbon dioxide on climate change[1]. Consequently, the first application of the results from this work is to inform whether the hydrate structure is mechanically stable and that no methane is escaping during exploration. Specifically, in recent years, global warming and geological movements have led to the instability of natural gas hydrates and the occurrence of methane seepage in some natural gas hydrate reservoirs. Consequently, the study of hydrate stability can help predict hydrates' resistance to climate change and to crustal movements.

Applications to climate change and global warming include $CO_2$ sI GHs that in principle, could be coupled to methane GHs to produce a dual energy-source-and-carbon-sink material system. Currently, hydrogen GHs are being intensely researched and developed due to the opportunity of creating an energy platform of green storage for green hydrogen. Further progress in these energy sources, impact and storage requires a quantitative understanding of mechanical stability limits and failure mechanisms under increasing stress loads and different guest gas compositions and degree of occupancy. In this work, we focus on the mechanical stability of monocrystal methane sI gas hydrates under pressure loads to establish the impact of gas cage occupancy and cage connectivity on failure thresholds and failure modes by integrating atomistic DFT simulations with geometric modelling inspired by composite materials.

Previous research on the stability of gas hydrates based on Density Functional Theory (DFT) and Molecular Dynamics (MD) simulations shed light on various aspects of single cage or lattice scale phenomena. Vlasic, T. M., et al.[2] examined the stability of sII hydrates using the Equation of State (EOS) (Murnaghan, Birch-Murnaghan, Vinet, Liu) and the impacts of various guest molecules on the material properties of the hydrates. They discovered that the hydrogen bond density, which serves as the lattice's sustaining force, and the bulk modulus were shown to have a positive linear connection. However, the bulk modulus drops as the atomic volume rises. Additionally, it was discovered that the larger gas molecules would exert an outward force on the cages due to van der Waals repulsions, growing the cages' dimensions and thereby growing the lattice volume. Daghash, S. M., et al.[3-5] have made a detailed study on the sH gas hydrates in terms of stability. They reported physical properties at the atomistic level using DFT and quantified the dispersion forces[3]. Also, Daghash, S. M., et al.[4] and Vlasic, T. M., et al.[6] used a DFT-based IR spectrum to identify the hydrogen bond's vibration frequency, which can be used to determine the hydrate's Young modulus and provide a better understanding on the host molecular vibrations. Since the vibrational frequency depends on the pressures and bond length, they have presented a new route for mechanical properties determination. In addition, Daghash, S. M., et al.[5] reported the positive linear relationships between the elastic constants and pressures, which implies that the hydrates' physical properties would change and can be quantified under pressures. Mathews, S.

L., et al.[7] examined the thermodynamic parameters of the sI hydrate at various temperatures and came to the apparent consensus that, at lower temperatures, DFT can provide more accurate results than MD. By utilizing the DFT, Jendi, Z. M., et al.[8] discovered that the tensile and compressive ideal strengths of sI pure methane gas hydrates are -1.10 GPa and 90 GPa, respectively. Jia, J., et al.[9] found significant correlations between the second-order elastic constants and pressures, and the piezo effects may differ depending on the type of guest molecules. Mirzaeifard, S., et al.[10] computed the water-methane surface tension by employing pressure and temperature calculations consistent with standard scaling concepts. Guerra, A., et al.[11] investigated the effects of temperature and pressure on the viscosities of methane and carbon dioxide hydrates. They discovered that temperature impacts are often one order of magnitude greater than piezo-viscous effects. Furthermore, pressure had a one-order-of-magnitude more significant influence on the viscosity of carbon dioxide hydrate systems than on methane hydrate systems. Also, Guerra, A., et al.[12] showed that by using the Tip4p/ice water model and the OPLS-AA methane model, molecular dynamics (MD) simulations overestimated the experimental data of sI methane hydrate viscosity under pre-nucleation conditions by 84% on average across all conditions examined. Guerra et al.[13] similarly demonstrated through MD simulations an overestimation of the viscosity of carbon dioxide hydrate systems of 65% on average across all conditions examined for the three $CO_2$ force field considered: EPM2, TraPPE, and Zhang. Wu, J., et al.[14] showed that the natural gas hydrates would be further destabilized and beyond the conventional thermodynamic instability if there is some force-induced ground deformation based on the deformation-induced hydrate dissociation they discovered. Zhu, X., et al.[15,16] work at the stability of the sI methane hydrate under pressures. They stated that the piezo effect might be seen from the perspectives of electron clouds, atoms, cages, and lattices[16], along with the values of second-order elastic constants with pressure restrictions[15]. Also, they confirmed that the sI methane hydrates obey the law of mixture[16] in the calculation of the structure's bulk modulus.

The standard for analyzing the piezo effect on the mechanics of gas hydrates involves an examination of the second-order elastic constants, the bulk modulus, the Young modulus and other properties. All these studies, however, are premised on the assumption that forces or energy are distributed uniformly throughout the lattice and that the system is within the stability limits. Within the stability limits, a coarse-grained law of the binary mixture method was successfully implemented under full occupancy for methane GH. To resolve the effect of magnitude (volume fraction effect) and type (small cage and/or large cage) of gas occupancy, a ternary component model is necessary since a crystal lattice has three interacting components: the hydrogen bond network, the small polyhedral cages and the large polyhedral cages. After recognizing these three components, the next step is to introduce polyhedral connectivity which together with cage number density defines a cage type as an inclusion or as a continuous matrix and leads to laws of mixtures for material stability under variable composition and cage type occupancy. The three key phenomena addressed in this paper are: (1) what are the stability limits of methane GH under increasing pressure under variable composition and cage occupancy? (2) what are the possible failure mechanisms under various composition and cage occupancy limiting modes? (3) find the stability surface as a function of cage occupancy and the critical steepest occupancy curves that characterize optimal reinforcement and maximal failure conditions.

This work is on monocrystal methane sI stability and failure modes under pressure, and no phase transitions to other hydrates are considered. DFT simulations are at 0 Kelvin. For each DFT simulation, the cage occupancy is fixed until ultimate failure conditions. To clarify, the only situations in this paper that involve thermodynamic stability are the DFT simulations. This is because, under the given conditions, DFT simulations would relax the system to its lowest-energy state, which is the thermodynamic equilibrium. However, stability limits refer to mechanical stability limitations. It represents the maximum pressure the system can withstand before being destabilized by mechanical forces. Since this work focuses on investigating the piezo effect on structural stability, the research of thermodynamic stability is beyond the scope of this work. The stability surface (Monge patch[17]) is derived from a ternary law of mixtures taking into account the first-order cage-cage interaction nonlinearity. Additionally, computational work involving gas hydrates is benefitted by the integrated use of experimental data[18]. However, to the best of our knowledge, experimental data relevant to the analysis performed here is not available in the literature. Conditions, processes, and mechanisms outside those mentioned above are outside the scope of this paper and can be included in future work as experimental data at the relevant scales becomes available. In this paper, we use, without ambiguity, the following nomenclature for the four existing phases (modes): (i) inclusion phase: small cages are occupied, and large cages are empty, denoted by SOLE; (ii) matrix phase: small cages are empty and large cages are occupied; denoted by SELO; (iii) hydrogen network phase: all cages are empty, denoted by SELE; (iv) composite phase: all cages are occupied, denoted by SOLO.

This paper is organized as follows. In the results section, the inclusion and matrix phases of the sI methane hydrate were identified via polygonal connectivity through face sharing. The stability thresholds in terms of phase modes were then determined, identifying two failure patterns. The correlation between the phase occupancy and compressive stability limits is then established. The use of a ternary non-ideal laws of mixtures in conjunctions with computed DFT stability limits leads to the equation for the mechanical stability surface under variable methane occupancy. Computing the steepest descent and ascent curves leads to the identification of optimal strengthening by specific gas occupancy and maximal failure routes by a decrease of mainly large cage occupancy. All these findings can be applied to other types of gas hydrates. Finally, all methodologies and software applied in this work are presented in the SI and main text. Details of equations and mechanisms are discussed. This work contributes to and accelerates the identification of the gas hydrates' stability under pressure. The results from this work may be crucial in developing hydrate technologies that involve the medium- and long-term storage of gases in the hydrate phase.

# 6.4 Results and Discussion

## 6.4.1 Two-phase structure determination

The sI gas hydrate structure consists of two small cages and six large cages. The small cages ($5^{12}$) contain 12 pentagonal faces, and the large cages ($5^{12}6^{2}$) contain 12 pentagonal faces and two hexagonal faces. Also, taking advantage of a Three-Dimensional Visualization System for Electronic and Structural Analysis (VESTA 3)[19], we could visualize the multi-phase structure directly, as shown in Figure 6-1.

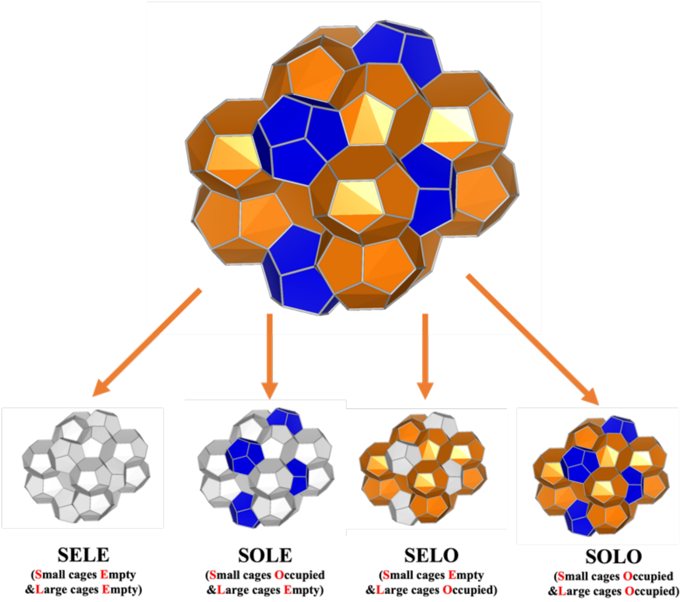

*Figure 6-1 sI gas hydrate's structure colored according to their cage types. The occupied large cages are shown in orange, the occupied small cages are shown in dark blue, and the empty cages are shown in white. Four different occupancies are shown. They are SELE (small cages empty and large cages empty), SOLE (small cages occupied and large cages empty), SELO (small cages empty and large cages occupied) and SOLO (small cages occupied and large cages occupied).*

Figure 6-1 presents the four different occupancy modes of sI methane hydrate within one unit lattice. The occupied small cages, shown in dark blue, are distributed dispersedly. In other words, all small cages are surrounded by large cages, and they cannot connect with each other. On the other side, large cages are connected and shown in orange.

In nature, the occupancy of gas hydrates is often greater than zero, which means some gas molecules would be trapped in the lattice. However, the empty gas hydrates were confirmed to be present under certain conditions[20-23] – temperatures between 100 K and 220 K and pressures between 1 and 5000 bar. Thus, four different occupancies proposed and shown at the bottom of Figure 6-1 are SELE (small-empty-large-empty), SOLE (small-occupied-large-empty), SELO (small-empty-large-occupied), and SOLO (small-occupied-large-occupied). If the cages are not occupied or empty, they are shown in white. Otherwise, they are shown in their corresponding colors (dark blue for occupied small cages and orange for occupied large cages).

The continuous and dispersed roles of large and small cages in the lattice are evident in Figure 6-1, which is attributed to the face connection. There are two types of faces to establish the cages and lattice: pentagonal and hexagonal faces. Pentagonal faces are involved in both small and large cages, and hexagonal faces are only formed in large cages. Each face is shared by two cages regardless of the type of cage and faces. There are six hexagonal faces in one unit lattice, and each hexagonal face would be shared by two different large cages. Also, there are 48 pentagonal faces. Half of the pentagonal faces are among large cages. However, another half is shared between one large and one small cage. According to these face-sharing principles, all faces contribute to the large cages, regardless of partial or complete involvement. In other words, if large cages exist, the small cages would be necessarily present. On the other hand, if only the small cages exist, it means that only two dispersed inclusions form since there is no shared face between the two small cages. In other words, there is no evidence to make any conclusion on large cages or lattices.

## 6.4.2 Effects of phase occupancy on the pressure stability of hydrates

From previous study, the small cages are recognized as the dispersed inclusion and large cages are identified as the continuous phase in the lattice[16]. The simulations were performed on sI methane hydrates with four different occupancies, pressures ranging from 0 GPa to 7.6 GPa, and at zero Kelvin; the unit lattice was the supercell. Six large tetradecahedral ($5^{12}6^{2}$) and two small dodecahedral ($5^{12}$) polyhedral cages were involved in one unit lattice. As discussed in the previous section, four occupancies were considered: SELE, SOLE, SELO and SOLO. The effects of different occupancies (four modes mentioned above) on lattice volume under compressive pressures are shown in Figure 6-2.

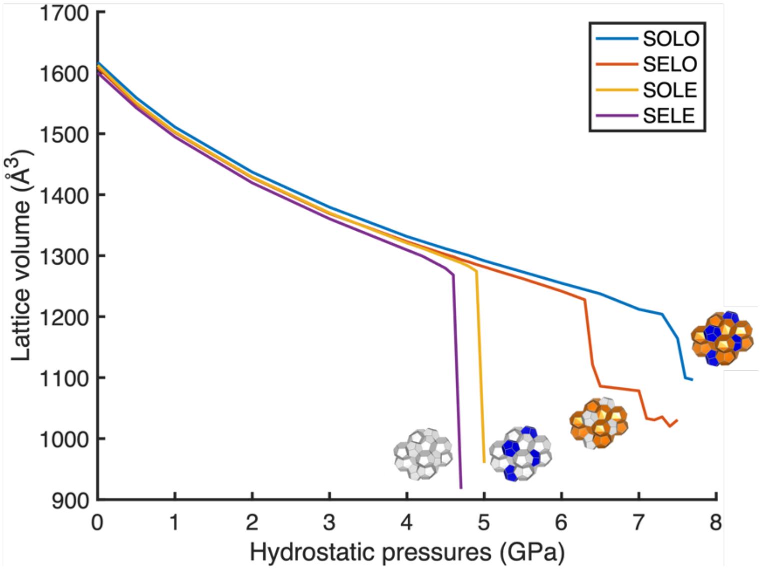

*Figure 6-2. Lattice volume as a function of hydrostatic pressures from 0 GPa to 7.6 GPa with four different occupancies. The blue line is for the SOLO hydrate. The orange line is for the SELO hydrate. The yellow and purple are for the SOLE and SELE hydrates. See text for nomenclature.*

Figure 6-2 shows the variations in lattice volume under pressures ranging from 0 to 7.6 GPa. In the region of low pressure, between 0 GPa and 4.5 GPa, the performances of all four modes are comparable. In this pressure region, all four modes exhibit a modest declining trend and a slight variation in magnitude. Compared with results from previous work[24], the values of unit lattice volume presented here are in the same order of magnitude. For example, Jendi, Z. M., et al.[24] shows the unit lattice volume of SOLO hydrate is approximately 1685 Å$^3$, which is very close to our result 1620 Å$^3$. At 0 GPa, the volumetric difference between SOLO occupied and SELE lattices was approximately 1%. Although SOLE has a greater lattice volume under certain low pressures than SELO, the difference is too small to determine whether occupied small cages have a stronger effect than occupied large cages. From a qualitative standpoint, we can conclude that the occupancy has no significant effect on the stability of the hydrate lattice under pressures ranging from 0 to 4.5 GPa. Based on these findings, between 0 GPa and 4.5 GPa, the hydrogen bonding lattice supporting forces are dominant over the guest-host interaction supporting forces. This is because, under 4.5 GPa, all four cases are stable, and the volumetric difference is less than 5%. Since SELE hydrate failed at 4.7 GPa, 4.6 GPa was considered its compressive stability limit. The cage volumes for empty sI hydrate under 4.6 GPa are also considered the minimum hydrogen-bonded tetradecahedral ($5^{12}6^{2}$) and dodecahedral ($5^{12}$) cages volumes, respectively, as shown in Table 6-1.

*Table 6-1 Cage sizes for empty sI hydrate under 4.6 GPa, where the empty hydrate can support the maximum compressive pressure. Cages 1 and 2 are the small cages, and cages 3-8 are the large cages.*

| **Small cages** | **Cage 1** | | | **Cage 2** | | |
|---|---|---|---|---|---|---|
| **Cage size ( Å$^3$ )** | 123.94 | | | 128.87 | | |
| **Large cages** | **Cage 3** | **Cage 4** | **Cage 5** | **Cage 6** | **Cage 7** | **Cage 8** |
| **Cage size ( Å$^3$ )** | 181.55 | 181.55 | 171.68 | 171.68 | 171.29 | 171.29 |

Table 6-1 shows detailed information on cage sizes for empty sI hydrate under 4.6 GPa. Small cages have volumes around 120 Å$^3$, the large cages would have volumes ranging from 171 Å$^3$ to 182 Å$^3$. Since these values represent the cage sizes under maximum pressure without losing lattice integrity, these numbers can serve as minimum stable volumes for tetradecahedral (large) and dodecahedral (small) cages. In other words, any smaller size without additional supporting force (e.g., the presence of guest molecules) can be identified as cage failure.

Figure 6-2 shows that once the pressure exceeds 4.5 GPa, hydrates having different occupancies respond differently. This is because the guest-host interaction starts to become a dominant effect. The figure allows for the classification of the four modes into two groups. The SOLO and SELO cases had comparable trends, while the SOLE and SELE cases exhibited similar behavior. The volume sizes of SOLO and SELO hydrates overlap when the pressure is below 6.4 GPa. However, once the pressure increased from 6.3 GPa to 6.4 GPa, the lattice volume of the SELO case unexpectedly decreased from 1227.72 Å$^3$ to 1121.34 Å$^3$, where the volume changes are ten times greater than the amount of volume change under a lower pressure with the same magnitude of pressure change. A similar volume drop takes place on the SOLO hydrates but under greater pressure (7.3 GPa). After the first drop, both SELO and SOLO hydrates seem to reach a plateau. After the plateau, the SELO and SOLO hydrates had their second volume drop at 7.1 GPa and 7.6 GPa, respectively, followed by a short plateau again. In Figure 6-2, SELO shows more discrete changes in lattice volume than SOLO because SELO has a 1.3 GPa pressure range to show its failure response while SOLO only has 0.3 GPa. This pressure range is determined between the maximum simulation pressure limits 7.6 GPa and their first volume drop pressure. In other words, the SOLO structure exhibited a higher resistance to volume change (higher mechanical stability) than the SELO structure, due to the occupation of its small cages.

However, the SOLE and SELE hydrates have completely different responses. The SOLE and SELE hydrates have their first drop under 4.9 GPa and 4.6 GPa respectively. Unlike the SOLO and SELO hydrates, no plateau emerges after the volume drop, and it seems they shrink to their minimum volume, where no lattice structure exists. In other words, the volume size represents the sum of the atoms and molecules in the lattice. Comparing to previous work[15,16], the compressive pressure limit for SOLO sI methane hydrate is 7.5 GPa, which is in agreement with the first volume drop of SOLO hydrate at 7.3 GPa shown in Figure 6-2. The results' reliability and accuracy are further discussed below.

### 6.4.3 Relationship between phase occupancy and compressive stability limits

In the previous section we obtained the maximum pressures, which were recognized as the stability limits, that the hydrate structure can withstand without sacrificing the lattice volume. Considering the law of mixtures, the property of the composite material is the weighted average of the property values of constituent materials. This idea can be extended to the prediction of stability limits, where the volumetric ratio is replaced by the lattice occupancy with respect to small and large cages.

The differences among first volume drop critical pressure points imply a relationship between the phase occupancy and compressive stability limits. The effects from occupied small and large cages are significantly different, and the interactions among occupied cages are important. Thus, in this section, we will quantify the impacts of these effects under pressure.

*Table 6-2 Compressive pressure points (see Figure 6-2) for first significant volume drop for sI methane hydrates with four different occupancies (SELE, SOLE, SELO and SOLO)*

| SELE | SOLE | SELO | SOLO |
|---|---|---|---|
| 4.6 GPa | 4.9 GPa | 6.3 GPa | 7.3 GPa |

Table 6-2, shows the critical pressure points for the first significant volume drop for sI methane hydrates with four different occupancies (see Figure 6-2). In general, the pressure at which the first volume drop occurs increases as the occupancy increases, which is reasonable. Since more cages are occupied, more guest-host interactions can be used to stabilize the lattice. For quantification, two assumptions were made to establish an equation between the critical pressure points (pressures for the first significant volume drop) and phase occupancy. Firstly, it is linearly correlated between the phase occupancy and critical pressure points. Secondly, only the interactions among different cages are considered. The interactions within the same type of cages are ignored.

Four modes and a canonical equation are proposed to quantify the occupancy effects on the compressive stability limits, as shown in Eqn (6.1). Although Eqn (6.1) is inspired from the ideal law of binary mixtures, they have four main differences. Firstly, there are three components in Eqn (6.1) (hydrogen-bonded skeleton, small and large cage's occupancies) instead of two in law of mixtures. Secondly, the variables X and Y in Eqn (6.1) have values between 0 and 1; however, in law of binary mixtures the sum of the volumetric ratio is constrained to 1. Thirdly, in Eqn (6.1), the (X,Y) variables are occupancy instead of the volumetric ratio. Lastly, cage occupancy interaction between large and small leads naturally to the last term in Eq.1. The analysis and DFT data is synthesized in terms of a stability surface S(X,Y):

$$\mathrm{S}\ (X, Y) = \mathrm{a} + \mathrm{bX} + \mathrm{cY} + \mathrm{dXY} \tag{6.1}$$

where S stands for the compressive stability limit (GPa), X is the small cages' occupancy and Y is the large cages' occupancy, and a, b, c, and d are constants. There are four terms in Eqn (6.1). One constant term shows as 'a'. Two linear correlated terms, 'bX' and 'cY', are used to describe the occupied small and large cages, respectively. The fourth term 'dXY' describes the interaction between occupied small and large cages. According to the four different occupancies mentioned above and, in the introduction, four modes are proposed, as shown Table 6-3. The network mode, which represents the hydrogen-bonded skeleton, describes the SELE hydrate. The inclusion and matrix modes demonstrate the SOLE and SELO hydrates. The composite mode describes the SOLO hydrates.

*Table 6-3 The four occupancy modes that contribute to the overall compressive stability model in Eqn (1).*

| | |
|---|---|
| **Network mode (SELE)** | $S = a$ |
| **Inclusion mode (SOLE)** | $S = a + bX$ |
| **Matrix mode (SELO)** | $S = a + cY$ |
| **Composite mode (SOLO)** | $S = a + bX + cY + dXY$ |

With the four critical points shown in Table 6-2, the assumption listed above and the proposed generic surface stability equation, we obtained a specific equation, as shown in Eqn (6.2). The constant term, 4.6, is from the SELE (empty) hydrates. The coefficients 0.3 and 1.7 are obtained from the differences between SOLE and SELE and between SELO and SELE, where the extended stability limits are only from the occupied small or large cages. To estimate the interactions between different types of cages, we calculated the differences between SOLO and SOLE and between SOLO and SELO. Both are 0.7 GPa, indicating that large and small cages would boost another type of occupied cages by 0.7 GPa. In Eqn (6.2), S stands for the compressive critical pressure points or stability limits. X and Y are replaced by $Q_s$ and $Q_l$, which are the small and large cage occupancy respectively (between 0 and 1).

$$S\ (\mathrm{GPa}) = 4.6 + 0.3 \times Q_s + 1.7 \times Q_l + 0.7 \times Q_s\, Q_l \tag{6.2}$$

The detailed comparisons between ideal constrained binary and nonlinear unconstrained ternary mixture models are shown in the Supporting Information (SI1).

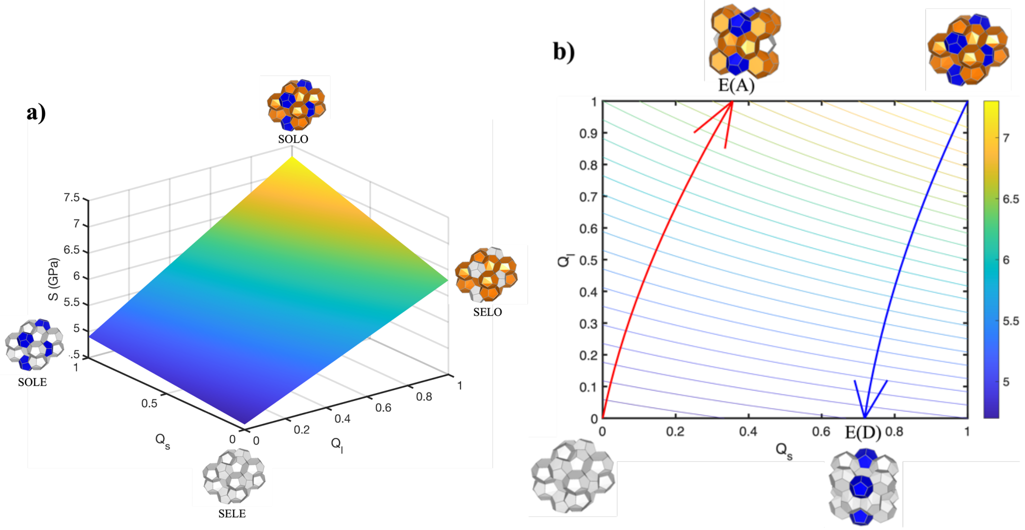

*Figure 6-3 Relationship between compressive stability limit and phase occupancy. Qs and Ql are the occupancies of small and large cages, respectively. (a) A 3D surface shows the compressive stability limits change with phase occupancy. (b) indicates the contour level with step size 0.1 GPa. The red arrow curve is the steepest ascent curve, and the blue arrow curve is the steepest descent curve, which is the fastest way to increase and decrease stability limits. E(A) and E(D) indicate the ending points for the ascent and descent curves, respectively. The color bar represents the stability limit values from 4.6 GPa to 7.3 GPa, with a unit of GPa.*

A 3D surface and contour levels were generated for Eqn (6.3), as shown in Figure 6-3. Figure 6-3(a) shows the relationship between the compressive stability limits and phase occupancy ($Q_s$ and $Q_l$). The stability limits range from 4.6 GPa to 7.3 GPa. Figure 6-3(b) shows the contour levels with a step size of 0.1 GPa.

The two curves in Figure 6-3b are generated by using the standard steepest ascent/descent method. The red curve shows the steepest changing pathway to increase the stability limits from empty hydrates, and the blue curve shows the steepest changing pathway to decrease the stability limits from fully occupied hydrates. The steepest ascent curve ends at $E(A) = (0.3524,1)$,where the stability limit equals to 6.65 GPa. The steepest descent curve ends at $E(D) = (0.7136,0)$, where the stability limit equals to 4.81 GPa. From the values of ending points, we find that the values of $Q_l$ are either 1 or 0, which means the occupancy of large cages has the dominant role for the entire lattice's stability. On the other hand, the difference between the $Q_s$ values of E(A) and of (D) is relatively small, indicating the secondary role of small cage occupancy.

Using the steepest descent/ascent curves of the stability surface, predictions to capture the relationship between cage occupancy to achieve the fastest way to increase or decrease the stability limits can be established as follows:

$$0.35\left(Q_l{}^2 - Q_s{}^2\right) + 0.3(Q_l - 5.67Q_s) = K_i(GPa), i = A, D \tag{6.3}$$

$i = A, K_A = 0$: steepest ascent from SELE (network) state

$i = D, K_D = -1.4$: steepest descent from SOLO (composite) state

Equation 6.3 (see SI for derivation) shows that the relationship between unconstrained occupancy $Q_l$ and $Q_s$ is hyperbolic, reflecting the impact difference between large and small cage effects. The stability limits' values for the terminal stage for optimal strengthening E(A) and for largest stability drop E(D) are:

$$S\big(E(A)\big) = S_{max} - (b + d)\left[1 + \frac{c - \sqrt{c^2 + 2bd + d^2}}{d}\right] \tag{6.4}$$

$$S\big(E(D)\big) = S_{min} + \frac{-c + \sqrt{c^2 - 2bd + 2dc}}{d} \tag{6.5}$$

Where $\{a, b, c, d\} = \{4.6, 0.3, 1.7, 0.7\}$ (coefficients in Eqn (6.2)); $S_{max} = S(Q_s = 1, Q_l = 1)$ and $S_{max} = a + b + c + d$; $S_{min} = S(Q_s = 0, Q_l = 0) = a$. Eqns (6.4-6.5) explain why the end points (E(A), E(D) in Figure 6-3) do not achieve the minimum and maximums stability limits values when following the dominant curves of steepest ascent/descent curves of the stability surface S. The presence of second terms in Eqns (6.4-6.5), accounting for cages (coefficients b and

c) and cage interaction (coefficient d) effects, indicate the difference. This mechanical response to composition clearly indicates the limitations of the optimal path to achieve maximal strength and the destabilizing nature of losing large cage occupancy.

To evaluate the consistency between the DFT stability limits and the values calculated by using the mixture model (Eqn (6.2)), three arbitrary occupancy modes were selected. Detailed information on occupancy is shown in Table 6-4.

*Table 6-4 Comparison between DFT simulations and mixture model (Eqn (6.2)) with 50% occupancy in three representative modes.*

| | Inclusion mode $Q_s = 0.5;\ Q_l = 0$ | Matrix mode $Q_s = 0;\ Q_l = 0.5$ | Composite mode $Q_s = 0.5;\ Q_l = 0.5$ |
|---|---|---|---|
| DFT Stability limits (GPa) | 4.7 | 5.2 | 5.6 |
| Calculated stability limits by using Eqn (6.2) (GPa) | 4.75 | 5.45 | 5.95 |

Table 6-4 shows the compressive stability limits for three representative cases; the inclusion mode has only 50 % of small cages being occupied, the matrix mode has only 50% of large cages occupied, and the composite mode has 50% of small cages and 50% of large cages occupied. These three modes with 50% occupancy provide a clear understanding of both individual cages' effects and their interactions. DFT simulations for the three modes have precisions of 0.1 GPa, and the precision cannot be smaller due to computational cost. The DFT results are obtained by relaxing the three selected modes of hydrates under pressure and finding the maximum pressure that the hydrate lattice can support before first significant volume drop. Table 6-4 shows that the DFT simulation and the mixture model (Eqn (6.2)) results are in very or excellent agreement. Although values from Eqn (6.2) can be greater than the simulation results, the discrepancies are always less than 10%, which implies the validity of the previously mentioned two assumptions and further confirms the accuracy of Eqn (6.2).

### 6.4.4 Failure Mechanisms

Figure 6-2 shows two different behaviors when the system approaches instability thresholds. The SELE and SOLE hydrates show a sudden step-like volumetric drop. On the other hand, the SOLO and SELO hydrates showed sequential staircase-like volume drops. To further understand the reasons for the sequential volume drops, we use Visualization for Electronic Structural Analysis (VESTA), to ascertain if there is any failure or intermolecular distortion in the lattice.

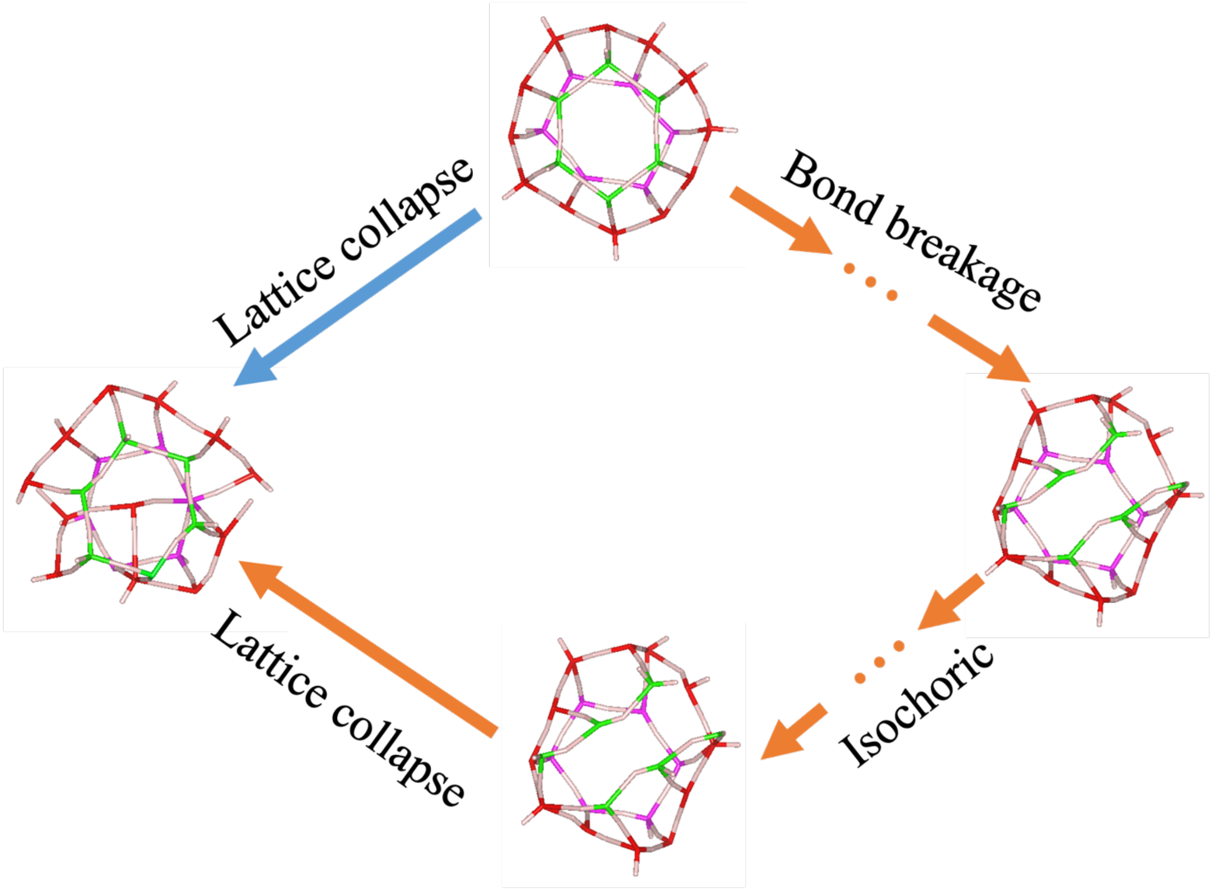

*Figure 6-4 Two failure mechanisms when approaching the compressive stability limit. The Failure Mechanism 1 (orange arrowed lines) found in SOLO and SELO hydrates has three steps: bond breakage, isochoric deformation, and lattice collapse. The arrow-dot-arrows represent sequential steps that take places several times before the lattice fails. The bond breakage step shows a significant volume drop, where bonds sacrifice at high pressures. The isochoric step indicates the hydrate system reaches a plateau with no volume change even when additional pressures are applied. Lattice collapse is the last step and represents a systematic failure. The Failure Mechanism 2 found in SELE, and SOLE hydrates is shown in blue. It has only one step and is the same as the last step of Failure Mechanism 1, where the system lost its lattice integrity.*

Figure 6-4 shows the two failure mechanisms that take place when the compressive stability limits are approached. The Failure Mechanism 1 (orange arrows) has three steps and Failure Mechanism 2 has only one step (blue arrows). Both mechanisms involve significant volume drops. The Failure Mechanism 1 was shown in the SOLO (composite) and SELO (matrix) hydrates. Meanwhile, the Failure Mechanism 2 was shown in the SELE (network) and SOLE (inclusion) hydrates.

The existence of two failure mechanisms is determined by how widely distributed the supporting forces are. Above 4.5 GPa, the hydrogen bond system cannot support the cage and lattice by itself. Thus, the guest-host interaction becomes very important for the hydrate's stability. Both SELE (network) and SOLE (inclusion) hydrates display the Failure Mechanism 2 because they do not have any occupied large cages. As discussed above, the small cages are dispersed and do not connect with each other. Thus, guest-host interactions can only be limited to local areas. As expected, the SOLE hydrates do have a greater stability limit than SELE, as shown in Figure 6-2, but the same failure pathway.

However, the SELO (matrix) and SOLO (composite) hydrates exhibit Failure Mechanism 1 instead of Failure Mechanism 2. Failure Mechanism 1 is a sequential or multi-step mechanism. At sufficient low pressure, although the cages are deformed, the faces' and cages' integrity were present. However, once the pressure reaches the first volume drop threshold, one hexagonal ring opens by bond breakage. It is possible that a couple of pentagonal faces sacrifice instead of hexagonal faces, but the main idea is that the cage integrity remains. At the same time, some bonds break, causing a significant volume drop. The two layers of pentagonal rings are the main body of the large cages. If they are complete and intact, the lattice's guest-hosting capability is still present. In the isochoric zone, the change in volume is negligible compared to the magnitude of the total volume. This zone does experience a small volume decrease, as seen in Figure 6-2. From Figure 6-2, both SELO (matrix) and SOLO (composite) hydrates show that the lattice volume becomes constant for a while after a significant volume drop, even when additional pressure is applied. This can be explained as the structure has changed to a new stable structure under pressure. Bond breakage and isochoric steps may take place several times before the final step (lattice collapse) is triggered. In summary, the volume drops and stabilizes several times before the final collapse. Due to computational costs and capabilities, the results beyond 7.6 GPa are out of convergence reach, and the final collapses of SOLO and SELO hydrates are not captured. But with all the information we have so far, the failure mechanism can be deduced without any ambiguities.

## 6.5 Methods and Tools

### 6.5.1 DFT simulations and computational analyses

First principle DFT calculations were performed by using VASP software. To obtain the lowest energy system under different pressures, we must relax the hydrate lattice in all three degrees of freedom (e.g., atomic positions, lattice volume and structural shape). The sI methane hydrates consist of the water molecules forming the host cages and methane molecules are the guest molecules. For the water cages, the water oxygen atoms' positions can be determined by X-ray diffraction, with the positions of water hydrogen atoms proposed by Takeuchi et al.[25] , which followed the Bernal-Fowler ice rules[26]. Methane molecules were selected to be the only guest molecules in the simulation box. They were placed at the center of each cage in the initial structure.

In the unit lattice of sI hydrate there are 46 water molecules, which form two small cages and six large cages. The small cages ($5^{12}$) contain 12 pentagonal faces and the large cages ($5^{12}6^{2}$) contains 12 pentagonal faces and two hexagonal faces. Considering the size of host cages and guest molecules, each cage can only have one methane molecule, regardless the cage type. The details of small and large cages are shown in Figure 6-5.

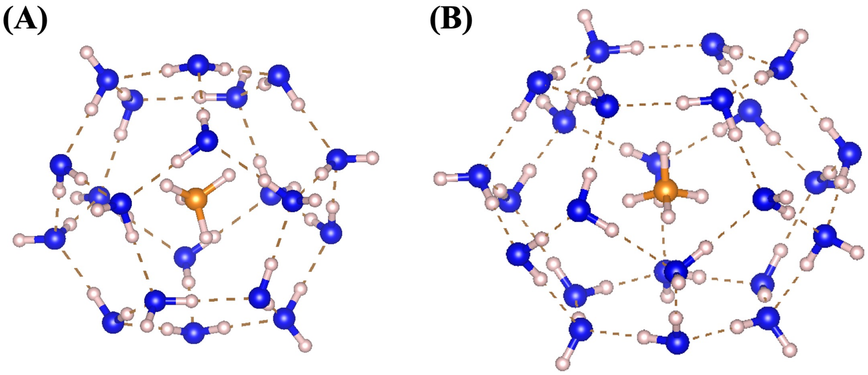

*Figure 6-5 sI methane hydrates have small (A) and large (B) cages. (A) A small cage consists of 12 pentagonal faces and a methane molecule at its center. Large cages (B) have 12 pentagonal faces and two hexagonal faces, with a guest methane molecule at the center. Water oxygen atoms are represented by blue circles. Hydrogen atoms are represented by pink-white circles. Carbon atoms are denoted by orange circles. All solid lines represent covalent bonds; their colors indicate which two atoms formed the covalent bond. OH hydrogen bonds are displayed by the brown dashed lines.*

As mentioned above, VASP was selected as the DFT implementation for all simulations in this work. The simulation involves one unit lattice of sI methane hydrate shown above at zero Kelvin with periodic boundary conditions. The conjugate-gradient algorithm was used since it has a reliable performance within or beyond the pressure stability limits[15]. Based on previous studies on gas hydrate[2,5,8,15,16], the revised Perdew-Burke-Ernzerhof (revPBE) exchange-correlation functional and the DFT-D2 dispersion correction method was selected[15,16,27]. Projector augmented wave potential[28,29] was employed for all calculations. Furthermore, 520 eV was chosen as the cut-off energy for the entire simulation process. As recommended by the VASP manual[30], the cut-off energy needs to be set at a level that is 30% higher than the maximum energy of all the atoms that were included in the simulation. For the electronic minimization, a 4×4×4 Gamma centered mesh was used[15,16]. Four subdivisions were selected in each reciprocal lattice vector considering the results' accuracy and computational cost. All simulation details can be found in our previous work[15,16], including the unit lattice preparation, parameter setting and structure relaxation.

### 6.5.2 Contour levels and Steepest decent method

The contour levels and steepest decent method are applied for the surface generated by Eqn (6.4). The contour levels are set with the step size of 0.1 GPa to show how values of stability limits evolve with occupancy. The steepest descent method was used to generate two critical curves to show the fastest pathways to increase or decrease the stability limits. The algorithm is shown below. $F(X, Y)$ is a multi-variable function with variables X and Y. The initial points are selected as $x_0$ and $y_0$. $\gamma$ is the step size. In this paper, a fixed step size of 0.02 was selected. The values are small enough to capture all the changing tendencies. The optimization method of step size was not applied, because we have some restrictions in this project. For example, the stability limits cannot be negative. Thus, a fixed step size with a small enough value would be the best choice. Calculations would keep iterated until $\mathrm{F}(\mathrm{x}_{\mathrm{n+1}}, \mathrm{y}_{\mathrm{n+1}}) < \text{Lower Limit}$ or $\mathrm{F}(\mathrm{x}_{\mathrm{n+1}}, \mathrm{y}_{\mathrm{n+1}}) > \text{Upper Limit}$.

$$x_{n+1} = x_n \pm \gamma \nabla F(x_n) \quad (6.6)$$

$$y_{n+1} = y_n \pm \gamma \nabla F(y_n) \quad (6.7)$$

Alternatively, to this standard numerical approach, the equations in SI 2 can be used to calculate the steepest ascent/descent curves.

## 6.6 Data availability

Data related to this work will be made available by request to the authors. These requests should be addressed to the corresponding author A.D.R. at alejandro.rey@mcgill.ca.

## 6.7 Acknowledgements

This work was supported by Compute Canada and Calcul Québec. A.D.R. and P.S. are thankful for the Natural Sciences and Engineering Council of Canada (NSERC) for funding through the Discovery Grant Program. A.D.R. is thankful for the James McGill Professorship appointment funding, McGill University. X.Z. is thankful for the support through the McGill Engineering Doctoral Awards (MEDA), the Graduate Excellence Award, and the McConnell Memorial Fellowship Award of the Chemical Engineering department, McGill University. A.G. is thankful for the NSERC Canada Graduate Scholarship-Doctoral (CGS-D) award.

## 6.8 Author contributions

X.Z. conducted data collection and analysis. X.Z., A.G., P.S., and A.D.R. discussed the results and contributed to the writing of the manuscript. P.S. and A.D.R. originated and supervised the research.

## 6.9 Competing Interests

The authors declare no competing interests.

## 6.10 References

1 Sloan Jr, E. D., Koh, C. A. & Koh, C. A. Clathrate Hydrates of Natural Gases. doi:10.1201/9781420008494 (2007).

2 Vlasic, T. M., Servio, P. & Rey, A. D. Atomistic modeling of structure II gas hydrate mechanics: Compressibility and equations of state. *AIP Advances* **6**, 085317, doi:10.1063/1.4961728 (2016).

3 Daghash, S. M., Servio, P. & Rey, A. D. Structural properties of sH hydrate: a DFT study of anisotropy and equation of state. *Molecular Simulation* **45**, 1524-1537, doi:10.1080/08927022.2019.1660326 (2019).

4 Daghash, S. M., Servio, P. & Rey, A. D. From Infrared Spectra to Macroscopic Mechanical Properties of sH Gas Hydrates through Atomistic Calculations. *Molecules* **25**, 5568, doi:10.3390/molecules25235568 (2020).

5 Daghash, S. M., Servio, P. & Rey, A. D. First-Principles Elastic and Anisotropic Characteristics of Structure-H Gas Hydrate under Pressure. *Crystals* **11**, doi:10.3390/cryst11050477 (2021).

6 Vlasic, T. M., Servio, P. D. & Rey, A. D. Infrared Spectra of Gas Hydrates from First-Principles. *The Journal of Physical Chemistry B* **123**, 936-947, doi:10.1021/acs.jpcb.8b10223 (2019).

7 Mathews, S. L., Servio, P. D. & Rey, A. D. Heat Capacity, Thermal Expansion Coefficient, and Grüneisen Parameter of CH4, CO2, and C2H6 Hydrates and Ice Ih via Density Functional Theory and Phonon Calculations. *Crystal Growth & Design* **20**, 5947-5955, doi:10.1021/acs.cgd.0c00630 (2020).

8 Jendi, Z. M., Servio, P. & Rey, A. D. Ideal Strength of Methane Hydrate and Ice Ih from First-Principles. *Crystal Growth & Design* **15**, 5301-5309, doi:10.1021/acs.cgd.5b00829 (2015).

9 Jia, J., Liang, Y., Tsuji, T., Murata, S. & Matsuoka, T. Elasticity and Stability of Clathrate Hydrate: Role of Guest Molecule Motions. *Scientific Reports* **7**, doi:10.1038/s41598-017-01369-0 (2017).

10 Mirzaeifard, S., Servio, P. & Rey, A. D. Molecular Dynamics Characterization of Temperature and Pressure Effects on the Water-Methane Interface. *Colloid and Interface Science Communications* **24**, 75-81, doi:https://doi.org/10.1016/j.colcom.2018.04.004 (2018).

11 Guerra, A. *et al.* Dynamic viscosity of methane and carbon dioxide hydrate systems from pure water at high-pressure driving forces. *Chemical Engineering Science* **252**, 117282, doi:https://doi.org/10.1016/j.ces.2021.117282 (2022).

12 Guerra, A., Mathews, S., Marić, M., Servio, P. & Rey, A. D. All-Atom Molecular Dynamics of Pure Water&ndash;Methane Gas Hydrate Systems under Pre-Nucleation Conditions: A Direct Comparison between Experiments and Simulations of Transport Properties for the Tip4p/Ice Water Model. *Molecules* **27**, 5019 (2022).

13 Guerra, A. *et al.* Molecular dynamics predictions of transport properties for carbon dioxide hydrates under pre-nucleation conditions using TIP4P/Ice water and EPM2, TraPPE, and Zhang carbon dioxide potentials. *arXiv preprint arXiv:2301.01757* (2023).

14 Wu, J. *et al.* Mechanical instability of monocrystalline and polycrystalline methane hydrates. *Nature Communications* **6**, 8743, doi:10.1038/ncomms9743 (2015).

15 Zhu, X., Rey, A. D. & Servio, P. Piezo-Elasticity and Stability Limits of Monocrystal Methane Gas Hydrates: Atomistic-Continuum Characterization. *The Canadian Journal of Chemical Engineering* **n/a**, doi:https://doi.org/10.1002/cjce.24433 (2022).

16 Zhu, X., Rey, A. D. & Servio, P. Multiscale Piezoelasticity of Methane Gas Hydrates: From Bonds to Cages to Lattices. *Energy & Fuels*, doi:10.1021/acs.energyfuels.2c01024 (2022).

17 Deserno, M. Notes on differential geometry with special emphasis on surfaces in R3. *Los Angeles, USA* (2004).

18 Guerra, A., Mathews, S., Marić, M., Rey, A. D. & Servio, P. An Integrated Experimental and Computational Platform to Explore Gas Hydrate Promotion, Inhibition, Rheology, and Mechanical Properties at McGill University: A Review. *Energies* **15**, 5532 (2022).

19 \it VESTA3 for three-dimensional visualization of crystal, volumetric and morphology data. *Journal of Applied Crystallography* **44**, 1272--1276, doi:10.1107/S0021889811038970 (2011).

20 Cruz, F. J. A. L., Alavi, S. & Mota, J. P. B. Low-Temperature Thermodynamic Study of the Metastable Empty Clathrate Hydrates Using Molecular Simulations. *ACS Earth and Space Chemistry* **3**, 789-799, doi:10.1021/acsearthspacechem.9b00009 (2019).

21 Falenty, A., Hansen, T. C. & Kuhs, W. F. Formation and properties of ice XVI obtained by emptying a type sII clathrate hydrate. *Nature* **516**, 231-233, doi:10.1038/nature14014 (2014).

22 Kosyakov, V. I. Structure formation under negative pressures. *Journal of Structural Chemistry* **50**, 60-65, doi:10.1007/s10947-009-0190-0 (2009).

23 Conde, M. M., Vega, C., Tribello, G. A. & Slater, B. The phase diagram of water at negative pressures: Virtual ices. *The Journal of Chemical Physics* **131**, 034510, doi:10.1063/1.3182727 (2009).

24 Jendi, Z. M., Rey, A. D. & Servio, P. Ab initio DFT study of structural and mechanical properties of methane and carbon dioxide hydrates. *Molecular Simulation* **41**, 572-579, doi:10.1080/08927022.2014.899698 (2015).

25 Takeuchi, F. *et al.* Water proton configurations in structures I, II, and H clathrate hydrate unit cells. *The Journal of Chemical Physics* **138**, 124504, doi:10.1063/1.4795499 (2013).

26 Bernal, J. D. & Fowler, R. H. A Theory of Water and Ionic Solution, with Particular Reference to Hydrogen and Hydroxyl Ions. *The Journal of Chemical Physics* **1**, 515-548, doi:10.1063/1.1749327 (1933).

27 Jendi, Z. M., Rey, A. D. & Servio, P. Ab initioDFT study of structural and mechanical properties of methane and carbon dioxide hydrates. *Molecular Simulation* **41**, 572-579, doi:10.1080/08927022.2014.899698 (2015).

28 Blöchl, P. E. Projector augmented-wave method. *Physical review B* **50**, 17953 (1994).

29 Kresse, G. & Joubert, D. From ultrasoft pseudopotentials to the projector augmented-wave method. *Physical review b* **59**, 1758 (1999).

30 Georg Kresse, M. M., ,J¨urgen Furthm¨uller. (2018).

# 6.11 Supplementary Information (SI)

## 6.11.1 Binary and Ternary Models (SI1)

Binary (two-component mixture) and Ternary (three-component mixture) were proposed in our previous and current work. This section aims to compare binary mixture model at full occupancy with a corresponding ternary mixture mode with no composition constraint.

Nomenclature:

**Binary Model:** Two-component mixture model at full occupancy. This model is only valid at full occupancy because partial occupancy implies free volume and in a real material the hydrogen network spans the system

Physical Property: $P^2$

$$S\colon small\ cage$$

$$L\colon large\ cage$$

$$N_{S/L}\colon number\ of\ small\ or\ large\ occupied\ cages\ in\ one\ unit\ lattice$$

$$V\colon total\ volume\ of\ one\ unit\ lattice$$

$$v_{S/L}\colon volume\ of\ a\ single\ small\ or\ large\ cage$$

$$V_{S/L}\colon volume\ of\ \ small\ or\ large\ occupied\ cages\ in\ one\ unit\ lattice$$

$$f\colon a\ required\ condition\ of\ at\ full\ occupancy$$

$$\varphi_{S/L}\colon volume\ fraction\ of\ occupied\ small\ or\ large\ cage\ in\ one\ unit\ lattice$$

$$P^{2S/2L}: the\ property\ of\ a\ single\ occupied\ small\ or\ large\ cage$$

$$\varphi_{Sf} = \frac{total\ volume\ of\ all\ small\ cages}{total\ lattice\ volume} = \frac{N_{sf}v_s}{V} = \frac{V_{sf}}{V} = \alpha$$

$$\varphi_{Lf} = \frac{total\ volume\ of\ all\ large\ cages}{total\ lattice\ volume} = \frac{N_{Lf}v_L}{V} = \frac{V_{Lf}}{V} = \beta$$

Constraint: $\varphi_{Sf} + \varphi_{Lf} = \alpha + \beta = 1$

Property:

$$P^2 = \varphi_{Sf}P^{2S} + \varphi_{Lf}P^{2L} = \alpha P^{2S} + \beta P^{2L} \tag{6.S1}$$

**Ternary Model:** Three-component mixture model with bounded occupancy constraint

Physical Property : P$^3$

$$HN: hydrogen - bonded\ network$$

$$S: small\ cage$$

$$L: large\ cage$$

$$o_S: occupany\ of\ small\ cages$$

$$o_L: occupancy\ of\ large\ cages$$

$$Bounds: 0 \le o_S \le 1;\ 0 \le o_L \le 1$$

$$Bounded\ constraint: 0 \le o_S + o_L \le 2$$

$$P^{3S/3L}: property\ of\ occupied\ small\ or\ large\ cages$$

$$P^{3HN}: property\ of\ hydrogen - bonded\ network$$

$$P^{3I}: property\ of\ interaction\ between\ occupied\ small\ and\ large\ cages$$

$$o_S = \frac{number\ of\ occupied\ small\ cages\ in\ one\ unit\ lattice}{total\ number\ of\ small\ cages\ in\ one\ unit\ lattice} = \frac{N_s}{N_{sf}}$$

$$o_L = \frac{number\ of\ occupied\ large\ cages\ in\ one\ unit\ lattice}{total\ number\ of\ large\ cages\ in\ one\ unit\ lattice} = \frac{N_L}{N_{Lf}}$$

$$\varphi_S = \frac{N_s v_s}{V} \tag{6.S2}$$

$$\varphi_L = \frac{N_L v_L}{V} \tag{6.S3}$$

$$\frac{o_s}{V} = \frac{N_s}{N_{sf}V} \times \frac{v_s}{v_s} = \frac{\varphi_S}{N_{sf}v_s} \tag{6.S4}$$

$$\frac{o_L}{V} = \frac{N_L}{N_{Lf}V} \times \frac{v_L}{v_L} = \frac{\varphi_L}{N_{Lf}v_L} \tag{6.S5}$$

$$o_s = \frac{V}{N_{sf}v_s} \times \varphi_S = \frac{\varphi_S}{\varphi_{Sf}} \tag{6.S6}$$

$$o_L = \frac{V}{N_{Lf} v_L} \times \varphi_L = \frac{\varphi_L}{\varphi_{Lf}} \tag{6.S7}$$

**Model P$^3$ at arbitrary occupancy in terms of volume fractions:**

**NOTE: $\boldsymbol{\varphi_L + \varphi_S \neq 1}$**

Property:

$$P^3 = P^{3HN} + o_S P^{3S} + o_L P^{3L} + o_S o_L P^{3I} \tag{6.S8}$$

Based on (6.S6) and (6.S7), (6.S8) can be shown as (6.S9)

$$P^3 = P^{3HN} + \frac{\varphi_S}{\varphi_{Sf}} P^{3S} + \frac{\varphi_L}{\varphi_{Lf}} P^{3L} + \frac{\varphi_S}{\varphi_{Sf}} \frac{\varphi_L}{\varphi_{Lf}} P^{3I} \tag{6.S9}$$

**Mapping ternary to binary at full occupancy**

**At full occupancy**

$$\begin{cases} \varphi_L = \varphi_{Lf} \\ \varphi_S = \varphi_{Sf} \end{cases}$$

$$\varphi_L + \varphi_S = \varphi_{Lf} + \varphi_{Sf} = 1$$

$$o_s = \frac{\varphi_S}{\varphi_{Sf}} = 1$$

$$o_L = \frac{\varphi_L}{\varphi_{Lf}} = 1$$

$$o_s + o_L = \frac{\varphi_S}{\varphi_{Sf}} + \frac{\varphi_L}{\varphi_{Lf}} = 2$$

$$P^3 = P^{3HN} + \frac{\varphi_{Sf}}{\varphi_{Sf}} P^{3S} + \frac{\varphi_{Lf}}{\varphi_{Lf}} P^{3L} + \frac{\varphi_{Sf}}{\varphi_{Sf}} \frac{\varphi_{Lf}}{\varphi_{Lf}} P^{3I} \tag{6.S10}$$

$$P^3 = (\varphi_{Sf} + \varphi_{Lf}) P^{3HN} + \frac{\varphi_{Sf}}{\varphi_{Sf}} P^{3S} + \frac{\varphi_{Lf}}{\varphi_{Lf}} P^{3L} + \frac{\varphi_{Sf}}{\varphi_{Sf}} \frac{\varphi_{Lf}}{\varphi_{Lf}} P^{3I} \tag{6.S11}$$

$$P^3 = \ \varphi_{Sf} \left( P^{3HN} + \frac{1}{\varphi_{Sf}} P^{3S} \right) + \varphi_{Lf} \left( P^{3HN} + \frac{1}{\varphi_{Lf}} P^{3L} \right) + P^{3I} \tag{6.S12}$$

Property:

$$P^2 = \varphi_{Sf} P^{2S} + \varphi_{Lf} P^{2L} \tag{6.S1}$$

At full occupancy: $P^2 = P^3$

$$P^{2S} = P^{3HN} + \frac{1}{\varphi_{Sf}} P^{3S} \tag{6.S13}$$

$$P^{2L} = P^{3HN} + \frac{1}{\varphi_{Lf}} P^{3L} \tag{6.S14}$$

$$P^{3I} \approx 0 \tag{6.S15}$$

Binary mixture model origins from the rule of mixture, which can be applied to all composite material. Once the property values are evaluated from the constituent material aspect, the property values of composite material can be calculated. In other words, the coefficients ($P^{2S}$ and $P^{2L}$) in the binary mixture model are evaluated from the cage aspect.

However, the ternary mixture model is designed for the gas hydrates system. It considers the structural feature of gas hydrate. The hydrogen-bonded network permanently exists regardless of the presence of guest molecules. The small and large cages are embedded in the hydrogen-bonded network. This is different from the constituent material in the binary mixture model, which does not have a basic structural skeleton. $P^{3S}$ and $P^{3L}$ are the effects estimated from the lattice aspect, originating from the occupied small or large cages.

At full occupancy, which is a special condition, the binary and ternary mixture models should generate the same results. Then the Eqns (6.S13-6.S15) shows the relationship between the properties from the binary model and the ternary model properties.

To summarize, there is no conflict between the binary and ternary mixture models. The ternary mixture model is the updated version of the binary model, which considers the structural feature of gas hydrate. At full occupancy, ensuring two models will give the same results, Eqns (6.S13-6.S15) need to be satisfied. Under other conditions, only ternary mixture models can be applied.

## 6.11.2 Steepest ascent and steepest descent curve derivation (SI2)

This section will provide detailed information for the derivations of Eqn (6.3-6.5) in the Results and Discussion section of the manuscript

The relationship between the compressive stability limits and the small and larges' occupancy can be expressed in analytical and numerical ways, as shown in Eqn (6.S16-6.S17) which are the same as Eqn (6.1-6.2) in the manuscript. The four coefficients a, b, c and d are equal to 4.6, 0.3, 1.7 and 0.7, respectively.

$$\mathrm{S}\ (\mathrm{X}, \mathrm{Y}) = \mathrm{a} + \mathrm{bX} + \mathrm{cY} + \mathrm{dXY} \tag{6.S16}$$

$$\mathrm{S}\ (\mathrm{GPa}) = 4.6 + 0.3 \times \mathrm{Q_s} + 1.7 \times \mathrm{Q_l} + 0.7 \times \mathrm{Q_s}\ \mathrm{Q_l} \tag{6.S17}$$

**Steepest Descent/Ascent Curves**

**Step 1: take partial derivatives of $\mathbf{S(X, Y)}$:**

$$\frac{\partial \mathrm{S}}{\partial \mathrm{X}} = \mathrm{b} + \mathrm{dY} \tag{6.S18}$$

$$\frac{\partial \mathrm{S}}{\partial \mathrm{Y}} = \mathrm{c} + \mathrm{dX} \tag{6.S19}$$

**Step 2: Apply standard calculus:**

$$\frac{dY}{dX} = \frac{\frac{\partial S}{\partial Y}}{\frac{\partial S}{\partial X}} \tag{6.S20}$$

$$\frac{\partial S}{\partial X}\ dY = \frac{\partial S}{\partial Y}\ dX \tag{6.S21}$$

$$(b + dY)dY = (c + dX)dX \tag{6.S22}$$

**Step 3: Integrate both sides:**

$$bY + \frac{d}{2}Y^2 = cX + \frac{d}{2}X^2 + K \tag{6.S23}$$

Where K is a constant, has a unit of GPa, the same as $S$:

$$bY + \frac{d}{2}Y^2 - \left(cX + \frac{d}{2}X^2\right) = K \tag{6.S24}$$

Plug in the coefficient values

$$0.7Y + \frac{1.7}{2}Y^2 - \left(0.3X + \frac{1.7}{2}X^2\right) = K \tag{6.S25}$$

The Eqn (6.S25) shown above is the Eqn (6.3) in the manuscript, where $X$ is $Q_s$ and $Y$ is $Q_l$.

$$bY + \frac{d}{2}Y^2 - \underbrace{\left(cX + \frac{d}{2}X^2\right)}_{R} = K \tag{6.S26}$$

Use $R$ to replace $\left(cX + \frac{d}{2}X^2\right)$

$$bY + \frac{d}{2}Y^2 - (R + K) = 0 \tag{6.S27}$$

$$Y = \frac{-b \pm \sqrt{b^2 + 4 \times \frac{d}{2} \times (R + K)}}{d} \tag{6.S28}$$

**Considering the value of Y would be positive**

$$Y(X, K) = \frac{-b + \sqrt{b^2 + 2d\left(cX + \frac{d}{2}X^2 + K\right)}}{d} \tag{6.S29}$$

**Steepest ascent curve (starting from $X = Y = 0$)**

**Step 1: to calculate the $K$ value for the steepest curve through $x = y = 0$, plug $x = y = 0$ into the equation**

$$0=\frac{-b+\sqrt{b^2+2d\left(c0+\frac{d}{2}0^2+K\right)}}{d} \tag{6.S30}$$

$$\mathbf{0}=\frac{-b+\sqrt{b^2+2dK}}{d}$$

$$-b+\sqrt{b^2+2dK}=0$$

By solving Eqn (6.S30), we can obtain the value of K.

$$\boldsymbol{K}=\mathbf{0}$$

**Thus $\boldsymbol{K}=\mathbf{0}$ for the steepest ascent curve.**

$$bY+\frac{d}{2}Y^2-\left(cX+\frac{d}{2}X^2\right)=0 \tag{6.S31}$$

**Step 2: find the ending point of the steepest ascent curve where $\boldsymbol{Y}=\mathbf{1}$.**

$$b\times 1+\frac{d}{2}\times 1^2-\left(cX+\frac{d}{2}X^2\right)=0 \tag{6.S32}$$

$$\frac{d}{2}X^2+cX-\left(b+\frac{d}{2}\right)=0 \tag{6.S33}$$

$$X=\frac{-c\pm\sqrt{c^2+4\frac{d}{2}\left(b+\frac{d}{2}\right)}}{d} \tag{6.S34}$$

Considering $X$ would be a positive value,

$$X = \frac{-c + \sqrt{c^2 + 4\frac{d}{2}\left(b + \frac{d}{2}\right)}}{d} \tag{6.S35}$$

$$\boldsymbol{X} = \frac{-c + \sqrt{c^2 + d^2 + 2db}}{d} \tag{6.S36}$$

Step 3: Evaluate the Stability limit value of the ending point of the steepest ascent curve.

$$S_{max}(X = 1, Y = 1) = a + b + c + d \tag{6.S37}$$

$$S_{min}(X = 0, Y = 0) = a \tag{6.S38}$$

$$S\left(X = \frac{-c + \sqrt{c^2 + d^2 + 2db}}{d}, Y = 1\right) = a + b\frac{-c + \sqrt{c^2 + d^2 + 2db}}{d} + c + d\frac{-c + \sqrt{c^2 + d^2 + 2db}}{d} \tag{6.S39}$$

$$S\left(X = \frac{-c + \sqrt{c^2 + d^2 + 2db}}{d}, Y = 1\right) = a + c + \frac{-c + \sqrt{c^2 + d^2 + 2db}}{d}(b + d) \tag{6.S40}$$

$$S\left(X = \frac{-c + \sqrt{c^2 + d^2 + 2db}}{d}, Y = 1\right) = S_{max} - \left(1 - \frac{-c + \sqrt{c^2 + d^2 + 2db}}{d}\right)(b + d) \tag{6.S41}$$

**Which is the same as Eqn (6.4) in the manuscript**

**Steepest decent curve (starting from $\boldsymbol{X = Y = 1}$)**

**Step 1: to calculate the $\boldsymbol{K}$ value for the steepest curve through $\boldsymbol{x = y = 1}$, plug $\boldsymbol{x = y = 1}$ into the equation**

$$1 = \frac{-b + \sqrt{b^2 + 2d\left(c + \frac{d}{2} + K\right)}}{d} \tag{6.S42}$$

$$\boldsymbol{b + d} = \sqrt{b^2 + 2dc + d^2 + 2dK}$$

$$\boldsymbol{K = b - c}$$

**Thus $\boldsymbol{K = b - c}$ for the steepest decent curve.**

$$bY + \frac{d}{2}Y^2 - \left(cX + \frac{d}{2}X^2\right) = b - c \tag{6.S43}$$

**Step 2: find the ending point of the steepest decent curve where $\boldsymbol{Y = 0}$.**

$$b \times 0 + \frac{d}{2} \times 0^2 - \left(cX + \frac{d}{2}X^2\right) = b - c \tag{6.S44}$$

$$\frac{d}{2}X^2 + cX + (b - c) = 0 \tag{6.S45}$$

$$X = \frac{-c \pm \sqrt{c^2 - 4\frac{d}{2}(b - c)}}{d} \tag{6.S46}$$

**Considering $\boldsymbol{X}$ is a positive value**

$$X = \frac{-c + \sqrt{c^2 - 2d(b-c)}}{d} \tag{6.S47}$$

**Step 3: Evaluate the Stability limit value of the ending point of the steepest decent curve.**

$$S\left(X = \frac{-c + \sqrt{c^2 - 4\frac{d}{2}(b-c)}}{d}, Y = 0\right) = a + b\frac{-c + \sqrt{c^2 - 2d(b-c)}}{d} \tag{6.S48}$$

$$S\left(X = \frac{-c + \sqrt{c^2 - 4\frac{d}{2}(b-c)}}{d}, Y = 0\right) = S_{min} + b\frac{-c + \sqrt{c^2 - 2d(b-c)}}{d} \tag{6.S49}$$

Which is the same as Eqn (6.5) in the manuscript

# Chapter 7

# 7 Discussion and Recommendations for Future work

## 7.1 Comprehensive Discussion

In section 7.1, we synthesize all of the results we have obtained thus far and demonstrate how each chapter fits my thesis plan, scope, and objectives and contributes to knowledge.

The primary objective of this thesis is to investigate the effects of pressure on the stability performance of gas hydrates and to determine their stability limits. To accomplish this objective, we approach this problem from two angles: numerical simulation and geometric-structural analysis. The contribution of each chapter and the relationship between them will be discussed as follows.

Using atomistic-continuum simulations, Chapter 3 investigates the mechanical properties and stability of methane gas hydrates. The results show that the tensile and compressive pressure stability limits are -1.1 GPa and 7.5 GPa, respectively, and that the values of second-order elastic constants would exhibit abnormal changes as these limits are approached. In particular, the changing tendency of the fundamental mechanical parameters, second-order elastic constants (SOEC), under pressure was studied, as well as their effects on the mechanical properties of monocrystalline and polycrystalline gas hydrates. The determination of its intrinsic brittle and ductile properties under pressure is critical in determining which type of fracture mechanism would be triggered. The computational time and cost would be a major concern, even though Chapter 3 presents solid results that demonstrate the properties of gas hydrates. In this project, simulations were conducted at over 20 pressure points. For the calculation of SOECs, at each pressure point, more than twenty simulations, each requiring approximately 30 GB of memory and 24 hours of simulation time, must be performed. This significant computational time and memory cost suggests the possibility of higher-order elastic constants for evaluating the piezo effect, which is the impetus for Chapter 5. Chapter 3 sheds light on the fundamental mechanical properties and stability limits of methane gas hydrates and provides a numerical simulations-based foundation for understanding their behaviour under external loads and in different environmental conditions. To complete the picture, we proposed studying the structural changes resulting from pressure effects, as described in Chapter 4.

Motivated by the numerical results from Chapter 3, Chapter 4 investigates the structure, thermodynamics, and elasticity of sI methane hydrates subjected to pressure loads, at three scales: atoms, cages, and lattice, using the density functional theory in conjunction with homogenization methods and the theory of mixtures. The distribution functions of bond parameters (e.g. bond angles and bond lengths) verify that the parameters values should not be constants under a specified condition. The role of different types of cages at the mesoscale have been identified, such as continuous phase and disperse inclusion, which helps to discover the cage's effect on the entire lattice in terms of mechanical properties and stability, as shown in Chapter 6. Meanwhile, at the continuum scale, the different deformation mechanisms are observed (affine and non-affine), which correspond to different fracture mechanisms (brittle and ductile) under tensile and compressive pressures, respectively. These findings are consistent with the ductile-to-brittle transition results found in Chapter 3. Taken together, the systematic atomic–cage–lattice multiscale characterization proves to be fruitful in linking processes that connect mechanical properties, cage geometry, and hydrogen bonding.

As a continuation of Chapter 3, Chapter 5 investigates piezo effects via numerical simulation with higher-order elastic constants. In Chapter 5, third-order elastic constants (TOECs) become the primary focus of research, particularly to determine whether the non-linear pressure/strain effect can be predicted using TOECs. The results demonstrate that the use of TOECs can not only provide a reliable prediction of the SOECs value under pressure, but also save a substantial amount of computation time and cost. Non-linear fitting with TOECs provides a more accurate overall prediction and a smaller root-mean-square deviation on pressure-strain evaluation than linear fitting. In addition, the non-linear fit offers a more precise and accurate prediction of the transition from ductile to brittle. Using the equations stated in Chapter 5, the results of Chapter 5 demonstrate that TOECs are able to evaluate the piezo effects on SOECs as well as some mechanical properties. In terms of numerical simulations, these results would significantly contribute to the study of piezo-effects on hydrogen-bonded crystalline materials. Future research can save a great deal of computational time and memory through its use.

Chapter 6, which is an extension of Chapter 4, investigates piezo effects from a geometric-structural standpoint. In this chapter, the focus was on hydrate occupancy and the function of cages in maintaining stability under pressure. Through face connectivity, the inclusion-matrix material structure of sI gas hydrates was first determined. The effects of the type of occupied cages were then determined and quantified. A proposed equation illustrates the impact of occupied cages and their interaction with the lattice stability. In the meantime, two types of fracture mechanisms associated with occupied cage types have been identified. If the large cages, which represent the matrix phase, are occupied, the multi-step fracture mechanism would be activated. If, on the other hand, only the small cages, which play the role of disperse inclusion, are occupied, the one-step fracture mechanism would occur. Meanwhile, to change the stability of the hydrate, the steepest ascending/descending pathways are identified. In conclusion, this chapter examined the stability of gas hydrates under pressure from a geometric-structural perspective. It recognizes the inherent matrix-inclusion structure of sI gas hydrate, implying that other types of gas hydrates may have phased structures as well.

To summarize, the goal of this thesis is to investigate the pressure effect on sI methane hydrates and determine their pressure stability limits. To accomplish this objective, two methods were utilized; direct simulation and atomistic-geometric analysis. Chapters 3 and 4 both developed a general understanding of the hydrate's stability under pressure based on the aforementioned aspects. The consistency between Chapter 3 and Chapter 4 results further validates the accuracy and reliability of the results. Chapters 5 and 6 are the continuations of Chapters 3 and 4, respectively. They investigated the stability of gas hydrates using higher-order elastic constants and matrix-inclusion structure. They provide new methods and insight to make the results more accessible to the research community at a lower computational cost.

## 7.2 Recommendations for Future Work

In this section, the future research strategy and potential applications based on the discussion presented in section 7.1, will be covered.

Section 7.1 discussed the pressure effects on the hydrates at zero Kelvin. In other words, the temperature effects have a great potential to be explored as well as the interaction between temperature and pressure. Also, the role of cages has been determined through the face connectivity. The following are some specific recommendations for future work .

1. Further studies of pressure limits and their effects on sI methane gas hydrate from molecular dynamic aspect are needed, as only atomistic simulations were performed in this work.
2. Characterization of temperature effects and temperature limits of sI methane gas hydrates, as well as the interaction between pressure and temperature.
3. Further characterize the distribution functions of bond parameters shown in Chapter 4 and explain changes of distribution under pressure through the oxygen atoms' classification (e.g. forbidden zones)
4. Investigating the location of crack nucleation and the path of crack propagation of sI methane gas hydrates once the system reaches the pressure stability limits based on the one-step and multi-step fracture mechanisms proposed in Chapter 6
5. Studying the effects of other guest molecules (e.g. carbon dioxide) on the sI gas hydrate's stability in terms of the pressure and temperature.
6. Investigating the pathway for the structural transition from sI to sII once the cracks are initiated in terms of the environmental conditions, type of guest molecules and etc.

7. Using the results of Recommendation 3 and Chapters 4 and 6, develop a systematic method for identifying the structure and integrity of polygons and cages.

# Chapter 8

# 8 Conclusions

This thesis examined the effects of pressure on sI methane hydrates at zero Kelvin on a wide range of mechanical properties and on the mechanical and geometric stability limits under pressure. The research included both direct numerical simulations and atomistic-geometric analysis. To achieve this goal, the thesis was divided into two interconnected branches. Chapters 3 and 5 incorporated numerical simulations. In Chapters 4 and 6, the geometric structural analysis was formulated, implemented and validated.

As a first step, the Ab initio first principle was implemented in Chapter 3 by employing the density functional theory and the VASP software to simulate sI methane hydrates and establish a comprehensive understanding of the pressure effects and stability limits. The results showed that the tensile and compressive stability limits are -1.1 GPa and 7.5 GPa respectively, which has been verified by Born's stability criteria. The second-order elastic constants (SOECs) change subject to pressure changes, and these changes would contribute to the mechanical properties as well. The ductile-to-brittle transition was found at the zero pressure. To be specific, the hydrates show ductile behaviors under compressive pressure and vice versa.

To further develop the understanding of hydrate's stability under pressure and validate the results , Chapter 4 utilized the multi-scale geometric structural analysis ranging from atoms to lattice to visualize the structural deformation under pressure. Firstly, the electronic cloud movements have been recorded at the pressure stability limits determined in Chapter 3. Also, the distribution functions of bond parameters (e.g. bond angles and bond lengths) subjected to pressure are investigated. The discrepancies between the deformation of large and small cages under pressure suggest that the roles of occupied cages would have a significant impact on how the piezo effect reflects on the lattice. Thus, the rule of mixtures was used to determine if the sI gas hydrate adheres to the rules of composite materials. The results demonstrate that the bulk modulus values derived from direct simulation and the rule of mixture are highly consistent, providing substantial confidence for the subsequent cage role study presented in Chapter 6.

The third step was based on the consideration of  simulation cost in Chapter 3 and 4. The results from either numerical simulation or multi-scale geometric-structural analysis require much computational cost. Thus, in Chapter 5, the third-order elastic constants (TOECs) were studied to investigate if the non-linear fitting involving TOECs could provide a reliable prediction on the SOECs under pressure as well as the mechanical properties. The comparisons, has been conducted among direct numerical simulations, linear fitting and non-linear fitting, and the analysis showed that the non-linear fitting involving the TOECs is able to predict the values of SOECs under pressures and could provide similar results as shown in Chapter 3. These findings could save significant amount of computation time and cost for the research community and promote the higher-order elastic constants studies.

In Chapter 6, a continuation of Chapter 4, it is determined how cage and occupancy affect the stability of sI methane hydrates. The application of the rule of mixture in Chapter 4 demonstrates that sI gas hydrates behave as composites, leading us to determine the two-phase structure in Chapter 6. In order to further investigate the cage effects on the hydrates' stability, an equation demonstrating the relationship between the occupancy and the compressive stability limit has been proposed. Additionally, the steepest ascent/descent path for hydrate stability has been determined, which will help stabilise the hydrate during pressure changes. In addition, two types of fracture mechanisms will be triggered based on the type of cage that is occupied. These results further validate the composite material property discovered in Chapter 4 and provide a novel understanding of the structure of hydrates.

In conclusion, this thesis demonstrated the pressure stability limits of sI methane hydrates and the associated piezo-effects on the hydrate's stability. The limits of compressive and tensile stability are 7.5 GPa and –1.1 GPa, respectively. Pressures affect both the second-order elastic constants (SOECs) and the mechanical properties. When approaching the limits of stability, both exhibit abnormal behaviours or changes. The non-linear fitting involving third-order elastic constants (TOECs) provides an accurate prediction of the SOECs values under pressure, which can save a substantial amount of computational time and resources. In addition, the geometric-structural analysis confirms the accuracy of the Chapter 3 and Chapter 5 results. The pressure-induced deformation has been studied in terms of atoms, cages, and lattices. The bond parameter distribution functions reveal the local characteristics of the lattice. Moreover, the application of the rule of mixture indicates that hydrates may share similarities with composite materials. Thus, in Chapter 6, the geometry of sI hydrates was investigated further. The structure of two phases has been determined. Meanwhile, the relationship between hydrate stability and cage occupancy is quantified. Additionally, the two relevant fracture mechanisms have been identified. All of these findings establish a thorough comprehension of sI gas hydrates under pressure. This thesis provides not only a quantitative deep understanding of how the gas hydrate would react under pressure, but also an advanced and reliable method for examining in the future the stability of other hydrogen-bonded materials.